Université de Montréal

Development of New Radiotracers for PET Imaging of Adrenomedullin and Angiotensin II Type 1 Receptors

par Luis Michel Alonso Martinez

Département de pharmacologie et physiologie
Institut de génie biomédical – Faculté de médecine

Thèse présentée en vue de l'obtention du grade de Philosophiae doctor (Ph.D.) –
Doctorat en génie biomédical

Mai 2020

Development of New Radiotracers for PET Imaging of Adrenomedullin and Angiotensin II Type 1 Receptors

par Luis Michel Alonso Martinez

Thèse évaluée par un jury composé des personnes suivantes:

Prof. Frédéric Lesage, Président-rapporteur
Prof. Jean N. DaSilva, Directeur de recherche
Prof. François Harel, Codirecteur
Prof. André Charette, Membre du jury
Prof. Brigitte Guérin, Examinateur externe
Prof. René Cardinal, Représentant de la doyenne

Résumé

Les récepteurs de l'adrénomédulline sont fortement exprimés dans les capillaires alvéolaires humains et fournissent une cible moléculaire pour l'imagerie de la circulation et de l'embolie pulmonaire. Au cours des années précédentes, le dérivé DFH12 marqué au ^{99m}Tc (PulmoBind) a démontré son potentiel en tant qu'agent d'imagerie SPECT de l'hypertension pulmonaire dans des études cliniques de phase I et II. L'objectif principal de mon projet est de développer le nouvel analogue DFH17 pour l'imagerie TEP des récepteurs de l'adrénomédulline via la méthode de l'Al^{18}F. Pour atteindre cet objectif, un système d'élution semi-automatique a été conçu pour produire l'Al^{18}F concentré directement dans le vial de réaction. En utilisant des tests de complexation avec le chélateur NOTA, des conditions optimales ont été trouvées pour le radiomarquage du DFH17 avec l'Al^{18}F. La combinaison du rapport Al/DFH17 1:3 dans l'éthanol 50% a permis de produire le [^{18}F]AlF-DFH17 avec des puretés radiochimiques et chimiques élevées. Les études TEP avec le [^{18}F]AlF-DFH17 ont démontré un rapport élevé poumon-bruit de fond ainsi qu'une grande stabilité *in vivo* chez le rat, le chien et le primate. Des captations différenciées dans les poumons des trois espèces ont aussi été détectées par imagerie TEP et leurs différences ont été associées à des variations de la composant RAMP2. Compte tenu de l'importante captation pulmonaire, de la stabilité *in vivo* et de la dosimétrie favorable, le nouveau dérivé [^{18}F]AlF-DFH17 est un excellent candidat potentiel en tant que traceur TEP des récepteurs adrénomédulline humains.

L'expression des récepteurs AT_1 de l'angiotensine II est altérée dans plusieurs maladies cardiovasculaires et rénales, telles la défaillance cardiaque, rénale et l'hypertension ainsi que dans certains cancers. Auparavant, le dérivé [^{11}C]méthyl-Candesartan a démontré un potentiel comme agent d'imagerie TEP de l'AT_1R rénal mais une proportion élevée du signal TEP

correspondait à une liaison non-spécifique d'un radiométabolite hydrophobe. Dans ce travail, l'objectif principal est de développer le nouveau dérivé [^{18}F]fluorobenzyl-Candesartan en utilisant le 4[^{18}F]fluoroiodobenzène ([^{18}F]FIB) avec un profil métabolique et de biodistribution potentiellement meilleurs. Pour atteindre cet objectif, des paramètres réactionnels de fluorination tels que le solvant, la quantité de précurseur, le catalyseur et la température ont été optimisés permettant la radiosynthèse du [^{18}F]FIB avec des rendements et pureté élevés. Ensuite, le couplage du [^{18}F]FIB au dérivé alcyne-trityl-Candesartan a été évalué en utilisant la réaction de Sonogashira suivie d'une détritylation acide. Suite à l'étude de plusieurs conditions de couplage, le rendement de radioconversion a été légèrement augmenté en utilisant le catalyseur $Pd(PPh_3)_4$/CuI et K_2CO_3 comme base. Les meilleures conditions de fluorination et de couplage ont été automatisées pour le module de synthèse Synthra® RNPlus Research. La production du [^{18}F]FB-Candesartan été atteinte avec de faibles rendements et activités molaires en raison de la formation d'impuretés ayant des structures et temps de rétention par HPLC similaires à ceux de notre traceur. Des études supplémentaires afin d'améliorer le rendement, la purification par HPLC et l'activité molaire se sont avérées infructueuses pour l'instant. D'autres expériences devront être effectuées à cette fin. En conclusion, l'utilisation de la réaction de Sonogashira pour produire le [^{18}F]FB-Candersartan avec des rendements et des activités molaires élevées s'est avérée difficile.

Mots-clés: Al^{18}F, Complexe de NOTA, Récepteurs de l'adrénomédulline, TEP, [^{18}]FIB groupement prosthétique, Réaction de couplage croisé de Sonogashira, Réaction catalysée par Pd, Radiosynthèse automatisée, AT_1R

Abstract

Adrenomedullin receptors are highly expressed in human alveolar capillaries and provide a molecular target for imaging the integrity of pulmonary microcirculation. In previous years, the ^{99m}Tc-labeled DFH12 derivative (PulmoBind) demonstrated its potential as a SPECT imaging agent of pulmonary hypertension in phase I and II clinical trials. In this work, we aimed to develop a NOTA-derivatized adrenomedullin analog (DFH17), radiolabeled with aluminum fluoride ([^{18}F]AlF), for PET imaging of pulmonary microcirculation. To achieve this goal, highly concentrated [^{18}F](AlF)$^{2+}$ was produced from purified ^{18}F using a semi-automatic system. Using inexpensive complexation assays with NOTA, optimal conditions at each step of the process were determined facilitating the radiolabeling optimization of DFH17. Furthermore, combining the Al-to-DFH17 1:3 ratio in 50% ethanol as co-solvent, allowed [^{18}F]AlF-DFH17 production in high radiochemical and chemical purities. PET/CT and biodistribution demonstrated high [^{18}F]AlF-DFH17 lung-to-background ratio and *in vivo* stability in rats, dog and primate. Contrasted inter-species uptake in the lungs associated with variations of RAMP2 were also detected by PET imaging. Considering high lung uptake, *in vivo* stability and favorable dosimetry observed in the monkey, the novel AM derivative [^{18}F]AlF-DFH17 exhibits an excellent potential as a PET tracer of human AM receptors.

Alterations of the expression levels of AT_1R has been linked to cardiac and renal diseases, such as cardiac and renal failures, hypertension and some type of cancers. Previously, [^{11}C]methyl-Candesartan displayed potential for PET imaging of AT_1Rs, but a high proportion of PET signal corresponded to non-specific binding from a ^{11}C-labeled hydrophobic metabolite. In this work, the main objective was to develop the novel derivative [^{18}F]fluorobenzyl-Candesartan, with potentially better metabolic profile and biodistribution, using 4-[^{18}F]fluoroidobenzene

([^{18}F]FIB) as prosthetic group. To pursue this goal, radiofluorination parameters such as solvent, amount of precursor, type of catalyst and temperature were optimized to reliably synthesize [^{18}F]FIB in high yield and purity. Coupling of [^{18}F]FIB to the alkyne-trityl-Candesartan was evaluated using the Sonogashira cross-coupling reaction followed by an acid deprotection. After studying several Pd-cross-coupling conditions, the radioconversion yield was slightly increased by means of a $Pd(PPh_3)_4$/CuI catalyst and K_2CO_3 as base in DMF. Therefore, the best reaction conditions for [^{18}F]FIB fluorination and its coupling to alkyne-Candesartan followed by an acid hydrolysis, was fully automated for Synthra® RNPlus Research synthesis module. In general, the synthesis of [^{18}F]FB-Candesartan was achieved in low yields and molar activities due to the formation of structurally-close by-product(s) with similar HPLC retention time. Additional studies to further improve the yield, HPLC purification and molar activity (MA) have been unsuccessful. Other experiments will need to be performed to this end. In conclusion, the use of Sonogashira cross-coupling reaction to produce [^{18}F]FB-Candesartan in high yields and molar activities was found to be challenging.

Keywords: Al^{18}F, NOTA complex, Adrenomedullin receptors, PET, [^{18}]FIB prosthetic group Sonogashira cross-coupling reaction, Pd-catalyzed reaction, Automated radiosynthesis, AT_1R

Note

This document compiles the development of two novel compounds for PET imaging of AM and AT_1Rs . The thesis has been written based on scientific articles. Thus, I specify herein my contribution to each chapter. The Chapter 1 (Introduction), 5 and Annexes were written by myself and edited by Professor Jean N. DaSilva.

The article in Chapter 2 entitled “SPECT and PET imaging of adrenomedullin receptors: a promising strategy for studying pulmonary vascular diseases” extensively reviews all radiotracers for molecular imaging of AM receptors in pulmonary vascular diseases. Previous labeling experiment for primate PET studies were performed by Dr Michael T. Klimas group from Merck Research Laboratories. I carried out the Al^{18}F-formation studies, semi-automatic production of Al^{18}F and NOTA-complexation assays at the Laboratoire de Radiochimie et Cyclotron (CRCHUM). I performed together with Dr Harel staff the DFH17 radiolabeling experiments and QC analyses for animal studies at the Research Centre of Montreal Heart Institute. PET imaging processing and quantification was done by Dr Harel’s team with my participation. Al[^{18}F]F-DFH17 PET and dosimetry studied in non-human primate were performed by Dr Harel’s group in collaboration with Dr Michael T. Klimas. All authors reviewed and agreed this chapter for publication, which was handled by myself and Prof DaSilva.

The Chapter 3 entitled “Al[^{18}F]F-complexation of DFH17, a NOTA-conjugated adrenomedullin analog, for PET imaging of pulmonary circulation” describes the synthesis, radiolabeling and *in vivo* evaluation of the novel adrenomedullin derivative DFH17 as a potential PET imaging agent of pulmonary hypertension and pulmonary embolism. DFH17 peptide was designed by Prof. Alain Fournier and Prof. Jocelyn Dupuis and was synthesized and

characterized by Ms. Myriam Létourneau at the Laboratoire D'études Moléculaires et Pharmacologiques des Peptides (all co-authors). I performed all Al^{18}F-formation experiment and NOTA complexation assays at Laboratoire de Radiochimie et Cyclotron (CRCHUM) and DFH17 radiolabeling, reactions optimization, and QC and Dr Harel's lab at Montreal Heart Institute. Biodistribution, PET and imaging processing and quantification was done by Dr Harel's team with my participation. All authors reviewed and agreed this chapter for publication, which was handled by myself and Prof DaSilva.

The Chapter 4 entitled "Development of a novel [^{18}F]fluorobenzyl derivative of the AT_1R antagonist Candesartan" presents the radiosynthesis and automation of a new potential Candesartan derivative labeled with [^{18}F]FIB using the Sonogashira cross coupling reaction. I performed all organic synthesis and characterization as well all radiosynthesis, optimization, automation and radioanalytical evaluation at Laboratoire de Radiochimie et Cyclotron (CRCHUM). The chapter was written by myself and subsequently reviewed and edited by Professor DaSilva.

In Chapter 5, a summary and discussion of important aspects not discussed in detail in the manuscripts are presented followed by the conclusion and perspectives of this thesis. These sections were written by me and reviewed by Professors DaSilva and Harel.

Table of Contents:

List of Figures

Chapter 1

Chapter 2

Chapter 3

Chapter 4

Chapter 5

Annex for Chapter 5

List of Schemes

Chapter 1

Chapter 3

Chapter 4

List of Tables

Chapter 1

Chapter 2

Chapter 3

Chapter 4

List of abbreviations

[^{18}F]AlF F-18 Aluminum fluoride

[^{18}F]FB F-18 fluorobenzyl

[^{18}]FIB F-18 fluoroiodobenzene

%ID percent of the injected dose

ACE angiotensin converting enzyme

ACEI ACE inhibitor

AlF Aluminum fluoride

AM Adrenomedullin

Ang Angiotensin

ARBS AT1R blockers

AT_1R Angiotensin type 1 receptor

Bq Becquerel

CGRP Calcitonin gene-related peptide

Ci Curie

CLR Calcitonin receptor-like receptor

CT Computerized tomography

CTEPH Chronic thromboembolic pulmonary hypertension

DFH12 N_4-chelator derivative of adrenomedullin fragment 22-52

DFH17 NOTA-chelator derivative of adrenomedullin fragment 22-52

DMF Dimethylformamide

DMSO Dimethylsulfoxide

DOTA 1,4,7,10-Tetraazacyclododecane-1,4,7,10-tetraacetic acid

DTPA Diethylenetriaminepentaacetic acid

ECL Extracellular loop

ED Effective dose

EDTA 2,2',2",2"'-(Ethane-1,2-diyldinitrilo)tetraacetic acid

EOB end of bombardment

EOS End of synthesis

ESI-MS Electrospray ionization mass spectrometry

EtOAc Ethyl acetate

eV Electron-volt

FB Fluorobenzyl

FDA Food and drug administration

FIB Fluoroiodobenzene

FOV field of view

GPCR G protein-coupled receptor

hAM (1-52) Human adrenomedullin

hAM (22-52) Human adrenomedullin fragment 22-52

HF heart failure

HPLC high-performance liquid chromatography

HRMS high-resolution mass spectrometry

IC_{50} Half maximal inhibitory concentration

ICL Intracellular loop

K222 Kryptofix 222

MA Molar activity

MAA Albumin marco-aggregates

MALDI-TOF Matrix Assisted Laser Desorption Ionization - Time of Flight

MAP Mean arterial pressure

MRI Magnetic resonance imaging

NMR Nuclear magnetic resonance

NODA-MPAA 2,2′-(7-(4-(2-((2-aminoethyl)amino)-2-oxoethyl)benzyl)-1,4,7-triazonane-1,4-diyl)diacetic acid

NOTA 2,2′,2”-(1,4,7-triazacyclononane-1,4,7-triyl)triacetic acid

NOTA-NHS NOTA mono-N-hydroxysuccinimide

PEG Polyethylene glycol

PET positron emission tomography

PH Pulmonary hypertension

QC quality control

QMA Quaternary methyl ammonium

rAM (1-50) Rat adrenomedullin

RAS renin angiotensin system

RBF Renal blood flow

ROI Regions of interest

SAR structure-activity relationship

SCN-Bz-NOTA 2-S-(4-isothiocyanatobenzyl)-1,4,7-triazacyclononane-1,4,7-triacetic acid

SPECT Single-photon computerized tomography

TAC time-activity curve

$TBAHCO_3$ Tetrabutylammonium hydrogenocarbonate

TEA Triethylamine

TFA Trifluoroacetic acid

THF Tetrahydrofuran

TLC thin layer chromatography

TM transmembrane

t_R retention time

Acknowledgements

This thesis is dedicated to my family, supervisors, colleagues, friends, institutions and all those who made these five years worthwhile.

Chapter 1: Introduction

1.1 Cyclotron.

Cyclotron-produced radionuclides, and their corresponding radiopharmaceuticals, are extremely valuable in basic medical research, disease diagnosis and radiotherapy treatment. Practically, most used PET radioisotopes (**Table 1**) are currently produced by a medical cyclotron.

Table 1 Most typically used positron-emitting isotopes and their cyclotron production conditions.

Radionuclide	$t_{1/2}$	Decay mode	Reaction	Energy (MeV)
C-11	20.3 min	β^+	$^{14}N(p,\alpha)$	11-17
N-13	9.97 min	β^+	$^{16}O(p,\alpha)$ $^{13}C(p,n)$	19
O-15	2.03 min	β^+	$^{15}N(p,n)$ $^{14}N(d,2n)$ $^{16}O(p,pn)$	11 6 >26
F-18	110 min	β^+	$^{18}O(p,n)$ $^{nat}Ne(d,\alpha)$	11-17 8-14
Cu-64	12.7 h	β^+	$^{64}Ni(p,n)$	8-15
Ga-68	67.8 min	β^+	$^{68}Zn(p,n)$	4.5-14

The cyclotron was invented by Ernest O. Lawrence and Milton S. Livingston in 1934 to accelerate particles (i.e. protons and deuterons) until achieving a high kinetic energy [1, 2]. Then these particles can be used to bombard other nuclei at a particular energy in a target to produce short-lived positron-emitting isotopes that are then incorporated in a molecule (called radiotracer or radiopharmaceutical) for PET or SPECT imaging.

The cyclotron operating principle is based on the fact that the motion period of charged particles in a uniform magnetic field is independent of the velocity of the particle (**Figure 1**) [3, 4]. Briefly, the four systems (vacuum, ion source, acceleration force and beam control) are necessary to generate a particle beam capable of creating radionuclides. By combination of these four systems in the cyclotron, particle beam produced via the ion source is moving inside semi-circular

dees (or D-shaped metal plates) which are placed inside vacuum chambers exposed to a static electromagnetic field perpendicular to the electrode plane. The particle beam is kept under vacuum to avoid interactions with other particles and to maintain the beam focused. Then, the charged particle beam is accelerated using a high radiofrequency alternating voltage, which is applied between two hollow "D"-shaped sheet metal electrodes. The presence of a magnetic field causes the particles to curve their path in a circular shape and the electric field to correct the direction to accelerate them. After each semi-revolution, the particles move in a quasi-spiral orbit outward from the center to the rim of the dees acquiring a high kinetic energy (up to its possible maximum), due to pushes created by the reverse of radiofrequency voltages [5].

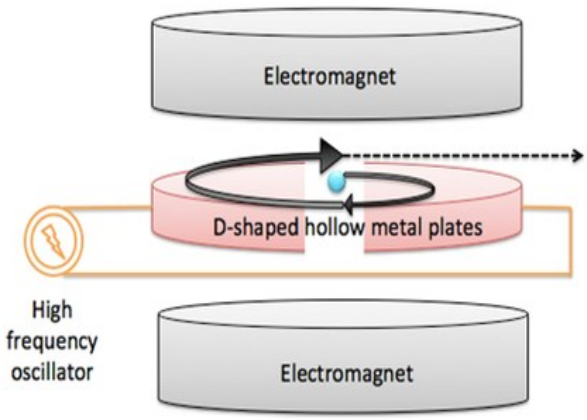

Figure 1. Basic scheme of a cyclotron.

Considering the maximum proton energy, cyclotrons are classified by type I (up to 10 MeV), type II (20 MeV) and type III (45 MeV). Nowadays, most cyclotrons accelerate negative ions due to the greater simplicity of the beam extraction process. If the particles are negatively charged, extraction is carried out by stripping electrons off the negatively charged ions and allowing the magnetic field to reverse the curvature of the resulting positively charged particle paths and to transport the particles out of the cyclotron [6]. For example, hydride ions formed by

the ion source are accelerated and then transformed into protons by charcoal thin foils to posteriorly incise in the target producing the nuclear reaction [7, 8].

1.2 Production of ^{18}F.

1.2.1. Targetry

Fluorine-18 has been produced by a variety of nuclear reactions, using both nuclear reactors and accelerators. The target materials used can be either in the solid, liquid or gas phase. Solid targets of enriched $^{6}LiCO_3$ have been used for production of ^{18}F. In this case, separation of ^{18}F from the solid target is performed by absorbing the [^{18}F]fluoride on alumina or ion exchange resins, followed by thorough washing step before [^{18}F]fluoride is eluted under basic conditions [9]. Gas targets, such as enriched ^{18}O and ^{20}Ne are also used for the production of $^{18}F^-$ via $^{18}O(p,n)^{18}F$ and $^{20}Ne(d,\alpha)^{18}F$ nuclear reactions [10]. Both target systems produce carrier-added ^{18}F gas ($^{18}F_2$) suitable for electrophilic radiofluorination reactions intended for applications where high molar activity (MA) is not required [11].

No-carrier-added [^{18}F]fluoride at high MA is currently produced using a liquid target of enriched [^{18}O]water in a chamber made of inert metal, such as silver, titanium, niobium or tantalum. [^{18}F]fluoride produced following $^{18}O(p,n)^{18}F$ reaction is the most commonly production way for PET studies [12]. Taking this into account, we will be focused on this single form of production in the following sub-chapters.

1.2.2. Production cross-section

Accelerated charged particles interact with a target nucleus producing a nuclear reaction, ultimately leading to a stable or radioactive nucleus. A nuclear reaction is characterized by a cross-section, a geometrical quantity given in barn (10-24 cm^2), representing the total probability that radionuclide can be formed and will then decompose along a particular decay. The reaction cross-section occurs in function of energy along with other factors including the thickness of the target. Considering the cross-section, the beam current determines the amount of radionuclide that can be produced in a given cyclotron at various energy levels and the levels of contamination with other radionuclides that may be present in the target material. [7, 13]. As consequence, the nuclear reaction cross-section data are needed in radioisotope production programs mainly for optimization of radionuclide production routes.

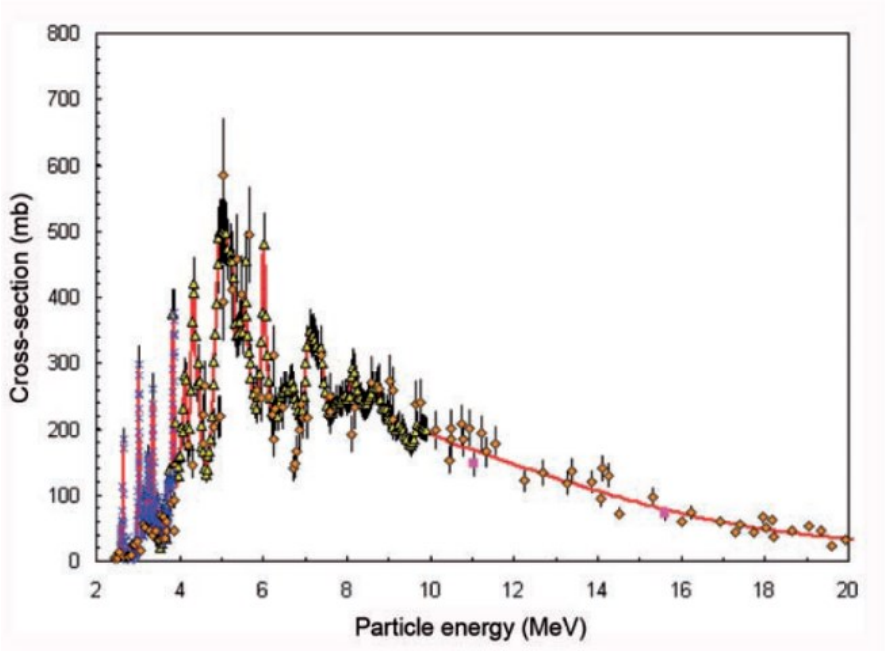

Figure 2. Excitation function for the $^{18}O(p,n)^{18}F$ reaction

In recent years, the $^{18}O(p,n)^{18}F$ reaction on highly enriched ^{18}O-targets (particularly as $H_2{}^{18}O$) has been extensively used. This nuclear reaction has relatively low threshold energies (0-20 MeV), and its maximum yield occurs at less than 10 MeV (**Figure 2**) [14]. Taking into account that the $^{18}O(p,n)^{18}F$ reaction is endoergic (Q value of -2.43 MeV), the minimum kinetic energy that the bombarding proton should possess for this reaction to be energetically possible is of 2.57 MeV. Thus, selecting proton energies higher 3 MeV maximizes the probability of occurrence of this reaction [15]. However, energy values above 10 MeV are usually selected since F-18 production yield will be much higher (as will be explained in next section).

1.2.3. ^{18}F production beam

Proton beam energy and the beam current along with the target volume are important practical factors in the production of ^{18}F that determine how much [^{18}F]fluoride can be produced in a given amount of time [16]. As depicted in **Figure 3**, there is a relative dependence between [^{18}F]fluoride yield and proton beam energy for a theoretical thick target [17]. As can be seen, the production yield of [^{18}F]fluoride (from the $^{18}O(p,n)^{18}F$ nuclear reaction) rises nearly linearly from 5 to 15 MeV and gradually, and at a lower rate above 15 MeV. This theoretically indicates that cyclotrons with proton energies higher than 15 MeV will produce at least 50% more F-18 compared to a 10-11 MeV cyclotron for the same beam current. However, taking into account the (p,n) reaction cross-section (**Figure 2**), energies above 18 MeV are not really necessary for the routine production of [^{18}F]fluoride since the nuclear reaction will occur at lower probabilities.

Moreover, the beam current of a cyclotron also has an influence in how much radioisotope can be produced at a given energy. Theoretically speaking, the production yield is directly proportional to the beam current but in practice, the beam current is also determined by the ability to remove the heat produced in a target by a beam. Most medical cyclotrons are capable of

generating a beam with a current of at least 50 μA. Typically, a target with a given operating pressure has an optimum current at which the production rate of the desired amount of radionuclide is the highest [17].

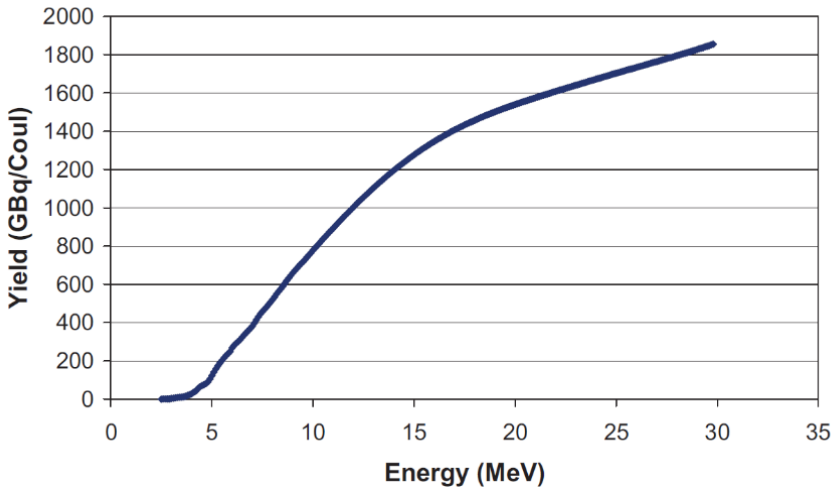

Figure 3. Relationship between ^{18}F irradiation yield and beam energy [17].

1.2.4 ^{18}F transfer and recovery

[^{18}F]fluoride from the ^{18}O enriched water target is typically transferred to the synthesis unit, where the ^{18}F is extracted from the irradiated aqueous solution and the ^{18}O-enriched water is recovered. Transport of the water containing the ^{18}F is usually carried out using small bore plastic tubing. The most common materials for this tubing are polyethylethylketone, tefzel or polyethylene. These materials are designed to contain very low amounts of ^{19}F reducing the formation of the unlabeled final radiopharmaceutical containing natural fluoride and therefore, without being detrimental to the MA of the final radiofluorinated compound [18]. There is a clear need of a reliable production of high MA radiopharmaceuticals that is particularly important for saturable receptor/transporter ligands. As PET is a true tracer technique (imaging at nM concentrations), receptor occupancy of radiolabeled tracers should be kept below about 1%, in

order to visualize easily-saturable receptors and also to avoid possible pharmacological/toxic effects [19].

With the purpose of reducing the excess of water in radiofluorination nucleophilic reactions [^{18}F]fluoride is usually recovered from enriched water using several different techniques. Among them, ion exchange resin or quaternary methyl ammonium (QMA) anion exchange resin offers not only separation of [^{18}F]fluoride and efficient recovery of expensive enriched [^{18}O]water [20], but also scavenging of many ion contaminants from the target or foil that can alter radiofluorination reactions [21]. Due to the presence of oxygen-16 in the target water (usually at 2% levels, with ^{18}O enriched water at 98%), nitrogen-13 ($t_{1/2}$ = 10 min) is also formed within the target by the (n,α) nuclear reaction. Nitrogen-13 constitutes a radionuclide impurity and can appear as nitrate, nitrite, nitrogen and/or ammonia [22]. Hence major part of ^{13}N will decay during the synthesis time. Importantly, ^{13}N-labeled cation impurities are commonly eliminated in the QMA elution in where nitrogen-13 cations are eluted while $^{18}F^-$ is trapped in the resin.

1.3 Decay of ^{18}F.

Nuclei that are “neutron deficient” or “proton rich” can decay by positron emission accompanied by the emission of a neutrino. After emission of a positron-particle, the daughter nuclide has an atomic number that is one unit less than the parent. Also, as consequence of a positron emission, a mass equivalent of two electrons are created by the conversion of a proton to a neutron (**Scheme 1**) in where 1.02 MeV is needed to create these two particles. Taking this into account, positron emission takes place only when the energy difference between the parent and daughter nuclides is equal to or greater than 1.02 MeV.

$$ {}^{1}_{1}p \longrightarrow {}^{1}_{0}n + {}^{0}_{+1}e + \nu $$

Scheme 1. β^+ decay process

A particular β^+ decay process may also happen when a nucleus has a smaller N/Z ratio compared to the stable nucleus. This process is called electron capture (**Scheme 2**), in which an electron is captured from the extra nuclear electron shells, transforming a proton into a neutron and emitting a neutrino. For this process to occur, the energy difference between the parent and daughter nuclides is usually, but not necessarily, less than 1.02 MeV. Nuclides having an energy difference greater than 1.02 MeV may also decay by electron capture. As larger the energy difference gets, higher the positron decay will be [13].

$$ {}^{1}_{1}p + {}^{0}_{+1}e \longrightarrow {}^{1}_{0}n + \nu $$

Scheme 2. Electron capture process

Fluorine-18 decays (**Figure 4**) largely by positron emission (97%) with a half-life of 109.77 min and relatively low energy (maximum 0.635 MeV) thus the emitted positron has short mean range (2.39 mm in water)[23].

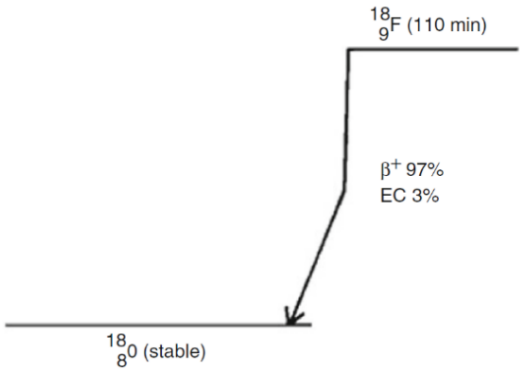

Figure 4. Decay of ^{18}F

At the end of the path of β^+ particles (0-10 mm, depending on its kinetic energy and density of the tissue), positrons combine with electrons and are thus annihilated, each event giving rise to two photons of 511 keV that are emitted in opposite directions. These photons are referred to as annihilation radiations (**Figure 5**) and this phenomenon is the basis of the positron detection system (also known as coincidence detection system) [7].

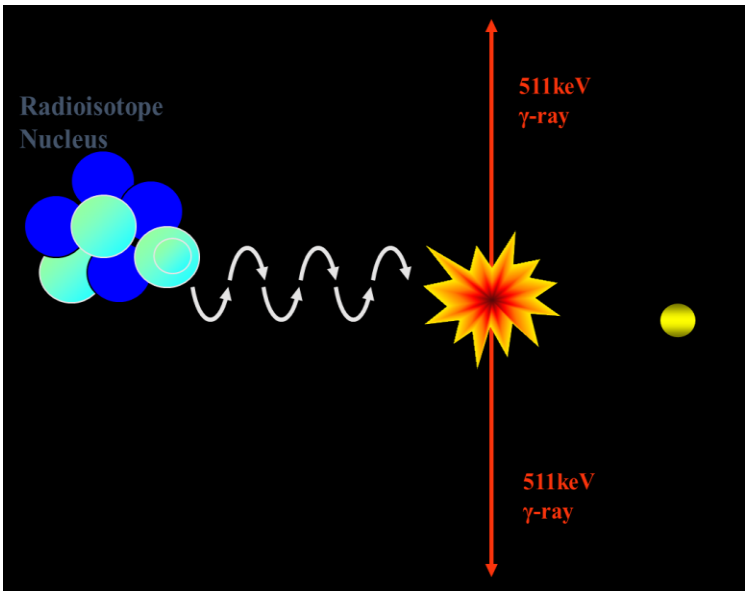

Figure 5. Positron-electron annihilation process after collision producing two gamma rays of 511 keV that are emitted in opposite directions

1.4 PET imaging.

Positron emission tomography (PET) is a non-invasive imaging modality that uses the principle of coincidence detection of two annihilation photons (**Figure 5**) to measure radiotracer

distribution within tissues. This information, when combined with assumptions based on physiology or biochemical models, can be used to assess biological processes *in vivo*.

In a PET camera, when opposing 511 keV gamma rays reach simultaneously two detector crystals, a flash of light (scintillation) is produced and due to the photoelectric effect, released electrons then magnified their energy in a photomultiplier tube [24] (**Figure 6**). By processing the information of millions of annihilations using mathematical techniques, a map of the activity distribution within the field of view over time is generated producing a dynamic image and time-activity curve (TAC) for various regions of interest (ROI) in the subject (**Figure 6**) [25]. Combining the maximal positron range (which is unique for each radioisotope) with the crystal detector properties and its photomultiplier tube, determine the final resolution of PET images (typically 4-6 mm). Recently, the spatial resolution of newer clinical systems (mainly dedicated for brain imaging) has been improved up to 2.5 mm and for small animal PET imaging systems, resolutions of 0.8-1.5 mm can be achieved [26].

PET is usually used in combination with other imaging modalities, such as radiography, computed tomography (CT), or magnetic resonance imaging (MRI). The use of PET in combination with these anatomy-based imaging technique offers advantages of a simultaneous assessment of both anatomical and functional processes. These hybrid imaging techniques provide unique opportunities in diagnosing diseases and evaluating its treatment which is the base of future personalized medicine [27].

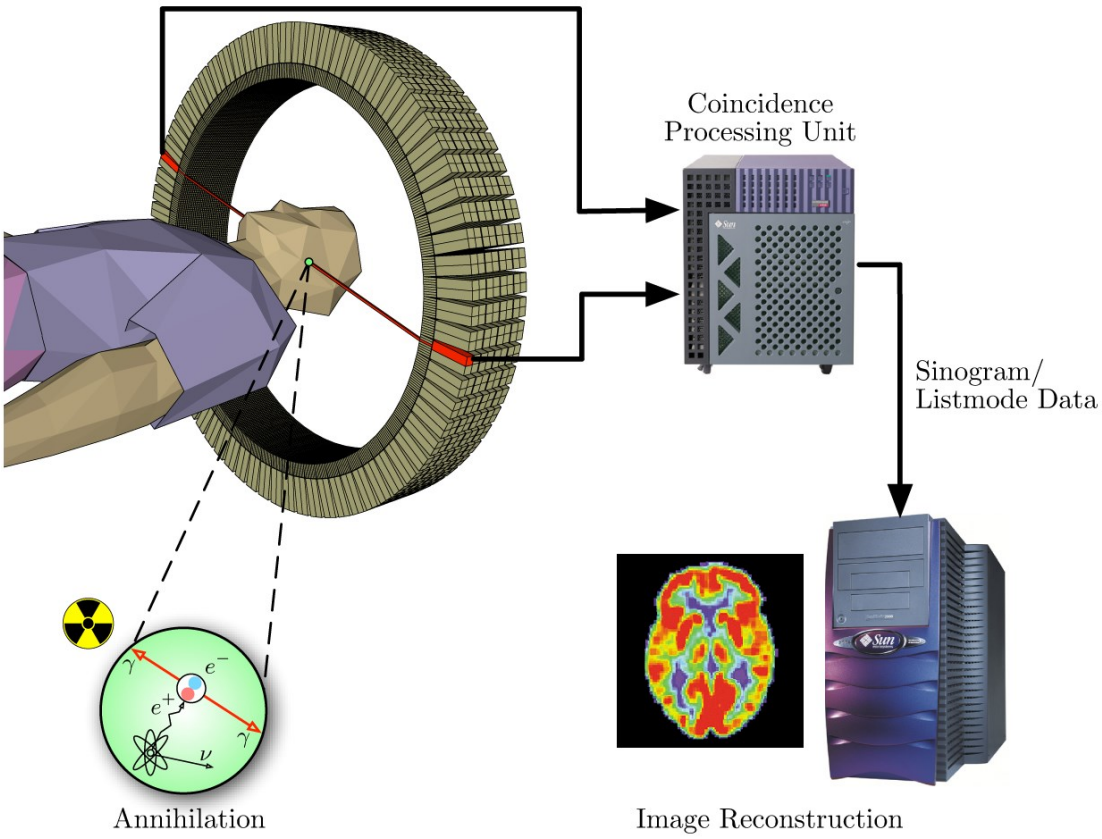

Figure 6. PET acquisition process

1.5 AM receptor radiotracers.

Many molecular imaging agents have demonstrated potential utility in the diagnostic of pulmonary vascular disease but very few have been tested in human subjects. Nonetheless, a non-invasive SPECT/PET imaging modality is currently unavailable to provide direct information on the pathophysiology processes affecting pulmonary vasculature (i.e. endothelium, adventitia). Recent studies have developed agents targeting angiotensin-converting enzyme, norepinephrine transporter and adrenomedullin receptors for imaging of pulmonary vasculature [28]. An extensive review of the state-of-art in SPECT and PET imaging of adrenomedullin receptors is provided in Chapter 2.

1.6 Chelation chemistry

Chelation is called to formation process in where two or more coordinate bonds are formed between a polydentate ligand and a single central atom. Chelators are usually organic compounds containing donor atoms such as O, N and S which share their electron pairs with transition elements (mainly metals) to form a stable coordination compound with a particular coordination number and geometry [29].

In radiochemistry, biological and radioactive drug components are often coupled through the use of bifunctional chelators with the dual purpose of radiometal complexation and bioconjugation. An ideal chelator for radiopharmaceutical preparation should efficiently bind the radiometal in high complexation yields, in aqueous medium, at low temperature and short reaction time. It is important that complexation with the radiometal be stable *in vivo* in order to prevent the release of the free radiometal (kinetic inertness) and non-selective binding imaging. Macrocyclic chelators possess a geometric constrain that partially organize metal ion binding sites by decreasing entropic losses upon the metal complexation. In contrast, acyclic chelators follow a more drastic change in physical and geometry orientation in order to arrange donor atoms to coordinate the metal ion, undergoing a significant decrease in entropy which is thermodynamically unfavorable. For this reason, most chelation of radiometals takes place using macrocyclic chelators which are known to form a stable entity and a more kinetically inert complexes than acyclic chelators [30].

1.6.1 Aluminum [^{18}F]Fluoride

Aluminum [^{18}F]Fluoride is an attractive method for radiofluorination by chelation of peptides and proteins. Recently, this emerging approach has been used to label peptides in aqueous solutions increasing the reaction yield, facilitating the purification and reducing considerably the total synthesis time [31].

Aluminum as cation exist most commonly at oxidation state +3, but some compounds are known at lower oxidation states of +1 and others at +2 in gas phase. Following the Pearson classification, Al^{3+} behaves as a Lewis acid thus forming stable coordinates with hard Lewis bases containing electron pair donors such as H_2O, ROH, RNH_2, OH^-, F^-, Cl^-, etc [32]. Among more than sixty metal ions, Al^{3+} binds to F^- the most strongly (>670 KJ/mol) with the exception of Sc^{3+}. Known molecular geometries of aluminum with F^- undergoes tetrahedral, trigonal bipyramidal and octahedral complexes such as $(AlF_4)^-$, $[AlF_4(OH)]^{2-}$ and $(AlF_6)^{3-}$ with four, five and six coordination number respectively [33]. Previous studies revealed that AlF-binary complex formation is a pH-depending process. When the pH is too high, aluminum would form insoluble hydroxide complexes. At contrary, if the pH it is too low, then the preferred fluoride species in the equilibrium would be HF. Also, at lower fluoride concentrations, aluminum appears as monofluoride species like $(AlF)^{2+}$ that could form a stable complex with a suitable chelator [34].

McBride *et al.* [35] were the first to explore the potential of $Al^{18}F$-method in radiopharmaceutical chemistry (**Figure 7**). As a proof-of-concept, the authors succeeded to complex $Al^{18}F$ to a DTPA-conjugated peptide in high yields (**Figure 8a**). However, by using this acyclic octadentate ligand, the formed complexes were not sufficiently stable for *in vivo*

applications. The conclusion drawn from this initial study was the needs of finding a thermodynamic stable and kinetic inert Al^{18}F-ligand that remains intact for several hours *in vivo*.

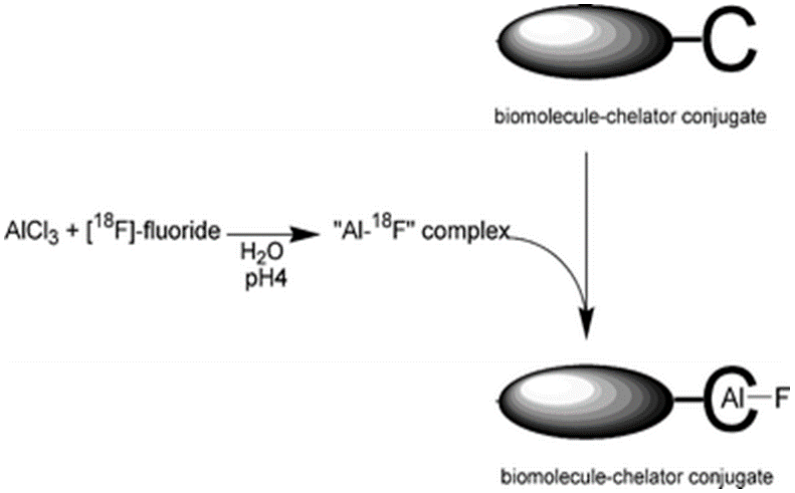

Figure 7. Al^{18}F radiolabeling approach for biomolecules. Found in Smith, G *et al.* [36]

1.6.2 NOTA

NOTA-chelator (**Figure 8c**) was first reported in the mid-80s as small version of DOTA (**Figure 8b**), in the search of a more stable chelator for lanthanides as potential MRI contrasting agents [37, 38]. NOTA is a hexadentate chelate with three nitrogen and three oxygen donor atoms, that tend to form stable coordination bond with d-orbitals of transition metals of smaller atomic radii. Thus, it is probably the most successful chelator for use with $^{67/68}$Ga and ^{64}Cu due to its favorable radiolabeling conditions and excellent *in vivo* stability.

In previous studies, Al^{3+} was found to form highly stable octahedral complexes with NOTA towards acid catalyzed dissociation by ^{27}Al-NMR spectroscopy [39]. Also, the Al^{18}F complex has pentadentate binding to NOTA, with the sixth binding site of the aluminum filled with the fluoride ion. Thus, the SCN-Bz-NOTA (**Figure 8c**) modified peptide IMP449 was successfully radiolabeled

with Al^{18}F in 5-20% yield. After demonstrating stability in serum for 4h, the product was able to bind its receptor by PET imaging using nude mice bearing the human colon cancer xenograft LS174T [40].

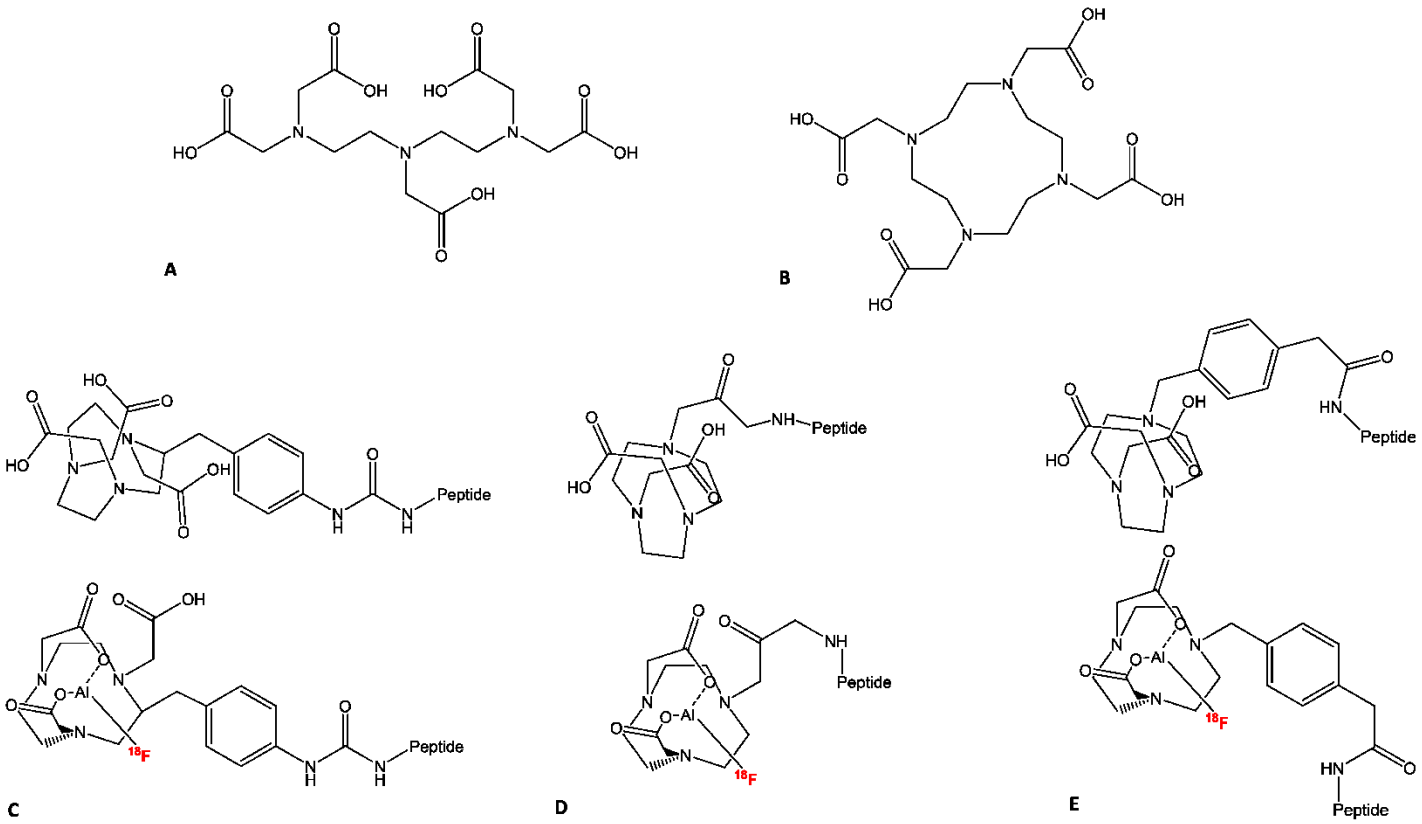

Figure 8. Chemical structures of DTPA (**a**), DOTA (**b**), NOTA-SCN-Bz-peptide (top) and the [^{18}F]AlF-NOTA-SCN-Bz-peptide conjugate (bottom) (**c**), NOTA-peptide (top) and the [^{18}F]AlF-NOTA-peptide conjugate (bottom) (**d**), NODA-MP-peptide (top) and the [^{18}F]AlF-NODA-MP-peptide conjugate (bottom) (**e**)

Further experiments evidenced that efficient and stable binding of radiometals by chelates is highly influenced by the chelate structure. D'Souza *et al.* [41] studied the solid-state X-ray structure of Al^{18}F in an improved NOTA chelator: 1,4,7-triazacyclononane-1,4-diacetate motif with a methylphenylacetic acid (NODA-MPAA) (**Figure 8e**). Considering their findings, it was

experimentally demonstrated that N_3O_2-type chelators can from stable mononuclear octahedral complexes with aluminum containing a single coordination site for binding fluoride. Therefore, pentadentate ligands such as NOTA-NHS ester (**Figure 8d**) or NODA-MPAA (**Figure 8e**) are desired for high complexation yields, leaving only one binding site open for the fluorine-18 ion.

1.7 AT_1 receptors.

The octapeptide hormone Ang II plays a central role in the regulation of blood pressure. As a part of the Renin-Angiotensin System, Ang II acts mainly by stimulating the AT_1Rs which are expressed in the kidneys, adrenal glands, heart, brain, and vasculature [42]. Previous studies suggested that there are alterations in the expression levels of the AT_1Rs associated with cardiovascular and renal diseases such as hypertension, cardiac and renal failures; but the regulatory mechanism that determines AT_1R expression and disease progression is not well understood yet [43].

AT_1R is part of the seven-transmembrane (7TM) superfamily of G protein-coupled receptors (GPCRs). New advances in the determination of the crystal structures of AT_1R confirms the postulates 7TM α-helical architecture with three extracellular loops (ECL1-3) and three intracellular loops (ICL1-3) (**Figure 9**) in where critical ligand binding residues (Arg^{167}, Tyr^{35} and Thr^{84}) for the so-called "sartan" family of selective AT_1R blockers (ARBs) have been identified [44].

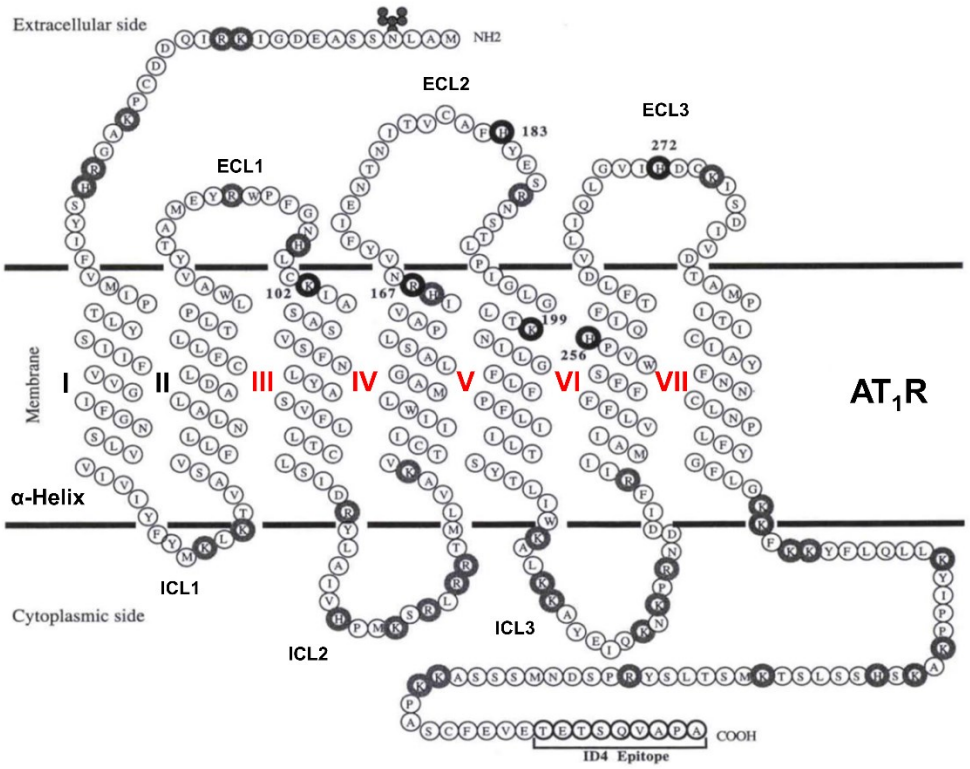

Figure 9. Representation of AT_1 receptor. 7TM α-helical are presented with Greek numbers (in red the helices that are important for binding). Adapted from Noda *et al.* [44].

1.8 Candesartan.

Candesartan is an ARB approved by FDA in 1998 as a treatment of hypertension. This compound selectively binds to AT_1R giving a long-lasting blockage and suppression of the response by Ang II. It displays a higher binding affinity (IC_{50} 0.6 nM) compared to other selective AT_1R antagonists (Losartan, IC_{50} 20 nM and Valsartan, IC_{50} 2.7 nM) [45]. Thus, a radiopharmaceutical based on the parent structure of Candesartan with similar pharmacological binding properties could exhibit some potential as a molecular imaging agent of AT_1 receptors.

1.9 AT_1 receptor radiotracers.

AT_1R radioligands have been previously developed for SPECT and PET imaging but so far only few of them are based on Candesartan. The Johns Hopkins PET group developed the first AT_1R PET radioligand [^{11}C]MK-996 by *N*-benzoylation with [α-^{11}C]benzoyl chloride in 1995 (**Figure 10a**). The compound was produced with an average MA of 1162 mCi/μmol in 38 min including reformulation [46].

Close structural analogues [^{11}C]L-162,574 and [^{11}C]L-159,884 were also prepared in low yields by Johns Hopkins PET group (**Figure 10b**). High AT_1R binding was obtained in canine adrenals and renal cortex demonstrating the tracer potential to examine *in vivo* AT_1R binding in dogs. Nonetheless, [^{11}C]L-159,884 was rapidly metabolized in humans [47] limiting its future applications. This group also produced the [^{11}C]KR31173 (**Figure 10c**) in low yields (at high MA >7000 mCi/μmol) and without remarkable brain uptake. Transient regional AT_1R up-regulation was detected with [^{11}C]KR31173 in the infarcted area by small-animal PET imaging [48].

Verjans *et al.* [49] reported the radiolabeling of Losartan with ^{99m}Tc for SPECT imaging. Losartan was attached with an N_4-type chelator and four PEG groups as linkers (**Figure 10d**). No data were shown for radiolabeling yield or MA. Compared to controls, nearly 2.4-fold higher AT_1R binding was observed in the infarct region of a mouse with permanent coronary artery ligation. However, the authors concluded that it is necessary to engineer new probes with better targeting characteristics for realization of potential clinical application.

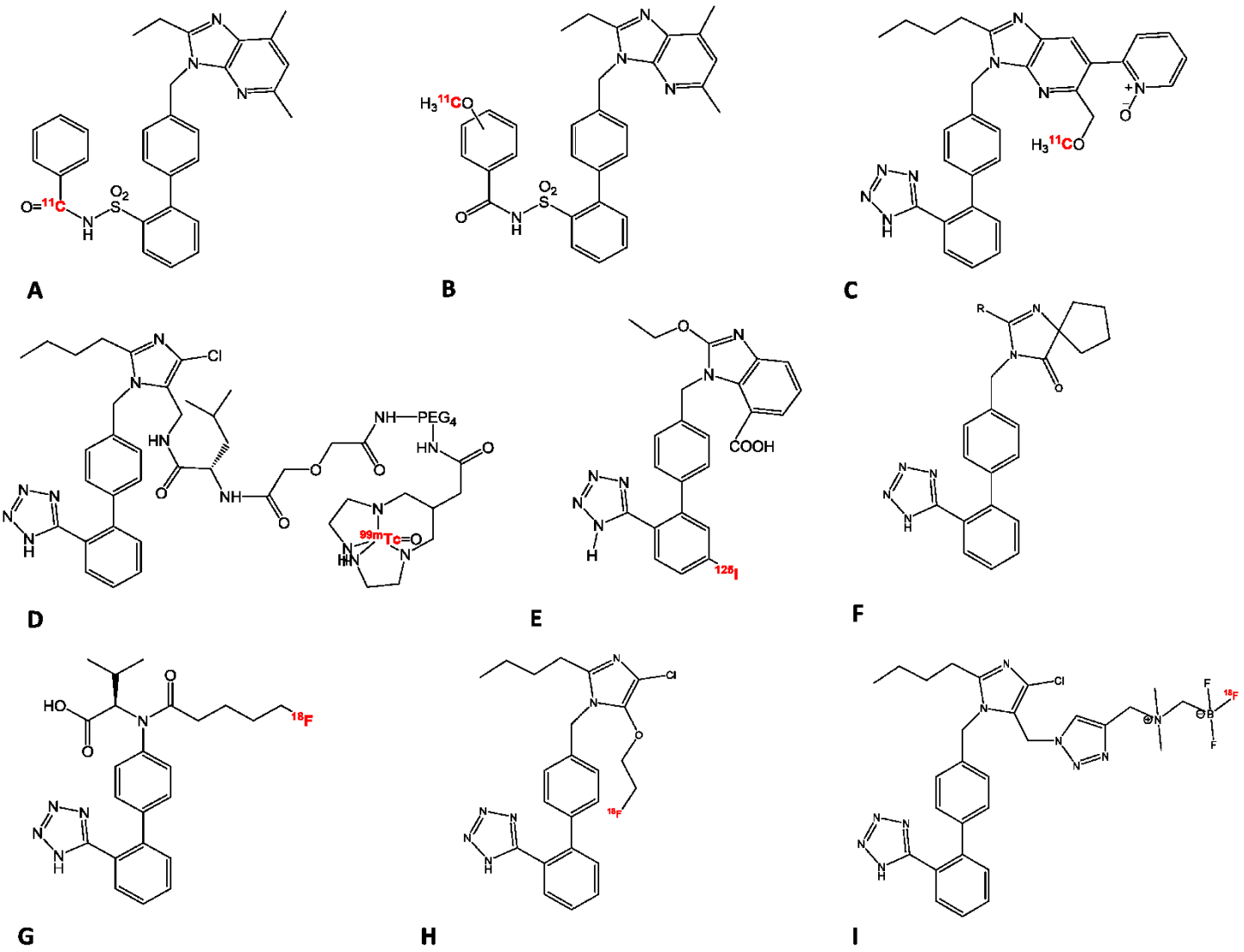

Figure 10. AT_1 receptor radiotracers. [^{11}C]MK-996 (**a**), [^{11}C]L-162,574 *m*- O$^{11}CH_3$ and [^{11}C]L-159,884 *p*- O$^{11}CH_3$ (**b**), [^{11}C]KR31173 (**c**), [^{99m}Tc]Tc-Losartan (**d**), [^{125}I]I-Candesartan (**e**), R=-CH-[^{18}F]F-$(CH_2)_2CH_3$ α-[^{18}F]F-Irbesartan, R=-$(CH_2)_3$[^{18}F]F δ-[^{18}F]F-Irbesartan (**f**), [^{18}F]FV45 (**g**), [^{18}F]FEtLos (**h**), and [^{18}F]AMBF$_3$Los (**i**).

Sanad *et al.* [50] reported the radioiodination of Candesartan with iodine-125 and its biological evaluation as potential tracer for cardiovascular disorder detection (**Figure 10e**). Using the chloramine-T method for radioiodination, the radiochemical yield of [^{125}I]I-Candesartan was

98%. No data were reported for MA. The authors stated that heart uptake of [^{125}I]I-Candesartan was higher than [^{125}I]I-Valsartan and [^{99m}Tc]Tc-Valsartan at same time post-injection. While the authors concluded that [^{125}I]I-Candesartan can be easily and safely used in myocardial SPECT imaging, it should be noted that nuclear properties of iodine-125 (half-life 59.43 days and gamma energy 35.5 keV) are not ideal for clinical applications. The authors suggest that further clinical trials are required to evaluate the potential of [^{125}I]I-Candesartan as cardiac SPECT imaging agent. However, due to the ideal gamma-ray characteristics, selection of the I-123 labeled Candesartan derivative would have been a better choice for SPECT imaging.

Two F-18 derivatives of Irbesartan were reported by Hoffman *et al.* [51] in 2018 (**Figure 10f**). Radiofluorinations at α- and δ-positions of tosyl precursors were carried out in 11% radiochemical yield and 94% radiochemical purity. Considering the results of *in vitro* competition studies, α-F-Irbesartan (IC_{50} 6.6 nM) was evaluated in rats and pigs by PET imaging. *In vivo* studies revealed that α-[^{18}F]F-Irbesartan accumulated in all relevant tissues expressing AT_1Rs such as heart, kidney and lung. The tracer uptake in these organs was proven to be specific to AT_1R due to reduction of uptake following blocking studies with Irbesartan (5 mg/kg). However, PET imaging in healthy heart was difficult due to low cardiac retention and high liver uptake. The study concluded that more work is needed to further explore its applicability for broad uses. Following the radiofluorination approach of α-[^{18}F]F-Irbesartan, the ^{18}F Valsartan-derivative FV45 (**Figure 10g**) was synthesized in 21.8 % yield and more than 99% radiochemical purity. No data were reported for MA. However, PET studies in rats revealed a fast and clear kidney uptake that was selectively blocked by a pre-treatment with valsartan. The authors concluded that [^{18}F]FV45 had almost identical AT_1R binding affinity as its lead compound Valsartan, facilitating the translational work to humans as a potential RAS PET imaging agent [52].

Recently, two tracers based on Losartan were labeled with F-18 using two different methods [53]. [^{18}F]Fluoroethyl-Losartan (**Figure 10h)** was radiolabeled by ^{18}F-fluoroakylation of Losartan potassium using the prosthetic group 2-[^{18}F]fluoroethyl tosylate in low yield (2.7%), low MA (38 Ci/mmol) and high radiochemical purity (>95%). [^{18}F]Ammoniomethyltrifluoroborate-Losartan ([^{18}F]AMBF$_3$Los) (**Figure 10i)** was prepared following ^{18}F-^{19}F isotopic exchange in 11% radiochemical yield and MA of 2900 Ci/mmol. Higher binding affinity was found with AMBF$_3$Los (Ki=7.9nM) in a competition assay using AT$_1$R-expressing membranes. Then, the tracer was evaluated in rats via PET imaging with AMBF$_3$Los blocking revealing specific uptake in the kidney cortex. Taking into account their findings, the authors concluded that [^{18}F]AMBF$_3$Los might be considered a valuable PET imaging tracer for monitoring AT$_1$R expression in several diseases.

1.9.1 Our AT1R Losartan derivative radiotracers

DaSilva's group reported the synthesis of [^{11}C]methyl-Losartan, [^{11}C]methyl-EXP3174, and [^{18}F]FPyKYNE-Losartan, (**Figure 11a** and **b**) in good yields, high radiochemical purity and reasonable synthesis time [54-57]. [^{11}C]methyl-Losartan and [^{11}C]methyl-EXP3174 were synthesized by O-[^{11}C]methylation of Losartan and its active metabolite EXP3174 respectively. Both radiotracers displayed high kidney-to-blood ratios which was further confirmed to correspond to [^{11}C]methyl-EXP3174 specific binding for AT$_1$R. Regardless the high selectivity for AT$_1$ over AT$_2$ and MAS receptors, [^{11}C]methyl-Losartan exhibited the presence of radiometabolites in the kidney with similar pharmacological binding profile to the parent tracer which is detrimental for AT$_1$R quantification by PET imaging. This study concluded that [^{11}C]methyl-EXP3174 displayed favorable uptake kinetics and binding profile to AT$_1$Rs supporting further studies to assess its full potential as PET imaging probe [58].

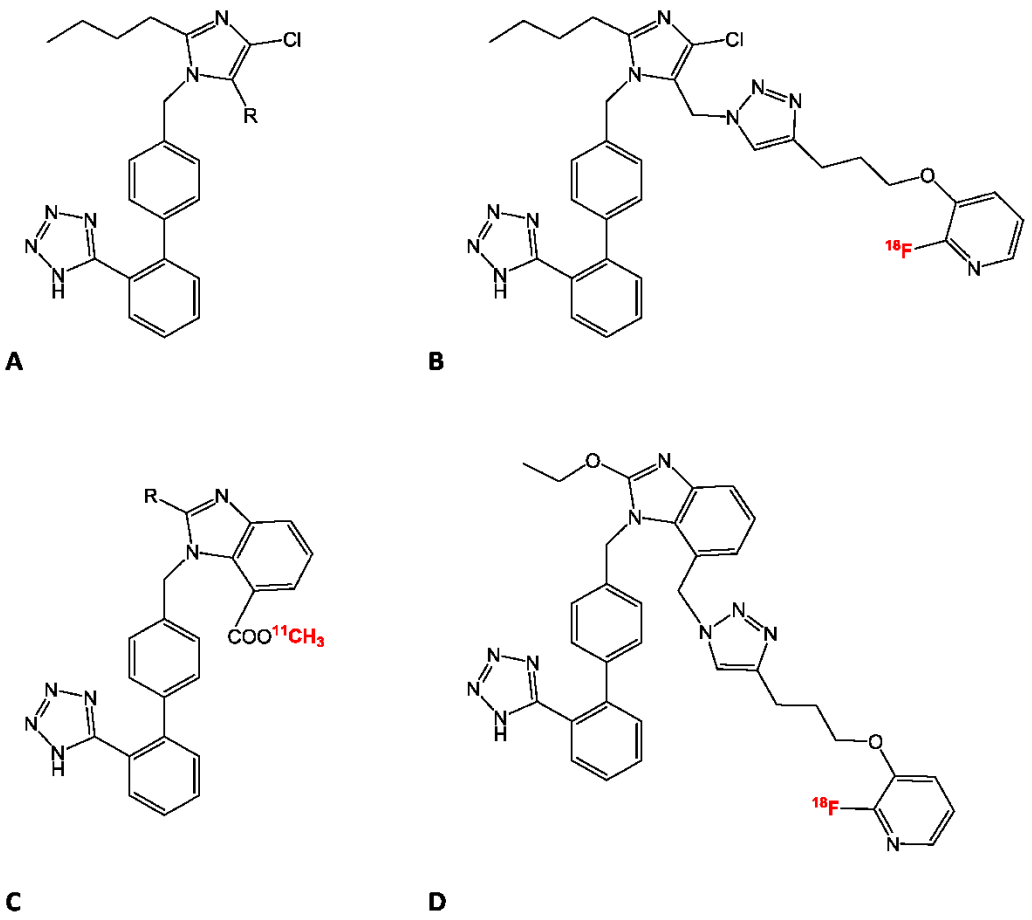

Figure 11. DaSilva's group AT_1 receptor radiotracers. [^{11}C]Methyl-Losartan R= -$CH_2O^{11}CH_3$ and [^{11}C]Methyl-EXP3174 R= -$COO^{11}CH3$ (**a**), [^{18}F]FPyKYNE-Losartan (**b**), [^{11}C]TH4 R= =O and [^{11}C]Methyl-Candesartan R= -OC_2H_5 (**c**), and [^{18}F]fluoropyridine-Candesartan (**d**).

[^{18}F]FPyKYNE-Losartan ([^{18}F]fluoropyridine-Losartan) was synthesized via click chemistry using a two-step, double reactor TRACERlab® FX N Pro GE Healthcare module in 7-14% overall process yield. MA of 200-4200 mCi/μmol were achieved. PET studies in rats and pigs displayed high uptake in the AT_1R-rich kidneys with good contrast compared to surrounding tissues. Blocking studies exhibited high binding selectivity for renal AT_1R over AT_2R. In addition, [^{18}F]FPyKYNE-Losartan was metabolized rapidly in plasma to mostly hydrophilic labeled

compounds suggesting a potentially advantageous metabolic profile. However, in order to prevent saturation of receptors and be able to image cardiac AT_1Rs, the MA needs to be above 7000 mCi/µmol [59].

1.9.2 Structure-activity relationship studies (SAR) justifying Candesartan labeled derivatives

Based on reported SAR studies by Kubo *et al*. [60], large prosthetic groups can be introduced at the imidazole 7-position of Candesartan without changing its binding properties and pharmacological functions. Coupling a prosthetic group at this position requires a chemical "inert" bond to enzymatic cleavage. C-C bond *in vivo* cleavage by enzymes does not occur with unfunctionalized methylene carbons, olefins, and aromatic molecules and requires oxidation reactions at two adjacent carbon atoms following a multi-step mechanism [61]. [^{11}C]methyl-Candesartan and its des-ethyl derivative [^{11}C]TH4 (**Figure 11c**) were synthesized in high yields of 50-70% from [^{11}C]methyl iodide and with specific activities of 300-1500 mCi/µmol. Even when both tracers displayed high uptake in the kidney, [^{11}C]TH4 exhibited reduced selectivity for AT_1R compared to [^{11}C]methyl-Candesartan [54]. Initial *in vivo* PET modeling performed with [^{11}C]methyl-Candesartan evidenced its ability to detect changes in AT_1R density and/or affinity in the rat kidney. However, the quantification and modeling demanded corrections due to the presence of the hydrophobic metabolite [^{11}C]TH4 bound to renal AT_1R [62].

Few weeks ago, our group published the synthesis of the novel tracer [^{18}F]fluoropyridine-Candesartan (**Figure 11d)** labeled with the [^{18}F]FPyKYNE prosthetic *via* the copper-catalyzed azide-alkyne cycloaddition at the imidazole 7-position in 10% yield and high radiochemical purity (≥97%) [63]. Using an improved methodology, the prosthetic group [^{18}F]FPyKYNE was completely separated from its nitro precursor allowing the production of the tracer in MA greater than 10 000 mCi/µmol. *Ex vivo* biodistribution and autoradiography studies revealed specific binding of

[^{18}F]fluoropyridine-Candesartan in AT_1R-rich tissues such as kidney cortex. These favorable results support conducting further studies to assess the full potential of [^{18}F]fluoropyridine-Candesartan.

Interestingly, the radiosynthesis of 4-[^{18}F]fluoroiodobezene ([^{18}F]FIB) has recently been reported with high radiochemical yields, relatively facile purification, fast conjugation and versatile applications [64]. Following the Sonogashira cross-coupling reaction, [^{18}F]FIB has been conjugate to alkyne modified peptides forming an alkyne-benzene (sp-sp^2 carbon-carbon) planar arrangement and exhibiting high *in vivo* stability of final ethynyl-4-[^{18}F]fluorobenzene moiety [65]. Using a similar approach, Candesartan could also be labeled with [^{18}F]FIB at the imidazole 7-position and possibly display a better metabolic profile and biodistribution than [^{11}C]methyl-Candesartan, facilitating the quantification of AT_1Rs *via* PET imaging.

1.10 Automation of ^{18}F processing and reactions

Due to very large quantity of radioactivity, radiopharmaceutical manufacturing facilities use automated synthesis modules controlled by computers to carry out the production of a radiolabeled compound. A wide range of synthesis modules are available from various manufacturers, but most of them allows the automatic ^{18}F post-processing, radiofluorination reaction, purification and re-formulation.

1.10.1. Semi-automatic system for production of Al^{18}F

As a common step in mostly all radiofluorination reactions, cyclotron produced ^{18}F needs to be purified from the target O-18 water. In general, the target chamber is made of inert metal

such as silver, titanium, niobium or tantalum. Activation of the foil by the proton beam is unavoidable, leading to the formation of unwanted radioactive metal ions that can leach into the target water and somehow affect the Al^{18}F complexation yield. Radiometals such as ^{51}Cr, ^{46}Sc, $^{55/56/57/58}$Co and ^{57}Ni have been found in the target water [66] and all of them could form stable complexes with a NOTA-conjugate molecule.

Due to the lack of a system to purify ^{18}F and to produce the binary Al^{18}F complex in extremely small volumes that is necessary for the labeling of peptides present in small quantities, we developed a semi-automatic system capable of doing so. The system depicted in **Figure 12**, consisted mainly of two solenoid valve and a Valco 12 port valve. Cyclotron produced ^{18}F was transfer from the target and trapped onto the small anion-exchanger cartridge.

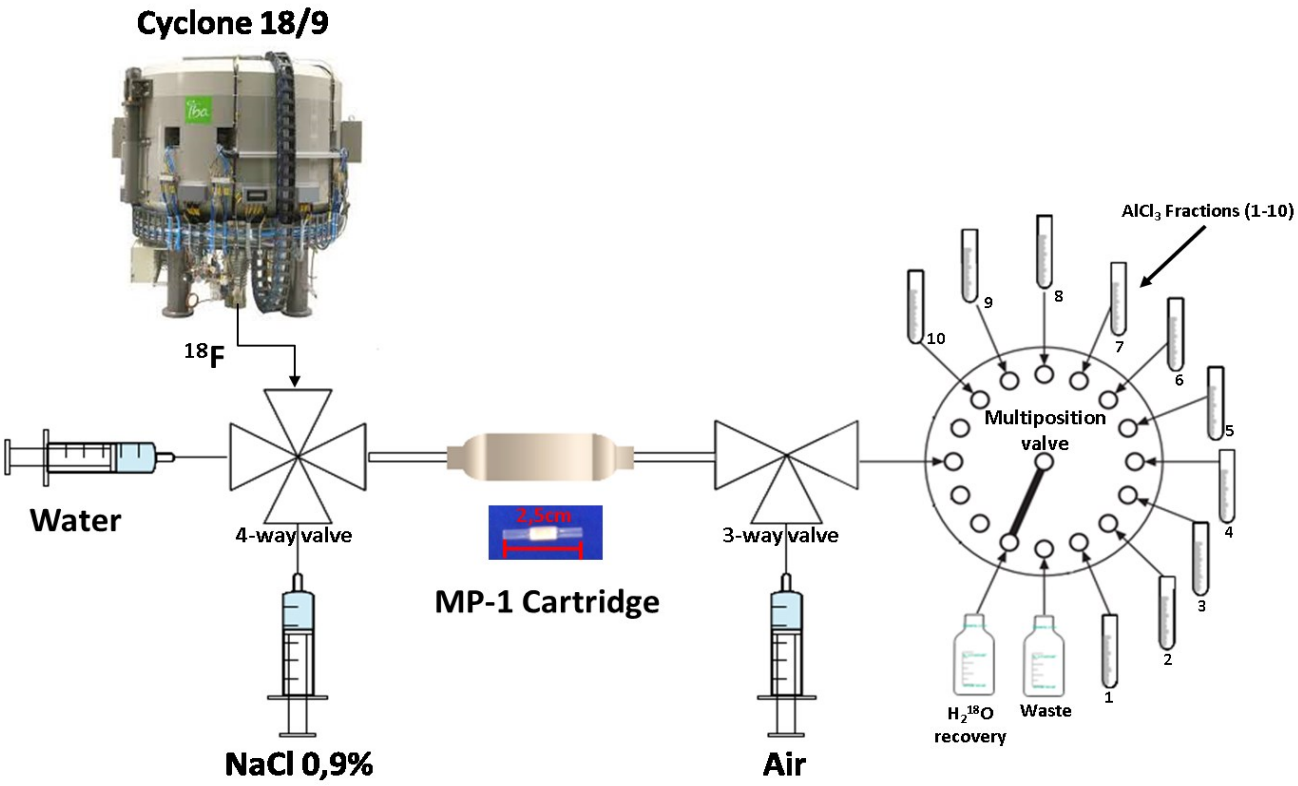

Figure 12. Semi-automatic system for ^{18}F-purification and production of concentrated [^{18}F](AlF)$^{2+}$.

The cartridge was then rinsed with 3 mL water to remove radiometal contaminants. Trapped F-18 was subsequently eluted with small volumes of 0.9% NaCl and dispensed semi-automatically via the multiport port valve into small vessels containing the $AlCl_3$. Using this system, pure and highly concentrated $Al^{18}F$ was produced directly in the reaction vial minimizing the loses, reducing the radiation exposure and simplifying considerably the radiolabeling process.

1.10.2. Automatic synthesis module

Introduction of ^{18}F via direct nucleophilic substitutions in a desired position of the molecule is not always possible. Therefore, a complex multi-step chemical process involving labeling of a prosthetic group for incorporation of ^{18}F into a desired molecule is often required. In cases like these ones, an automatic synthesis module is always useful [67].

The multi-step chemical process carried out in the module usually starts with the trapping of [^{18}F]fluoride and recovery of oxygen-18 enriched water (**Figure 13**, section A). We use the Synthra® RNPlus Research dual-reactor dual-HPLC system at the CRCHUM radiochemistry lab for the production of the novel [^{18}F]FB-Candesartan. Then ^{18}F is eluted with a mixture of potassium carbonate and kryptofix 222. Kryptofix 222 is a cyclic crown ether, which binds the potassium ion, preventing the formation of [^{18}F]KF and thus rendering [^{18}F]F^-more nucleophilic.

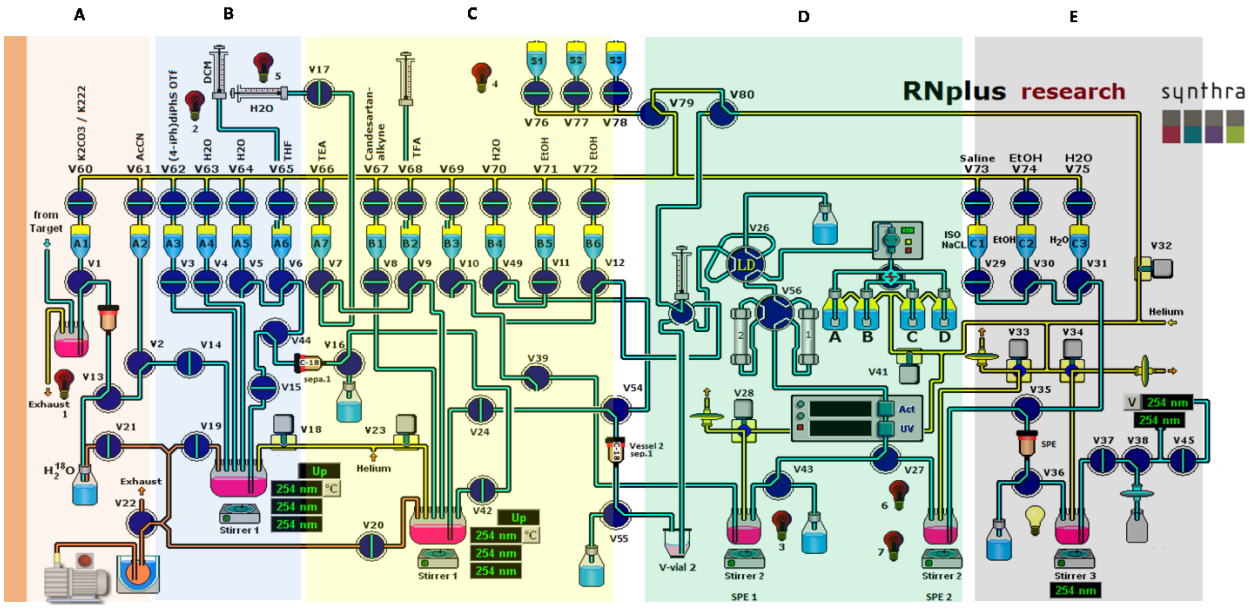

Figure 13. Automatic synthesis module for a two-step radiofluorination. ^{18}F-purification and ^{18}O recovery (**A**), azeotropic distillation and radiofluorination of prosthetic group (**B**), prosthetic group coupling reaction (**C**), semi-prep HPLC purification (**D**) and re-formulation and final filtration (**E**)

After the [^{18}F]F^- is eluted into the reactor 1, it is necessary to evaporate any residual water from the solution via azeotropic distillation with acetonitrile. Subsequently, the radiofluorination of prosthetic group is taking place in the first reactor by a nucleophilic substitution reaction **(Figure 13**, section B). When the first reaction is completed, a semi-preparative HPLC purification is often performed in between reaction 1 and 2 (**Figure 13**, section D). After that, the coupling reaction between the prosthetic group and the second precursor takes place in reactor 2 following a fast reaction such as the 1,3 Huisgen cycloaddition (**Figure 13**, section C). The final product is again purified by semi-preparative HPLC (**Figure 13**, section D) and finally reformulated in normal saline for parenteral use (**Figure 13**, section E).

1.11 Hypothesis

The primary hypotheses of this doctoral proposal are: 1) for the AM project: that the novel human NOTA-AM derivative DFH17 labeled by the Al^{18}F method ([^{18}F]AlF-DFH17) in high yields and high radiochemical purity will demonstrate appropriate binding properties, such as selective pulmonary uptake and favorable dosimetry for PET imaging of pulmonary circulation. 2) for the AT_1 project: that the novel [^{18}F]FB-Candesartan can be synthesized in good yields and MA.

1.12 Objectives

The objectives of this doctoral proposal are:

Objectives 1:

1. Develop a semi-automatic elution method to produce very high concentrated [^{18}F]AlF.
2. Perform complexation experiments with [^{18}F]AlF and pentadentate NOTA chelator.
3. Optimize the radiolabeling conditions to yield pure DFH17 with [^{18}F]AlF considering the results of chelation experiments.
4. Perform the quality control of [^{18}F]AlF-DFH17 for animal studies.
5. Evaluate the potential of [^{18}F]AlF-DFH17 *in vitro* (stability) and *in vivo* by animal PET imaging

Objectives 2:

1- Synthesize the precursor (tetrazole-protected alkyne Candesartan) and the standard (FB-

Candesartan).

2- Optimize the radiosynthesis of [^{18}F]FIB prosthetic group.
3- Radiolabel the alkyne Candesartan precursor with [^{18}F]FIB following the Sonogashira cross-coupling reaction.
4- Automate the radiosynthesis and purification of [^{18}F]FB-Candesartan in high radiochemical purity using a synthesis module.
5- Analyse the final formulation of [^{18}F]FB-Candesartan by analytical methods.
6- Evaluate [^{18}F]FB-Candesartan *in vitro* plasma stability by column-switch HPLC analyses.

1.13 Manuscripts

As part of these PhD research projects, I have been involved with many aspects of the AM and AT_1R tracer development that culminated in three peer-reviewed manuscripts (all as first author) that will be briefly overviewed below.

Manuscript 1: "SPECT and PET imaging of adrenomedullin receptors: a promising strategy for studying pulmonary vascular diseases" Am J Nucl Med Mol Imaging 2019;9(5):203-215 www.ajnmmi.us /ISSN:2160-8407/ajnmmi0099437.

The objective of this manuscript was to review all published radiotracers for molecular imaging of AM receptors in pulmonary vascular diseases. In this study, all AM tracers are presented as separated subsections in where their synthesis, *in vitro* and *in vivo* evaluation are extensively reviewed. Of particular interest is the section dedicated to the novel PET tracer Al[^{18}F]F-DFH17, in where previously unpublished data of PET imaging in rats, dog and primate are also presented and discussed. The manuscript concludes that the tracers [^{99m}Tc]Tc-

PulmoBind and Al[^{18}F]F-DFH17 are promising agents for SPECT/PET imaging of pulmonary vascular diseases involving AM receptors.

Manuscript 2: "Al[^{18}F]F-complexation of DFH17, a NOTA-conjugated adrenomedullin analog, for PET imaging of pulmonary circulation" Nucl Med Biol 2018; 67:36-42. doi:10.1016/j.nucmedbio.2018.10.003

This article describes the synthesis, radiolabeling and *in vivo* evaluation of the novel adrenomedullin derivative DFH17 as a potential PET imaging agent of pulmonary hypertension and pulmonary embolism. Highly concentrated Al^{18}F was produced using an in-house semi-automatic system. Then, as result of a complexation study with pentadentate NOTA, the best Al^{18}F-to-NOTA ratios were applied to optimize the radiosynthesis of [^{18}F]AlF-DFH17. Various parameters such as fluorine-18 activity, concentration of $AlCl_3$ and the effects of hydrophilic organic solvent (aqueous vs ethanol 50%) in the reaction mixture were also studied. As a result, the tracer [^{18}F]AlF-DFH17 was produced in 22-38% yield and radiochemical purity. PET evaluation in rats revealed high lung-to-background ratios and no defluorination *in vivo*. The study concluded that [^{18}F]AlF-DFH17 appears to be a promising PET ligand for imaging the integrity of pulmonary microcirculation.

Manuscript 3: "Development of a novel [^{18}F]fluorobenzyl derivative of the AT_1 Receptor antagonist Candesartan" (Submitted for the Journal of Labelled Compounds and Radiopharmaceuticals).

The aim of this study was to synthesize the novel Candesartan derivative [^{18}F]FB-Candesartan using [^{18}F]FIB as prosthetic group. The manuscript explores the Sonogashira cross-coupling reaction, a reaction not widely used in radiochemistry, to produce a new Candesartan derivative

with potentially better metabolic profile and biodistribution as other existing ^{18}F-labeled AT_1 derivatives. First, the synthesis of [^{18}F]FIB was performed produced by direct radiofluorination of a mono-iodinated triphenylsulfonium salt. Reaction parameters such as phase-transfer catalyst, amount of precursor, reaction solvent and temperature were studied. Then [^{18}F]FIB was conjugated to the alkyne-trityl-Candesartan analog using the Sonogashira cross-coupling reaction, followed by acid detritylation. Several coupling reactions and de-protection conditions were evaluated. The radiosynthesis of [^{18}F]FIB was reproducibly carried out in a ~30% yield. However, the best cross-coupling condition produced the desired [^{18}F]FB-Candesartan in low yield and MA due to partial destruction of the compound during the coupling and acid hydrolysis. Attempts to further improve the radiochemical yield or change HPLC semi-prep conditions turned out to be fruitless so far. The authors concluded that the use of Sonogashira cross-coupling reaction to produce [^{18}F]FB-Candesartan in high radiochemical yields and molar activities resulted to be challenging.

1.14 References

[1] THE NATIONAL ACADEMY OF SCIENCES. Science 1930;72:372-8.

[2] Lawrence EO and Livingston MS. The Production of High Speed Protons Without the Use of High Voltages. Physical Review 1931;38:834-.

[3] Wolf AP. Cyclotrons, radionuclides, precursors, and demands for routine versus research compounds. Ann Neurol 1984;15 Suppl:S19-24.

[4] Comar D and Crouzel C. Biomedical cyclotrons for radioisotope production. Int J Rad Appl Instrum B 1986;13:101-7.

[5] Chu WT. Cyclotron and medicine. Zeitschrift fur medizinische Physik 2006;16:109-10.

[6] Ter-Pogossian MM and Wagner HN, Jr. A new look at the cyclotron for making short-lived isotopes. 1966 -classical article. Seminars in nuclear medicine 1998;28:202-12.

[7] Friedlander G, Kennedy JW, Macias ES, and Miller JM. Nuclear and Radiochemistry: Wiley,1981.

[8] Ter-Pogossian MM. Cyclotron produced short-lived radioactive isotopes. Am J Roentgenol Radium Ther Nucl Med 1966;96:737-43.

[9] Kilbourn MR, Huizenga JR, Nuclear NRCCo, Radiochemistry, Sciences NRCBoC, Technology, *et al.* Fluorine-18 Labeling of Radiopharmaceuticals: National Academy Press,1990.

[10] Nickles RJ, Daube ME, and Ruth TJ. An 18O2 target for the production of [18F]F2. The International Journal of Applied Radiation and Isotopes 1984;35:117-22.

[11] Nickles RJ. A high-pressure gas target for cyclotrons. Nuclear Instruments and Methods 1980;177:593-4.

[12] Iwata R, Ido T, Brady F, Takahashi T, and Ujiie A. [18F]fluoride production with a circulating [18O]water target. International Journal of Radiation Applications and Instrumentation. Part A. Applied Radiation and Isotopes 1987;38:979-84.

[13] Saha GB. Fundamentals of Nuclear Pharmacy: Springer International Publishing,2017.

[14] RUTH TJ and WOLF AP. Absolute Cross Sections for the Production of 18F via the 18O(p, n)18F Reaction. 1979;26:21.

[15] Phelps ME. PET: Molecular Imaging and Its Biological Applications: Springer,2004.

[16] VanBrocklin HF and O'Neil JP. Cyclotron production of [18F]fluoride ion and [18F]fluorine gas and their medical applications. AIP Conference Proceedings 1997;392:1329-32.

[17] Guillaume M, Luxen A, Nebeling B, Argentini M, Clark JC, and Pike VW. Recommendations for fluorine-18 production. International Journal of Radiation Applications and Instrumentation. Part A. Applied Radiation and Isotopes 1991;42:749-62.

[18] Wilson JS, Avila-Rodriguez MA, Johnson RR, Zyuzin A, and McQuarrie SA. Niobium sputtered Havar foils for the high-power production of reactive [18F]fluoride by proton irradiation of [18O]H2O targets. Applied Radiation and Isotopes 2008;66:565-70.

[19] Jagoda EM, Vaquero JJ, Seidel J, Green MV, and Eckelman WC. Experiment assessment of mass effects in the rat: implications for small animal PET imaging. Nucl Med Biol 2004;31:771-9.

[20] Schlyer DJ, Bastos MAV, Alexoff D, and Wolf AP. Separation of [18F]fluoride from [18O]water using anion exchange resin. International Journal of Radiation Applications and Instrumentation. Part A. Applied Radiation and Isotopes 1990;41:531-3.

[21] Gillies JM, Najim N, and Zweit J. Analysis of metal radioisotope impurities generated in [18O]H2O during the cyclotron production of fluorine-18. Applied Radiation and Isotopes 2006;64:431-4.

[22] Tilbury RS and Dahl JR. ¹³ N Species Formed by Proton Irradiation of Water. Radiation Research 1979;79:22-33.

[23] Production of Radionuclides in Accelerators. Handbook of Radiopharmaceuticals, p. 1-70.

[24] Wadsak W and Mitterhauser M. Basics and principles of radiopharmaceuticals for PET/CT. European Journal of Radiology 2010;73:461-9.

[25] Wagner HN, Jr. and Wahl RL. Principles and practice of PET and PET/CT. 2nd ed. ed.: Philadelphia : Lippincott Williams & Wilkins,2009.

[26] Chua S and Groves A. 1 - Biomedical Positron Emission Tomography (PET) imaging. In: P Morris editor. Biomedical Imaging: Woodhead Publishing; 2014, p. 3-40.

[27] Wadsak W and Mitterhauser M. Basics and principles of radiopharmaceuticals for PET/CT. Eur J Radiol 2010;73:461-9.

[28] Dupuis J, Harel F, and Nguyen QT. Molecular imaging of the pulmonary circulation in health and disease. Clin Transl Imaging 2014;2:415-26.

[29] Crichton R, Blower P, Hider R, Nielsen P, Porter J, Ward R, *et al*. Metal Chelation in Medicine: Royal Society of Chemistry,2016.

[30] Price EW and Orvig C. Matching chelators to radiometals for radiopharmaceuticals. Chem Soc Rev 2014;43:260-90.

[31] Laverman P, McBride WJ, Sharkey RM, Goldenberg DM, and Boerman OC. Al(18) F labeling of peptides and proteins. J Labelled Comp Radiopharm 2014;57:219-23.

[32] Downs AJ. Chemistry of Aluminium, Gallium, Indium and Thallium: Springer Netherlands,1993.

[33] Hancock RD and Martell AE. Ligand design for selective complexation of metal ions in aqueous solution. Chemical Reviews 1989;89:1875-914.

[34] Bruce Martin R. Ternary complexes of Al3+ and F− with a third ligand. Coordination Chemistry Reviews 1996;149:23-32.

[35] McBride WJ, Sharkey RM, Karacay H, D'Souza CA, Rossi EA, Laverman P, *et al*. A novel method of 18F radiolabeling for PET. J Nucl Med 2009;50:991-8.

[36] Smith GE, Sladen HL, Biagini SCG, and Blower PJ. Inorganic approaches for radiolabelling biomolecules with fluorine-18 for imaging with positron emission tomography. Dalton Trans 2011;40:6196-205.

[37] Cacheris WP, Nickle SK, and Sherry AD. Thermodynamic study of lanthanide complexes of 1,4,7-triazacyclononane-N,N',N"-triacetic acid and 1,4,7,10-tetraazacyclododecane-N,N',N",N'"-tetraacetic acid. Inorganic Chemistry 1987;26:958-60.

[38] Geraldes CFGC, Brown III RD, Brucher E, Koenig SH, Sherry AD, and Spiller M. Nuclear magnetic relaxation dispersion profiles of aqueous solutions of a series of gd(nota) analogs. Magnetic Resonance in Medicine 1992;27:284-95.

[39] André JP, Mäcke H, Kaspar A, Künnecke B, Zehnder M, and Macko L. In vivo and in vitro 27Al NMR studies of aluminum(III) chelates of triazacyclononane polycarboxylate ligands. Journal of Inorganic Biochemistry 2002;88:1-6.

[40] Laverman P, D'Souza CA, Eek A, McBride WJ, Sharkey RM, Oyen WJ, *et al.* Optimized labeling of NOTA-conjugated octreotide with F-18. Tumour Biol 2012;33:427-34.

[41] D'Souza C, McBride W, Todaro L, Sharkey R, Karacay H, Rossi E, *et al.* Evaluation of 1,4,7-triazacyclononane-1,4-diacetate (NODA) ligand for the development of PET imaging agents. Journal of Nuclear Medicine 2011;52:577.

[42] De Mello WC. Renin Angiotensin System and the Heart: Wiley,2005.

[43] Sechi LA, Grady EF, Griffin CA, Kalinyak JE, and Schambelan M. Distribution of angiotensin II receptor subtypes in rat and human kidney. American Journal of Physiology-Renal Physiology 1992;262:F236-F40.

[44] Noda K, Saad Y, Kinoshita A, Boyle TP, Graham RM, Husain A, *et al*. Tetrazole and Carboxylate Groups of Angiotensin Receptor Antagonists Bind to the Same Subsite by Different Mechanisms. Journal of Biological Chemistry 1995;270:2284-9.

[45] Burnier M and Brunner HR. Angiotensin II receptor antagonists. The Lancet 2000;355:637-45.

[46] Mathews WB, Burns HD, Dannals RF, Ravert HT, and Naylor EM. Carbon-11 labeling of a potent, nonpeptide, at1-selective angiotensin-II receptor antagonist: MK-996. Journal of Labelled Compounds and Radiopharmaceuticals 1995;36:729-37.

[47] Hamill TG, Donald Burns H, Dannals RF, Mathews WB, Musachio JL, Ravert HT, *et al*. Development of [11C]L-159,884: A radiolabelled, nonpeptide angiotensin II antagonist that is useful for angiotensin II, AT1 receptor imaging. Applied Radiation and Isotopes 1996;47:211-8.

[48] Zober TG, Mathews WB, Seckin E, Yoo S-e, Hilton J, Xia J, *et al*. PET Imaging of the AT1 receptor with [11C]KR31173. Nuclear Medicine and Biology 2006;33:5-13.

[49] Verjans JWH, Lovhaug D, Narula N, Petrov AD, Indrevoll B, Bjurgert E, *et al*. Noninvasive Imaging of Angiotensin Receptors After Myocardial Infarction. JACC: Cardiovascular Imaging 2008;1:354-62.

[50] Sanad MH, Sallam KM, Marzook FA, and Abd-Elhaliem SM. Radioiodination and biological evaluation of candesartan as a tracer for cardiovascular disorder detection. Journal of Labelled Compounds and Radiopharmaceuticals 2016;59:484-91.

[51] Hoffmann M, Chen X, Hirano M, Arimitsu K, Kimura H, Higuchi T, *et al.* 18F-Labeled Derivatives of Irbesartan for Angiotensin II Receptor PET Imaging. ChemMedChem 2018;13:2546-57.

[52] Chen X, Hirano M, Werner RA, Decker M, and Higuchi T. Novel 18F-Labeled PET Imaging Agent FV45 Targeting the Renin–Angiotensin System. ACS Omega 2018;3:10460-70.

[53] Sahylí Ortega Pijeira M, Sérgio Gonçalves Nunes P, Nascimento dos Santos S, Zhang Z, Pérez Nario A, Araujo Perini E, *et al*. Synthesis and Evaluation of [18F]FEtLos and [18F]AMBF3Los as Novel 18F-Labelled Losartan Derivatives for Molecular Imaging of Angiotensin II Type 1 Receptors. Molecules 2020;25:1872.

[54] Hadizad T, Kirkpatrick SA, Mason S, Burns K, Beanlands RS, and DaSilva JN. Novel O-[11C]methylated derivatives of candesartan as angiotensin II AT1 receptor imaging ligands: Radiosynthesis and ex vivo evaluation in rats. Bioorganic & Medicinal Chemistry 2009;17:7971-7.

[55] Hadizad T, Collins J, E. Antoun R, S. Beanlands R, and N. DaSilva J. [11C]Methyl-losartan as a potential ligand for PET imaging angiotensin II AT1 receptors. Journal of Labelled Compounds and Radiopharmaceuticals 2011;54:754-7.

[56] Hachem M, Tiberi M, Ismail B, Hunter CR, Arksey N, Hadizad T, *et al*. Characterization of 18F-FPyKYNE-Losartan for Imaging AT1 Receptors. Journal of Nuclear Medicine 2016;57:1612-7.

[57] Ismail B, deKemp RA, Hadizad T, Mackasey K, Beanlands RS, and DaSilva JN. Decreased renal AT1 receptor binding in rats after subtotal nephrectomy: PET study with [18F]FPyKYNE-losartan. EJNMMI Research 2016;6:55.

[58] Ismail B, Hadizad T, Antoun R, Lortie M, deKemp RA, Beanlands RSB, *et al*. Evaluation of [11C]methyl-losartan and [11C]methyl-EXP3174 for PET imaging of renal AT1receptor in rats. Nuclear Medicine and Biology 2015;42:850-7.

[59] Fukushima K, Bravo PE, Higuchi T, Schuleri KH, Lin X, Abraham MR, *et al*. Molecular Hybrid Positron Emission Tomography/Computed Tomography Imaging of Cardiac Angiotensin II Type 1 Receptors. Journal of the American College of Cardiology 2012;60:2527-34.

[60] Kubo K, Kohara Y, Imamiya E, Sugiura Y, Inada Y, Furukawa Y, *et al*. Nonpeptide angiotensin II receptor antagonists. Synthesis and biological activity of benzimidazolecarboxylic acids. J Med Chem 1993;36:2182-95.

[61] Guengerich FP and Yoshimoto FK. Formation and Cleavage of C-C Bonds by Enzymatic Oxidation-Reduction Reactions. Chemical reviews 2018;118:6573-655.

[62] Lortie M, DaSilva JN, Kirkpatrick SA, Hadizad T, Ismail BA, Beanlands RSB, *et al*. Analysis of [11C]methyl-candesartan kinetics in the rat kidney for the assessment of angiotensin II type 1 receptor density in vivo with PET. Nuclear Medicine and Biology 2013;40:252-61.

[63] Abreu Diaz AM, Drumeva GO, Petrenyov DR, Carrier J-F, and DaSilva JN. Synthesis of the Novel AT1 Receptor Tracer [18F]Fluoropyridine–Candesartan via Click Chemistry. ACS Omega 2020.

[64] Way JD and Wuest F. Automated radiosynthesis of no-carrier-added 4-[18F]fluoroiodobenzene: a versatile building block in 18F radiochemistry. Journal of Labelled Compounds and Radiopharmaceuticals 2014;57:104-9.

[65] Way JD, Bergman C, and Wuest F. Sonogashira cross-coupling reaction with 4-[18F]fluoroiodobenzene for rapid 18F-labelling of peptides. Chem Commun (Camb) 2015;51:3838-41.

[66] Schueller MJ, Alexoff DL, and Schlyer DJ. Separating long-lived metal ions from 18F during H218O recovery. Nuclear Instruments and Methods in Physics Research Section B: Beam Interactions with Materials and Atoms 2007;261:795-9.

[67] Krasikova R. Synthesis Modules and Automation in F-18 Labeling. Berlin, Heidelberg: Springer Berlin Heidelberg; 2007, p. 289-316.

Chapter 2: SPECT/PET imaging of adrenomedullin receptors: a promising strategy for studying pulmonary vascular diseases

Luis Michel Alonso Martinez[1,2,3], François Harel[2,3,4], Myriam Létourneau[5], Vincent Finnerty[3], Alain Fournier[5], Jocelyn Dupuis[3,6], Jean N. DaSilva[*,1,2,4]

[1] University of Montreal Hospital Research Centre, 900 rue Saint-Denis, Montréal (Québec) H2X 3H8, Canada

[2] Department of Biomedical Engineering, Faculty of Medicine, Université de Montréal, Pavillon Paul-G. Desmarais, 2960 chemin de la Tour, Montréal (Québec) H3T 1J4, Canada

[3] Research Center of the Montreal Heart Institute, 5000 Rue Bélanger, Montréal (Québec) H1T 1C8, Canada

[4] Department of Radiology, Radio-oncology and Nuclear Medicine, Université de Montréal, Pavillon Roger-Gaudry, 2900 boulevard Edouard Montpetit, Montréal (Québec) H3T 1J4, Canada

[5] Laboratoire d'études moléculaires et pharmacologiques des peptides, INRS-Institut Armand-Frappier, 531 boulevard des Prairies, Laval (Québec) H7V 1B7, Canada

[6] Department of Medicine, Université de Montréal, 2900 boulevard Edouard Montpetit, Montréal (Québec) H3T 1J4, Canada

Am J Nucl Med Mol Imaging 2019;9(5):203-215 www.ajnmmi.us /ISSN:2160-8407/ajnmmi0099437.

2.1 Abstract

Circulating adrenomedullin (AM) levels are elevated in several cardiovascular diseases, including pulmonary vascular diseases causing pulmonary hypertension. To date the perfusion agent ^{99m}Tc-albumin macroaggregates (MAA) is the only approved radiopharmaceutical used for imaging of pulmonary circulation. Unlike [^{99m}Tc]Tc-MAA, imaging the AM receptors involves a molecular process dependent on the density of the receptors and the affinity of specific radioligands. The AM receptors are abundantly distributed in lung capillaries and its integrity provides protection in the development of pulmonary vascular diseases. This review summarizes the development and characterization of radioligands for *in vivo* imaging of AM receptors as an early predictor of the onset of a pulmonary vascular disease.

Keywords

Pulmonary arterial hypertension, Pulmonary embolism, SPECT, PET, Adrenomedullin radiotracers, Lung microcirculation.

2.2 Introduction

2.2.1 Adrenomedullin receptors

Adrenomedullin (AM) is a 52-amino acid peptide member of the calcitonin gene-related peptide (CGRP) family, that also includes calcitonin, two forms of calcitonin gene-related peptide (αCGRP and βCGRP), adrenomedullin-2 and amylin [1,2]. On the one hand, CGRP mediates its effects through a heteromeric receptor composed of a G protein-coupled receptor called calcitonin receptor-like receptor (CLR) and a receptor activity-modifying protein (RAMP1) (**Figure 1a**). On the other hand, AM mediates vaso- and bronchodilating actions through specific AM receptors [3,4]. Those are similarly composed by the heterodimer combination of CLR and RAMP2 or RAMP3, respectively, which leads to the formation of the AM receptor subtypes 1 and 2 (termed AM1 and AM2) [5,6] (**Figure 1b and 1c**). The CLR component of the AM receptors belongs to the B family of the seven-transmembrane G protein-coupled receptors (GPCRs) and is conserved among the AM receptor subtypes [7]. The RAMP family comprises three members (RAMP1, RAMP2 and RAMP3) that each exhibits an N-terminal portion of 100–120 amino acids, a single transmembrane central domain, and a C-terminal segment of approximately 10 residues that is essential for glycosylation, cell-surface targeting and ligand-binding selectivity of the receptor [8].

2.2.1 Expression of Adrenomedullin Receptors

Specific AM binding sites have been identified in many tissues including the heart, blood vessels, lung and spleen [9,10]. Particularly, AM receptor subtype 1 is expressed in vascular smooth muscle cells of heart, blood vessels, and spleen and its expression is markedly high in lung. Martinez *et al.*[11] extensively studied the expression of AM receptors in lung. Their findings suggest a specific distribution of AM and its receptors in the apical border of the epithelium and

in the airway smooth muscle. AM receptors are also highly expressed in the cytoplasm of the serous cells of the bronchial glands and in type II pneumocytes, the latter being involved in the regeneration of epithelial layers of the lung. Other studies have evidenced an increased level of AM1 in the kidney and heart of rats with obstructive nephropathy and congestive heart failure [12]. In addition, a reduced expression level of RAMP2 and CLR, paired with an increase of RAMP3 levels, has been found during lipopolysaccharide-induced sepsis in rats. Also, a reduced level of the AM1 receptor components was reported in pulmonary hypertension [13-16].

Previous reports from animal models suggest that circulating AM levels are up-regulated in several cardiovascular diseases, including pulmonary vascular diseases causing pulmonary hypertension. Also, an elevation of local AM concentrations in some tumor cell lines such as carcinoids (H679, UMC11) [17], adenocarcinomas (H2228) [18] and to a greater extent in tumors of epithelial origin like small cell lung carcinomas H774, H123 and H735 [19,20] was reported. Despite an association between AM and its receptor with these pathologies, the therapeutic potential of regulating the AMergic system in humans remains under-documented due to the limited information about the mechanism controlling its function [21].

2.2.2 Pulmonary Hypertension

Pulmonary hypertension (PH) is characterized by a mean pulmonary artery pressure >20 mmHg [22] and is the result of numerous disorders that may directly or indirectly affect the integrity of pulmonary circulation. As a general consensus, this disorder is difficult to diagnose, and in most cases there is a rather large time gap between the initial clinical manifestation and the diagnosis, thereby evidencing the needs of early detection strategies of pulmonary vascular diseases [10]. This delay is in part due to the non-specific symptomatology caused by pulmonary vascular diseases, shortness of breath, and to the current diagnostic gold standard that requires invasive

hemodymamic measurement of pulmonary artery pressures. Although non-invasive methods, such as cardiac ultrasound, can be utilized for screening, there is currently no biomarker for the disease, as well as no imaging method that directly assesses pulmonary vascular biology.

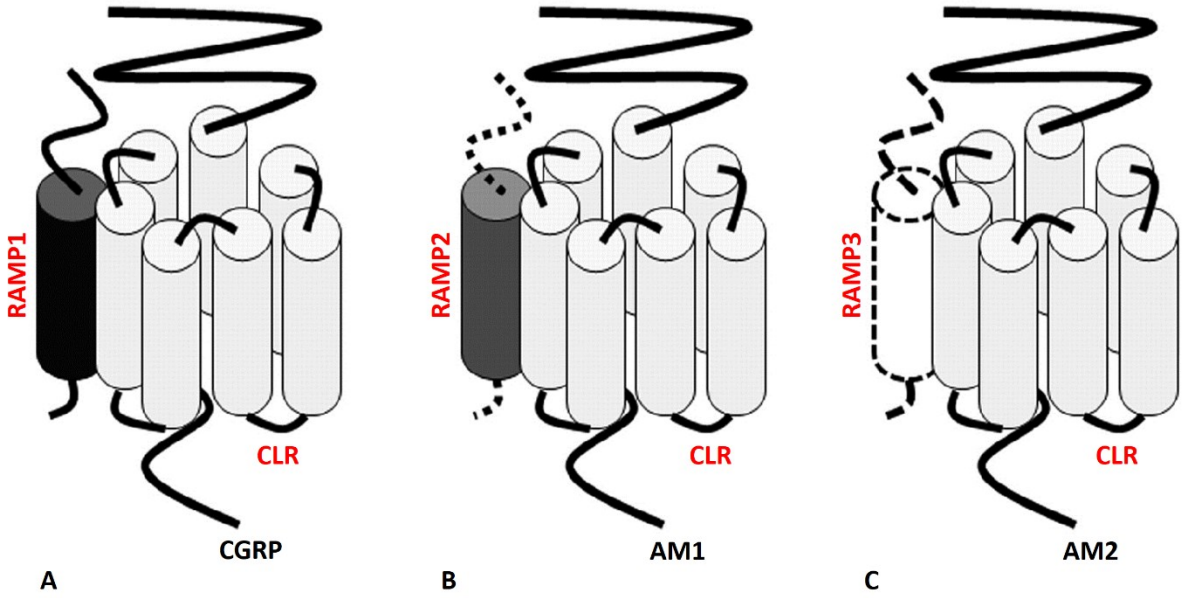

Figure 1. Composition of calcitonin gene-related peptide (CGRP) (**a**) and adrenomedullin receptor subtypes 1 (**b**) and 2 (**c**). Calcitonin-like receptor (CLR) is a seven transmembrane protein and the receptor activity-modifying protein (RAMP) is a component that varies in subtypes. Modified from Hay *et al.* [36]

The integrity of pulmonary circulation is currently anatomically imaged by X-ray, chest CT angiography, MRI and pulmonary angiography with radiologic contrast [23]. Lung perfusion scanning with ^{99m}Tc-albumin macroaggregates (MAA) is the most utilized procedure to dynamically study the pulmonary vasculature. However, [^{99m}Tc]Tc-MAA has the limitation of not allowing the investigation of the pulmonary microcirculation due to their large size, thus causing their trapping in small pulmonary vessels and preventing visualization beyond the point of

blockage [24]. Furthermore, being a physical tracer, [^{99m}Tc]Tc-MAA distribute solely according to the relative supply of blood flow and does not provide information on the biology of the pulmonary circulation.

At the microcirculation level, endothelial injury is an early event in the development of a pulmonary vascular disease [25]. In particular, this disorder is characterized by a dysregulation of transporters and specific receptors such as the AM receptors [10]. Thus, we hypothesized that a molecule targeting endothelial metabolic functions, like does AM, could serve as an imaging agent of pulmonary microcirculation.

2.3 SPECT ADRENOMEDULLIN RADIOLIGANDS

2.3.1 Initial Proof of Concept:[^{125}I]I-rAM(1-50)

Biodistribution, pharmacokinetics and multi-organ clearance of [^{125}I]I-rAM(1-50) (**Figure 2a**) were evaluated in rats. After injecting the tracer (200 µL, 18.5 kBq, 0.5 µCi), blood samples were collected 1 min post-injection and then this step was repeated every 5 min for a 30-min period. The tracer exhibited a fast distribution half-life of 2 min and an elimination of 15.9 min that was not affected by the administration of hAM(22-52), CGRP or unlabeled rAM(1-50). [^{125}I]I-rAM(1-50) was predominately retained 20 times more efficiently in the lungs than any other organs, and the uptake was found to be specific to AM receptors after blocking with unlabeled rAM(1-50). There was also no difference in plasma and tissue levels of endogenous AM demonstrating that lungs are the primary site for clearance of [^{125}I]I-rAM(1-50), mediated via a specific murine AM receptor process at the vascular endothelium level [26].

Single-pass measurement of AM clearance was performed in dogs using the single bolus indicator-dilution technique. A bolus of 122 kBq (3.3 µCi) was injected, and the samples were collected and processed to construct the indicator-dilution curves. After a baseline single bolus dilution, AM(22-52), CGRP or unlabeled rAM(1-50) was administered to perform a second indicator-dilution experiment [26]. The findings suggested an important first-pass extraction of [^{125}I]I-rAM(1-50) that was greatly reduced after injection of unlabeled rAM(1-50), slightly decreased after AM(22-52), and unaffected by CGRP, revealing a specific binding to AM receptors. Altogether, these experiments indicated that there is an important first-pass pulmonary clearance in the lung and that [^{125}I]I-rAM(1-50) binds with a very high affinity to its receptor.

2.3.2 ^{99m}Tc-labeled DTPA-AM

2.3.2.1 Synthesis

Disulfide bridged DTPA-human AM(1-52) is identical to native human AM, except for the addition of DTPA as a ^{99m}Tc chelator at the N-terminus (**Figure 2b**) [24]. Using DTPA dianhydride, the chelating moiety was incorporated into the peptide chain and purified by reverse-phase HPLC (RP-HPLC). The conjugate was radiolabeled with ^{99m}Tc in presence of $SnCl_2$ in acidic media, at room temperature for 1h, and then purified by RP-HPLC. The radiochemical purity was 93±2%.

2.3.2.2 In Vitro Evaluation

Tracer affinity was evaluated in human breast adenocarcinoma MCF-7 cells by competitive-binding experiment with [^{125}I]I-hAM(1-52). The IC_{50} value of DTPA-AM was calculated as 19 nM, which is within the expected range for a specific AM ligand [24].

2.3.2.3 In Vivo Evaluation

Plasma kinetics and biodistribution of [^{99m}Tc]Tc-DTPA-AM (18.5 µg, 185 MBq, 5 mCi) were studied in healthy dogs. Plasma levels rapidly decreased following a bi-compartmental model with a distribution half-life of less than 2 min and an elimination half-life of 42 min. In addition, the rate constant between the central and peripheral compartments was established at 24, thereby showing an important distribution into the peripheral compartment [24].

Biodistribution and multi-organ clearance were evaluated by dynamic planar and static SPECT imaging. Dynamic acquisitions of the lungs, heart, liver, and kidneys were recorded for 30 min, while static acquisitions were also recorded for whole individual organs (lungs, kidneys, liver, heart, bladder, and gallbladder) at 30, 60, and 120 min after the initial injection. The result demonstrated that the lungs predominantly retained the peptide with 27±1% of the injected dose (ID) at 30 min post-injection. The kidneys and liver also exhibited important uptakes with 19±1% ID and 12±1% ID, respectively. Tracer retained in the lung was slowly washed out over time maintaining approximately 20% of the injected dose after 120 min [24]. Hence, cyclic [^{99m}Tc]Tc-DTPA-AM derivative exhibited significant lung uptake but important retention in liver and heart were found to potentially decrease its interest as a SPECT imaging agent.

2.3.3 ^{99m}Tc-labeled-AM Through the Free Cys^{16,21} -SH Functions ((S-[^{99m}Tc]Tc-S)-AM)

2.3.3.1 Synthesis

The linear AM derivative (L-AM), containing free SH groups on cysteines 16 and 21, was directly radiolabeled with technetium via chelation of oxotechnetium (V) with the cysteine residues, using $SnCl_2$ as a reducing agent (**Figure 2c**). Similar to the parent molecule DTPA-AM,

the radiolabeling was performed in acidic media for 1 h. Moreover, a study with different linear AM fragments i.e. AM(13-52) and serial AM fragments ranging from 16-52 to 22-52 showed that only the peptides containing both cysteine residues were able to chelate [^{99m}Tc]Tc(V)O^{2+}. The labeling efficiency for linear free SH AM was 55% but with an unexpected high 35% of radiocolloids. After purification by C_{18} Sep-Pak, (S-[^{99m}Tc]Tc-S)-AM was produced with a radiochemical purity ≥95%. The average specific activity was 51.8±15 MBq/nmol (1.4±0.4 mCi/nmol) [24].

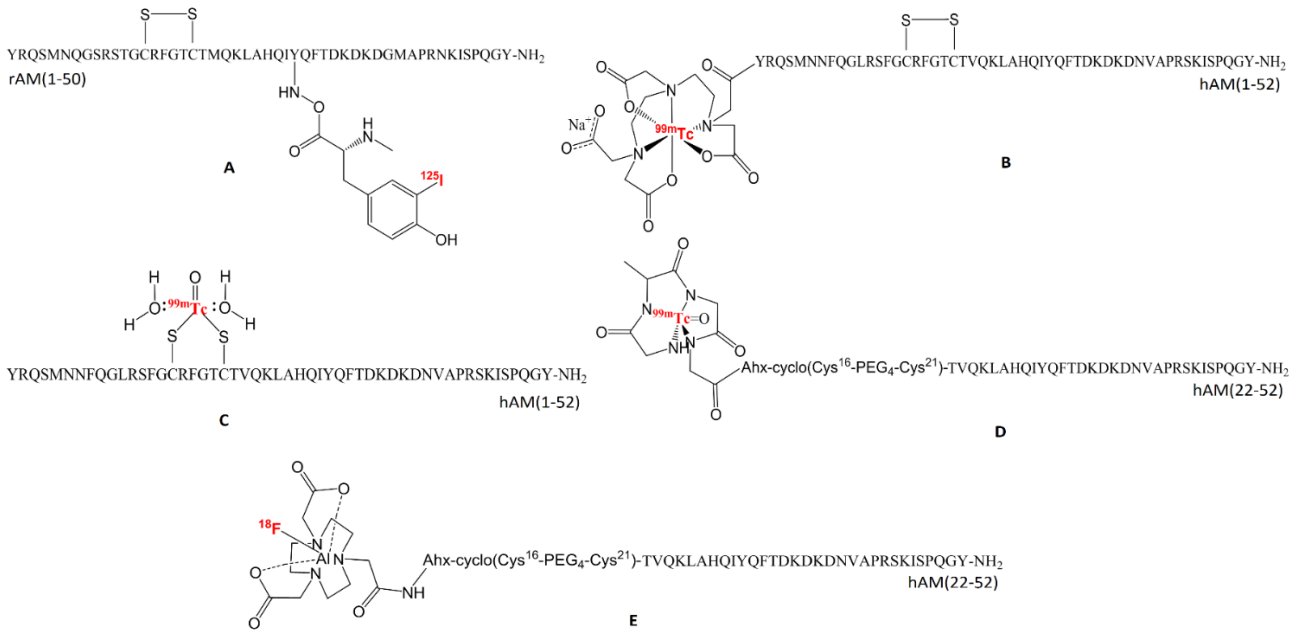

Figure 2. Adrenomedullin SPECT and PET radiotracers. Proof of concept: [^{125}I]I-rAM(1-50) (**a**), [^{99m}Tc]Tc-DTPA-AM (**b**), [^{99m}Tc]Tc-Cys^{16,21}-AM (**c**), [^{99m}Tc]Tc-PulmoBind (**d**), and [^{18}F]AlF-DFH17 (**e**).

2.3.3.2 In Vitro Evaluation

Similar to that of DTPA-AM, the L-AM affinity was evaluated in human breast adenocarcinoma MCF-7 cells by competitive-binding experiment with [^{125}I]I-hAM(1-52). The IC_{50} value was 70 nM confirming the competitive binding of the L-AM form in human cells expressing the AM receptors. Dog lung homogenates were also used to study the affinity and selectivity of L-AM, along with other agonists and antagonists of the calcitonin peptide family, by receptor-binding assays using [^{125}I]I-hAM(1-52). Although it was weaker than the native molecule, the linear peptide exhibited excellent affinity and selectivity for canine AM receptor subtype 1 over those of other peptides like adrenomedullin-2 (AM2), amylin and pro-adrenomedullin N-terminal peptide [27].

2.3.3.3 In Vivo Evaluation

Plasma kinetics and biodistribution of the (S-[^{99m}Tc]Tc-S)-AM derivative were studied in healthy dogs. The pharmacokinetic two-compartment model resulted in a distribution half-life of 1.7 min and an elimination half-life of 32 min, thus evidencing a slightly faster elimination than [^{99m}Tc]Tc-DTPA-AM. Transpulmonary indicator dilution with Evans blue dye-labeled albumin was used to precisely quantify the first-pass clearance of (S-[^{99m}Tc]Tc-S)-AM. The tracer single-pass pulmonary extraction was 30±5% being almost the same as that of [^{125}I]I-rAM. Hence, as previously demonstrated with [^{125}I]I-rAM, lungs are the primary site for clearance of (S-[^{99m}Tc]Tc-S)-AM mediated via AM receptors. Biodistribution and multiorgan clearance were evaluated by dynamic and static SPECT imaging as described for the cyclic [^{99m}Tc]Tc-DTPA-AM derivative. Unexpectedly, the (S-[^{99m}Tc]Tc-S)-AM peptide had a higher uptake in the lungs than the cyclic derivative (42±5% vs 27±1%). Also, a lower uptake in the liver and higher levels of urinary elimination were found with the tracer derived from linear AM, making this derivative an attractive

imaging agent. Moreover, a study using (S-[^{99m}Tc]Tc-S)-AM in dogs, following a surgical ligation of the pulmonary arteries, demonstrated that this radioligand could be used to visualize lung perfusion defects because anatomic perfusion mimicking large pulmonary embolism was easily detectable [27].

Finally, evaluation of (S-[^{99m}Tc]Tc-S)-AM in the rat monocrotaline-induced PH model, a paradigm that mimics group 1 pulmonary arterial hypertension (PAH), resulted in lower pulmonary uptake in the animals. This treatment causes progressive obliteration of pulmonary vessels that is associated with a reduced lung expression of RAMP2, the specific heterodimeric component of the AM1 receptor [15]. This finding was the first evidence of a direct correlation between the 80% decrease of RAMP2 protein expression, as measured by Western blot, and the approximate 70% reduction in lung uptake found during the SPECT imaging experiment. Taking all this into account, the authors concluded that the novel imaging agent could potentially diagnose PAH and other similar disorders.

2.3.4 [^{99m}Tc]Tc-PulmoBind

2.3.4.1 Structure-Activity Relationship (SAR) Studies

SAR studies were performed to characterize the structural requirements of human AM for binding sites in dog lungs. The AM derivatives (fragments 13-52, 22-52, 26-52, 1-25, 40-52 and 1-40) were produced by Fmoc solid-phase peptide synthesis and characterized *in vitro* by displacement of [^{125}I]I-hAM(1-52) [28]. First, the study demonstrated that deletion of 12 or 21 N-terminal residues, to generate fragments AM(13–52) and AM(22–52), induced a significant decrease in binding affinity, whereas deletion of four extra amino acids (AM(26–52)), led to a compound unable to bind the AM receptors present in the lung. Second, the C-terminal fragment

AM(40–52) produced no displacement while C-terminal deletions (fragments 1-25 and 1-40) induced dramatic losses of binding properties [27]. All these results suggested that the C-terminal portion of the peptide, in which is localized an α-helix structure, is essential for binding to AM receptors. Moreover, the study showed that a disruption of the disulfide bridge involving the cysteine residues 16 and 21 also reduced receptor affinity, demonstrating an important role for the disulfide bond, probably by stabilizing the secondary structure of the peptide. Finally, the order of potency for binding inhibition was AM>>linear AM (1-52)>AM(13-52)>AM(22-52)>AM(26-52)>AM(1-25), AM(40-52) and AM(1-40) [29].

2.3.4.2 Synthesis

Considering the SAR studies and the data obtained with (S-[^{99m}Tc]Tc-S)-AM, the fragments 13-52 and 22-52 were further investigated as potential AM-based lung molecular imaging agents. The AM derivatives were synthesized in high purity (≥92%) by solid-phase and radiolabeled with ^{99m}Tc, as previously described.[24],[27] Particularly, three compounds based on AM(22-52) were modified with a 4 unit-PEG spacer, aimed at substituting the intracyclic amino acid residues promoting the AM vasodilating action, and a Gly-Gly-D-Ala-Gly N_4-type chelator. Among these AM derivatives, the disulfide bridged fragment Gly-Gly-D-Ala-Gly-Cys^{16}-$(PEG)_4$-Cys^{21}-hAM(22–52) called PulmoBind was synthesized with 97% chemical purity (**Figure 2d**). PulmoBind and the other analogues were radiolabeled with Sn^{2+}-reduced technetium-99m, in a buffered solution (pH 4.5) at room temperature for 15 min. Labeling efficiencies were determined by iTLC-SG. The tracers were purified via a C_{18} Sep-Pak and reformulated in PBS pH 7.4. As expected, the ^{99m}Tc direct labeling of AM derivatives resulted in lower radiochemical yields (65%) compared to chelator-modified AM derivatives (≥80%). Among all compounds, [^{99m}Tc]Tc-PulmoBind exhibited the greatest capacity to stably complex ^{99m}Tc [29].

2.3.4.3 In Vitro Evaluation

The binding ability of PulmoBind was evaluated in dog lung homogenates by saturation and competitive displacement experiments with [^{125}I]I-hAM(1-52). Saturation studies demonstrated that [^{99m}Tc]Tc-PulmoBind was bound to specific binding sites with a density of 2,317±320 fmol/mg and affinity of Kd 2.6±0.8 nM. In contrast, (S-[^{99m}Tc]Tc-S)-AM resulted in a receptor density of 1,222±148 fmol/mg and a Kd of 0.17±0.07 nM suggesting that PulmoBind could occupy more binding sites than AM but with lower affinity. Surprisingly, [^{125}I]I-hAM(1-52) and PulmoBind displacement curves were statistically indistinguishable, suggesting that AM and PulmoBind competed for the same binding site in dog lungs [30].

2.3.4.4 In Vivo Evaluation

[^{99m}Tc]Tc-PulmoBind as well as other AM derivatives were evaluated in mongrel dogs (**Figure 3b**). The radioligands (185 MBq, 5 mCi) were injected intravenously via the jugular vein and whole-body biodistribution was evaluated by a dual head gamma-camera (Siemens) equipped with a low-energy parallel-hole collimator. Dynamic acquisitions were recorded for a 30-min period, and static whole-body scans were obtained at 30, 60, and 120 min at a scan speed of 10 cm/min. Among all derivatives, at the first min post-injection, [^{99m}Tc]Tc-Pulmobind had a lung first pass comparable to AM (~75% ID), which was then reduced to 40% in an uptake plateau that was maintained up to 1 h. At later points, uptake in kidneys and bladder was higher than in other tissues with concomitant decreases in lung, heart, and liver, indicating that PulmoBind was eliminated mainly through renal excretion [29].

Additionally, since native AM is primarily a vasodilator with hypotensive effects, the hemodynamic effect of PulmoBind and other AM analogues were evaluated in dogs by means of

pulmonary artery pressure monitoring with a Swan-Ganz catheter. After cumulative intravenous injections, native human AM clearly dropped the mean arterial blood pressure (MAP), an activity that was accompanied with an elevation in heart rate. In contrast, PulmoBind did not produce significant variations in MAP and heart rate up to a dose close to 100X the estimated lung scan dose. In addition, PulmoBind injection did not cause any significant hemodynamic effects at 300X the estimated lung scan dose in rats.

These results demonstrated that the 17 to 20 segment of AM (Arg^{17}-Phe^{18}-Gly^{19}-Thr^{20}) plays a crucial role in the vasodilating effect of this peptide and that receptor affinity is mostly associated with the C-terminal portion of the molecule. Hence, the substitution of the intracyclic amino acids with a PEG_4 spacer was an efficacious strategy to maintain a good affinity while reducing potently the hypotensive effects. Moreover, the conservation of the cyclic structure by keeping the disulfide bridged cysteine residues at position 16 and 21 is also a key feature of the ligand, as shown with the mixed results obtained with the linear analogue in which the Cys side chains were capped with acetamidomethyl (Acm) groups, in order to maintain the peptide linearity. Accordingly, the cyclic Cys^{16}-PEG_4-Cys^{21} structure, mimicking in size and constraint the cyclic core shaped in AM by the Cys^{16}- Arg^{17}-Phe^{18}-Gly^{19}-Thr^{20}-Cys^{21} segment, appears to stabilize the molecular geometry of the C-terminal stretch of the peptide and favors binding by facilitating its interaction with the AM1 receptor.

[^{99m}Tc]Tc-PulmoBind was further evaluated in the monocrotaline-induced PAH model, as previously described above. Rats were anesthetized for hemodynamic measurements and SPECT scans. *In vivo* biodistribution revealed a markedly reduced lung uptake of PulmoBind, from 12±2% ID in control rats to 4±1%, in rats with pulmonary arterial hypertension [29]. This result clearly demonstrated that [^{99m}Tc]Tc-PulmoBind was able to detect lung microcirculatory perfusion defects associated with PAH, without causing any adverse hemodynamic responses.

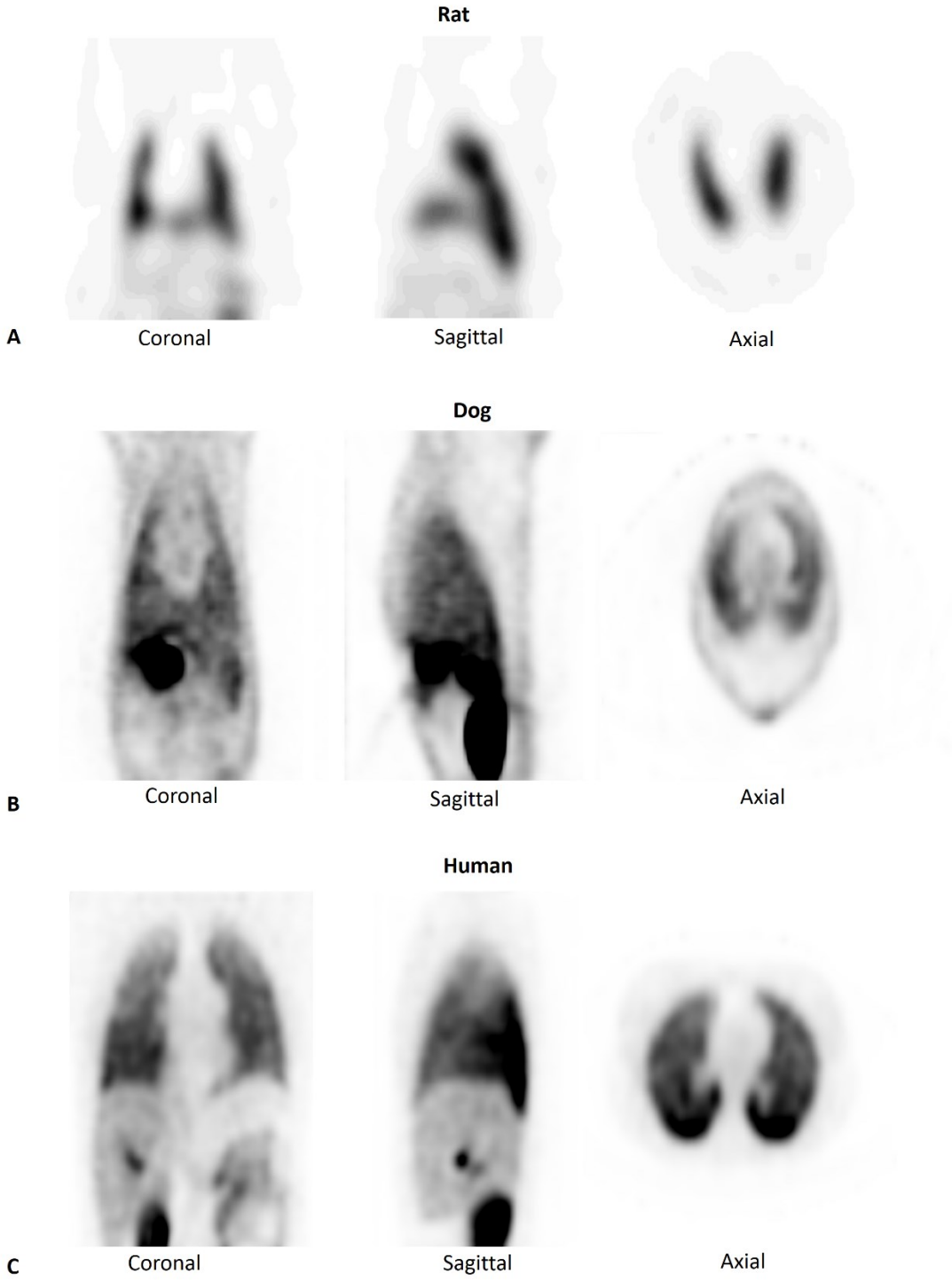

Figure 3. Whole body images of [^{99m}Tc]Tc-PulmoBind activity (30-75 min post-injection) of in Sprague-Dawley rat (**a**), mongrel dog (**b**), and human (**c**).

2.3.4.5 Human Studies

The safety, efficacy and dosing of PulmoBind was evaluated in a clinical trial phase I (NCT01539889) for molecular imaging of pulmonary circulation (**Figure 3c**) [31]. Healthy individuals (n=20) were included into dose-scaling groups of [^{99m}Tc]Tc-PulmoBind: 185 MBq (5 mCi, n=5), 370 MBq (10 mCi, n=5), or 555 MBq (15 mCi, n=10). Specific activity was estimated to be around 252 MBq/mmol (6.8 mCi/mmol). Afterward, SPECT imaging and dosimetry were serially performed. The study revealed no safety concerns at the three dosages studied. Image analysis displayed a predominant and prolonged tracer uptake in lung with a mean peak extraction of 58±7%. [^{99m}Tc]Tc-PulmoBind was generally well tolerated, with no clinically-significant adverse event related to the product since no changes in systolic and diastolic pressure, respiratory rate, oxygen saturation and body temperature were detected. At the highest dose 555 MBq (15 mCi) the tracer provided excellent images with favorable dosimetry (effective dose of approximately 6 to 8 mSv). At a dose of 555 MBq, nuclear medicine specialists judged the quality of imaging obtained with PulmoBind as superior to that attained with MAA. The study concluded that [^{99m}Tc]Tc-PulmoBind is safe and provides good quality lung perfusion imaging [31], and that the dose of 555 MBq can be used for further developments.

Subsequently, the safety of [^{99m}Tc]Tc-PulmoBind and its capacity to detect pulmonary vascular diseases associated with PH was evaluated in a human phase II study (NCT02216279) [30]. Thirty patients with PAH (group I PH, n=23) or chronic thromboembolic PH (CTEPH, group IV PH, n=7) with WHO functional class II (n=26) or III (n=4) were compared to 15 healthy subjects (control group). [^{99m}Tc]Tc-PulmoBind was administered at the previously established dose of 555 MBq (340±42 MBq/nmol, 9.18±1.14 mCi/nmol,) and SPECT/CT images were acquired in supine position after 35 min. Dynamic planar images were obtained for the first 35 min and static images after 60 min. Qualitative and semi-quantitative analyses of lung uptake were performed and the

analysis found a markedly abnormal pattern in the PH group. In fact, approximately 50% of subjects presented abnormalities ranging from moderate to severe in heterogeneity and extent. The abnormalities were unevenly distributed between the right and left lungs as well as within each lung. Compared to controls, segmental defects compatible with pulmonary embolism were present in 7 out of 7 subjects with CTEPH and in 2 out of 23 subjects with PAH. Additionally, [^{99m}Tc]Tc-PulmoBind activity distribution index was elevated by 59% in PAH compared to controls, evidencing the degree of severity of PAH group.[^{99m}Tc]Tc-PulmoBind lung SPECT was completely normal for the only individual included in the study with vasodilator-responsive idiopathic PAH, a rare form of group I PH with excellent prognosis and responsive to therapy. Repeated testing in healthy controls after one month was well tolerated and showed no significant variability of [^{99m}Tc]Tc-PulmoBind distribution. Taking all this into account, [^{99m}Tc]Tc-PulmoBind SPECT imaging of the pulmonary vascular endothelium was found to be safe in PH and showed potential to detect both pulmonary embolism and abnormalities indicative of PAH. To this extent, a PulmoBind Phase III study is now required to directly compare with other perfusion agents such as labeled macro-aggregates of albumin and angio-CT, and determine its capacity to detect pulmonary vascular diseases at earlier stages than is currently clinically available.

2.4 PET ADRENOMEDULLIN RADIOLIGANDS

A radiofluorinated AM derivative was recently developed for PET imaging of pulmonary microcirculation offering key advantages such as higher resolution images and more sensitive uptake, facilitating the quantification of AM receptors with potentially less false positives.

2.4.1[^{18}F]AlF-DFH17

2.4.1.1 Synthesis

Based on PulmoBind, the human AM derivative DFH17 (**Figure 2e**) was produced by Fmoc solid-phase peptide synthesis using the same pegylated core Cys^{16}-$(PEG)_4$-Cys^{21} [32]. The pegylated peptide was then coupled to an aminohexanoyl spacer and derivatized with the macrocyclic chelator NOTA for radiometal complexation chemistry. DFH17 was produced in 94% chemical purity and was radiofluorinated using the $Al^{18}F$ method [33]. Complexation studies with maleimido-NOTA were initially performed to find the optimal reaction conditions. Then, DFH17 was successfully radiolabeled with $Al^{18}F$ at a 22-38% (n=6) radiochemical yield and with a 99% radiochemical purity [32].

2.4.1.2 In Vivo Evaluation

[^{18}F]AlF-DFH17 was in *vivo* evaluated in Sprague-Dawley rats, mongrel dogs and rhesus monkeys (**Figure 4**). CT images and Dynamic PET were acquired on a PET-CT clinical imaging system (Siemens Biograph mCT Flow 40, Germany). Rats were injected with [^{18}F]AlF-DFH17 (~74 MBq, 2 mCi, 0.3 mL) and whole-body PET images were acquired (6 x 10 min frames), 15 min after radiopharmaceutical injection [32]. A mongrel dog was injected intravenously with 296 MBq (8 mCi, 8 mL) via the jugular vein through a 3-way stopcock 18-French catheter for lung uptake evaluation. Whole-body PET images were acquired (6 x 10 min frames), 15 min after radiopharmaceutical injection. Dynamic PET image centered on the lungs were acquired over a period of 15 minutes and then 8 whole-body PET images were obtained up to 90 min after radiopharmaceutical injection.

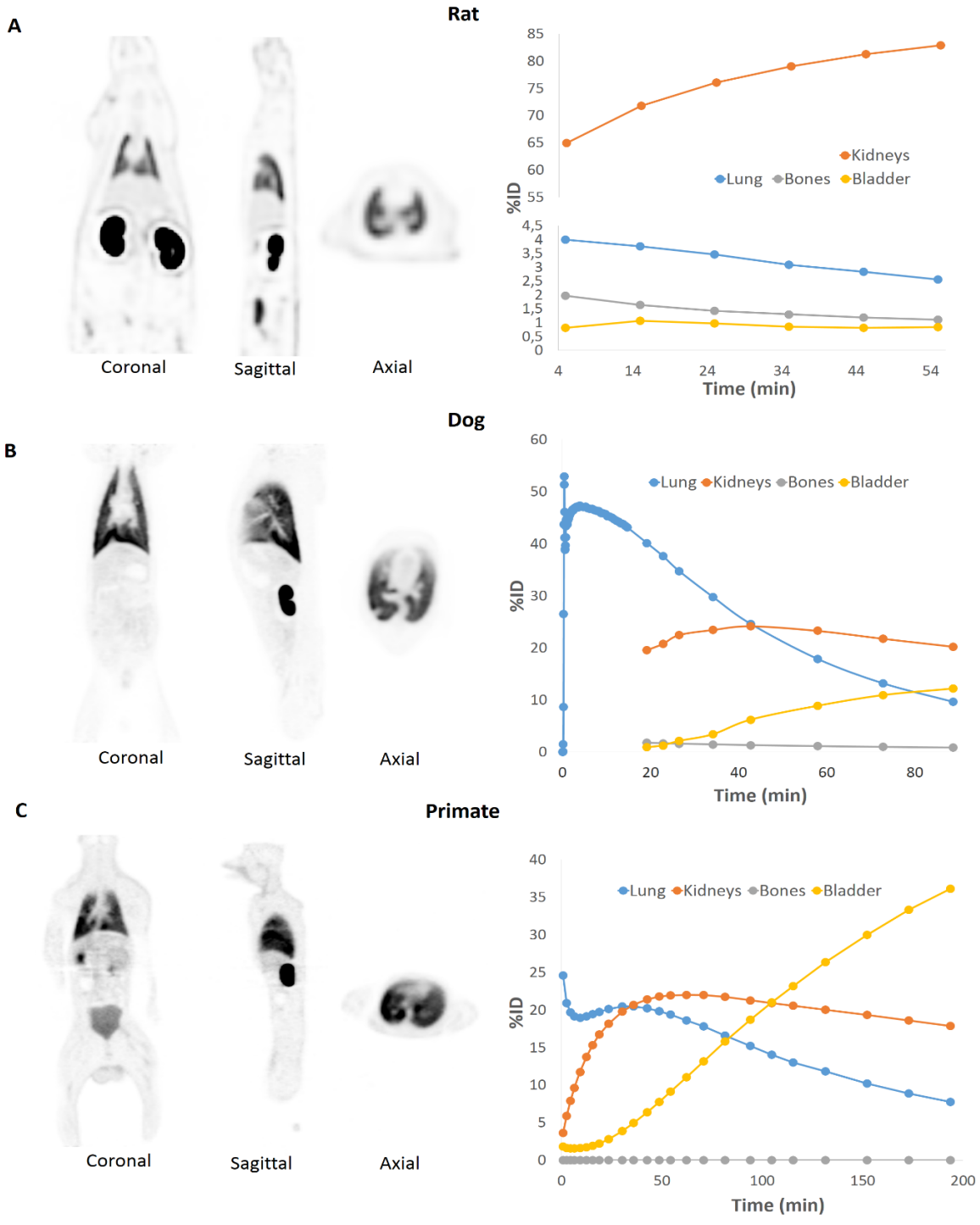

Figure 4. Whole body images of tracer activity (30-40 min post-injection, left panels) and time-activity curves (TAC, right panels) of [^{18}F]AlF-DFH17 in Sprague-Dawley rat (**a**), mongrel dog (**b**), and rhesus monkey (**c**).

A non-human primate whole-body PET imaging was performed delineating the liver, kidneys, testes, lung, and a gut region as regions of interest. Dosimetry estimations were obtained with the OLINDA-Organ Level Internal Dose Assessment software package. A conservative bladder voiding time of 4.8 h was assumed to obtain the estimates.

Compared to the control animal, high tracer accumulation was observed in rat lungs 5 min post-injection and persisted for 1 h (3% ID). The tracer was rapidly excreted by the kidneys and biodistribution in other non-target organs were considerably low (**Figure 4a**). The tracer also exhibited high in vivo stability since no radioactivity was observed in the bones even at 1 h post injection. A similar profile was found in the dog and primate with a rapid [^{18}F]AlF-DFH17 accumulation in lungs after 5 min post-injection (**Figure 4b**) and that remained up to 200 min (rhesus monkey) with a clear elimination pathway via the urinary system (**Figure 4c**). Particularly in the monkey, the uptake in the right lung was greater than the left lung presumably due to differences in perfusion between the two lungs. Signs of *in vivo* stability were found in all species since uptake in the bones due to de-fluorination of [^{18}F]AlF-DFH17 was not observed (**Figure 4**).

Time-activity curves (**Figure 4**) display that lung uptake is species-dependent with an increasing uptake of [^{18}F]AlF-DFH17 from rat to monkey. Analysis of the human and mouse transcriptomes revealed that the RAMP2 component of AM1 was relatively equally distributed among most tissues with high expression levels in lung.[34] As previously reported, modifications in RAMP2 implies an uptake reduction of AM in lung.[15] Hence, using bioinformatics tools, the alignment of AM receptor sequences of various species was carried out and the data showed differences in the RAMP2 subcomponent of the receptor. As a matter of fact, only small differences in CLR sequences (primary sequence identity of 91% vs 99%) are observed, whereas high disparities are displayed when comparing RAMP2 of rat and primate (68% vs 94%).

Therefore, it is believed that this large inter-species variation found in RAMP2 would be responsible for the contrasting inter-species uptake detected by PET imaging.

Calculations of absorbed radiation doses in the monkey identified the urinary bladder wall as the critical organ with an average absorbed radiation dose of 0.92 mSv/MBq. Based on the CFR 21 361.1 [35] recommendations, a maximum of 54 MBq of [^{18}F]AlF-DFH17 can be administered in a single dose. In addition, the effective dose (ED) in an adult male was estimated to be 66.5 μSv/MBq (ED for F18-fluorodeoxyglucose (FDG) is ~19 μSv/MBq). Taking this value into account, a maximum of 150 MBq of [^{18}F]AlF-DFH-17 can be administered within one year.

In summary, using PET imaging of AM receptors, the in vivo evaluation of [^{18}F]AlF-DFH17 has found inter-species differences in lung uptake. These dissimilarities are attributed to differences in the RAMP2 subcomponent sequences of the AM receptor subtype 1. Considering high lung uptake, *in vivo* stability and favorable dosimetry observed in monkey, the novel AM derivative [^{18}F]AlF-DFH17 exhibits an excellent potential as a PET tracer of human AM receptors.

2.5 Future perspectives

As discussed, the use of several radiotracers has proven to be a promising strategy for studying pulmonary vascular diseases via SPECT and PET imaging.

DTPA-conjugated AM opened the doors to applications of AM derivatives to image the integrity of pulmonary microcirculation. Using the well-established DTPA coordination chemistry with ^{99m}Tc, the compound was radiolabeled with more than 80% complexation yield with lower amounts of radiocolloids. This radiopharmaceutical exhibited high accumulation in the lungs with

an important kidney elimination, but unfortunately its potential use was limited due to high accumulation in non-target organs such as liver and heart. The ^{99m}Tc direct labeling with a linear form of AM was then evaluated. [^{99m}Tc]Tc-Cys^{16,21}-AM was shown to bind to lung AM receptors with high affinity allowing detection of lung perfusion defects at microcirculation level. In contrast, the real applicability of this tracer was limited due to its low radiochemical yield and higher amount of radiocolloids making its synthesis process costly and inefficient (**Table 1**).

After extensive SAR studies, the tracer [^{99m}Tc]Tc-Pulmobind was designed to overcome the problems found in the past with [^{99m}Tc]Tc-DTPA-AM and [^{99m}Tc]Tc-Cys^{16,21}-AM. The compound was robustly produced in high radiochemical yield and purity using the technetium-99m one-step lyophilized kit-like approach. From animal studies to the most recent clinical trials, [^{99m}Tc]Tc-PulmoBind exhibited high target to background signal and favorable dosimetry without any serious side effect (**Table 1**). The novel tracer, [^{18}F]AlF-DFH17, displaying high sensitivity and good spatial resolution with PET imaging was developed and evaluated in different species. Even though the complexation yield to produce [^{18}F]AlF-DFH17 was modest, our purification approach produced this tracer in high purity allowing lung imaging in animals using PET.

[^{99m}Tc]Tc-PulmoBind is thus an alternative to [^{99m}Tc]Tc-MAA for SPECT imaging of PH. Similarly, [^{18}F]AlF-DFH17 has a great potential for studying PH with PET imaging. We believe that these two tracers will contribute to the understanding of PH related to early endothelium injury and AM receptors and, thus help to better guide PH therapy.

2.6 Conclusions

Evidences of the association between AM receptors and the development of pulmonary vascular diseases was presented along this review. In conditions leading to PH, assessment of

pulmonary vascular diseases through *in vivo* quantification of AM receptors shows the capacity of evaluating endothelial injuries as an early predictor of disease and a marker of severity. Several AM tracers have been characterized for SPECT/PET imaging of pulmonary circulation. [^{99m}Tc]Tc-PulmoBind and [^{18}F]AlF-DFH17 exhibited binding selectivity to lung AM receptors, high target-to-background ratios and a favorable dosimetry. Therefore, these radiopharmaceuticals are promising agents for future applications in molecular SPECT and PET imaging of pulmonary vascular diseases.

Table 1. Radiotracers for Molecular imaging of AM receptors

Modality	*Radioligand*	*Advantages*	*Disadvantages*
SPECT	[^{99m}Tc]Tc-DTPA-AM	Rapid accumulation in lungs and renal elimination	Important retention in liver and heart
	[^{99m}Tc]Tc-Cys^{16,21}-AM	High specific binding in lungs Visualization of lung perfusion defects	Low radiochemical yield, high level of radiocolloids
	[^{99m}Tc]Tc-PulmoBind	High radiochemical yield and purity High target to background, favorable dosimetry Absence of hypotensive and hemodynamic effects	Attenuation-associated accuracy limit

PET	[^{18}F]AlF-DFH17	High sensitivity, good resolution. Possible quantification of AM receptors	Lower Complexation yield

2.7 References

[1] Hinson JP, Kapas S and Smith DM. Adrenomedullin, a multifunctional regulatory peptide. Endocr Rev 2000; 21: 138-167.

[2] Smith DM, Coppock HA, Withers DJ, Owji AA, Hay DL, Choksi TP, Chakravarty P, Legon S and Poyner DR. Adrenomedullin: receptor and signal transduction. Biochem Soc Trans 2002; 30: 432-437.

[3] Vachiery JL and Gaine S. Challenges in the diagnosis and treatment of pulmonary arterial hypertension. Eur Respir Rev 2012; 21: 313-320.

[4] Nuki C, Kawasaki H, Kitamura K, Takenaga M, Kangawa K, Eto T and Wada A. Vasodilator effect of adrenomedullin and calcitonin gene-related peptide receptors in rat mesenteric vascular beds. Biochem Biophys Res Commun 1993; 196: 245-251.

[5] Hay DL and Pioszak AA. Receptor Activity-Modifying Proteins (RAMPs): New Insights and Roles. Annu Rev Pharmacol Toxicol 2016; 56: 469-487.

[6] Hay DL, Garelja ML, Poyner DR and Walker CS. Update on the pharmacology of calcitonin/CGRP family of peptides: IUPHAR Review 25. Br J Pharmacol 2018; 175: 3-17.

[7] Conner AC, Simms J, Hay DL, Mahmoud K, Howitt SG, Wheatley M and Poyner DR. Heterodimers and family-B GPCRs: RAMPs, CGRP and adrenomedullin. Biochem Soc Trans 2004; 32: 843-846.

[8] Hagner S, Stahl U, Knoblauch B, McGregor GP and Lang RE. Calcitonin receptor-like receptor: identification and distribution in human peripheral tissues. Cell Tissue Res 2002; 310: 41-50.

[9] Yanagawa B and Nagaya N. Adrenomedullin: molecular mechanisms and its role in cardiac disease. Amino Acids 2007; 32: 157-164.

[10] Dupuis J, Harel F and Nguyen QT. Molecular imaging of the pulmonary circulation in health and disease. Clin Transl Imaging 2014; 2: 415-426.

[11] Martinez A, Miller MJ, Unsworth EJ, Siegfried JM and Cuttitta F. Expression of adrenomedullin in normal human lung and in pulmonary tumors. Endocrinology 1995; 136: 4099-4105.

[12] Muff R, Born W and Fischer JA. Calcitonin, calcitonin gene-related peptide, adrenomedullin and amylin: homologous peptides, separate receptors and overlapping biological actions. Eur J Endocrinol 1995; 133: 17-20.

[13] Nikitenko LL, Blucher N, Fox SB, Bicknell R, Smith DM and Rees MC. Adrenomedullin and CGRP interact with endogenous calcitonin-receptor-like receptor in endothelial cells and induce its desensitisation by different mechanisms. J Cell Sci 2006; 119: 910-922.

[14] Nowak W, Parameswaran N, Hall CS, Aiyar N, Sparks HV and Spielman WS. Novel regulation of adrenomedullin receptor by PDGF: role of receptor activity modifying protein-3. Am J Physiol Cell Physiol 2002; 282: C1322-1331.

[15] Dupuis J, Harel F, Fu Y, Nguyen QT, Letourneau M, Prefontaine A and Fournier A. Molecular imaging of monocrotaline-induced pulmonary vascular disease with radiolabeled linear adrenomedullin. J Nucl Med 2009; 50: 1110-1115.

[16] Merabet N, Nsaibia MJ, Nguyen QT, Shi YF, Letourneau M, Fournier A, Tardif JC, Harel F and Dupuis J. PulmoBind Imaging Measures Reduction of Vascular Adrenomedullin Receptor Activity with Lack of effect of Sildenafil in Pulmonary Hypertension. Sci Rep 2019; 9: 6609.

[17] Sugo S, Minamino N, Shoji H, Kangawa K, Kitamura K, Eto T and Matsuo H. Production and secretion of adrenomedullin from vascular smooth muscle cells: augmented production by tumor necrosis factor-alpha. Biochem Biophys Res Commun 1994; 203: 719-726.

[18] Born W, Muff R and Fischer JA. Functional interaction of G protein-coupled receptors of the adrenomedullin peptide family with accessory receptor-activity-modifying proteins (RAMP). Microsc Res Tech 2002; 57: 14-22.

[19] Cuttitta F, Fedorko J, Gu JA, Lebacq-Verheyden AM, Linnoila RI and Battey JF. Gastrin-releasing peptide gene-associated peptides are expressed in normal human fetal lung and small cell lung cancer: a novel peptide family found in man. J Clin Endocrinol Metab 1988; 67: 576-583.

[20] Martinez A, Elsasser TH, Muro-Cacho C, Moody TW, Miller MJ, Macri CJ and Cuttitta F. Expression of adrenomedullin and its receptor in normal and malignant human skin: a potential pluripotent role in the integument. Endocrinology 1997; 138: 5597-5604.

[21] Gibbons C, Dackor R, Dunworth W, Fritz-Six K and Caron KM. Receptor activity-modifying proteins: RAMPing up adrenomedullin signaling. Mol Endocrinol 2007; 21: 783-796.

[22] Simonneau G, Montani D, Celermajer DS, Denton CP, Gatzoulis MA, Krowka M, Williams PG and Souza R. Haemodynamic definitions and updated clinical classification of pulmonary hypertension. Eur Respir J 2019; 53:

[23] Lau EM, Manes A, Celermajer DS and Galie N. Early detection of pulmonary vascular disease in pulmonary arterial hypertension: time to move forward. Eur Heart J 2011; 32: 2489-2498.

[24] Harel F, Fu Y, Nguyen QT, Letourneau M, Perrault LP, Caron A, Fournier A and Dupuis J. Use of adrenomedullin derivatives for molecular imaging of pulmonary circulation. J Nucl Med 2008; 49: 1869-1874.

[25] Tuder RM, Stacher E, Robinson J, Kumar R and Graham BB. Pathology of pulmonary hypertension. Clin Chest Med 2013; 34: 639-650.

[26] Dupuis J, Caron A and Ruel N. Biodistribution, plasma kinetics and quantification of single-pass pulmonary clearance of adrenomedullin. Clin Sci (Lond) 2005; 109: 97-102.

[27] Fu Y, Letourneau M, Nguyen QT, Chatenet D, Dupuis J and Fournier A. Characterization of the adrenomedullin receptor acting as the target of a new radiopharmaceutical biomolecule for lung imaging. Eur J Pharmacol 2009; 617: 118-123.

[28] Fu Y, Letourneau M, Chatenet D, Dupuis J and Fournier A. Characterization of iodinated adrenomedullin derivatives suitable for lung nuclear medicine. Nucl Med Biol 2011; 38: 867-874.

[29] Letourneau M, Nguyen QT, Harel F, Fournier A and Dupuis J. PulmoBind, an adrenomedullin-based molecular lung imaging tool. J Nucl Med 2013; 54: 1789-1796.

[30] Harel F, Langleben D, Provencher S, Fournier A, Finnerty V, Nguyen QT, Letourneau M, Levac X, Abikhzer G, Guimond J, Mansour A, Guertin MC and Dupuis J. Molecular imaging of the human pulmonary vascular endothelium in pulmonary hypertension: a phase II safety and proof of principle trial. Eur J Nucl Med Mol Imaging 2017; 44: 1136-1144.

[31] Levac X, Harel F, Finnerty V, Nguyen QT, Letourneau M, Marcil S, Fournier A and Dupuis J. Evaluation of pulmonary perfusion by SPECT imaging using an endothelial cell tracer in supine humans and dogs. EJNMMI Res 2016; 6: 43.

[32] Alonso Martinez LM, Harel F, Nguyen QT, Letourneau M, D'Oliviera-Sousa C, Meloche B, Finnerty V, Fournier A, Dupuis J and DaSilva JN. Al[(18)F]F-complexation of DFH17, a NOTA-conjugated adrenomedullin analog, for PET imaging of pulmonary circulation. Nucl Med Biol 2018; 67: 36-42.

[33] McBride WJ, Sharkey RM, Karacay H, D'Souza CA, Rossi EA, Laverman P, Chang CH, Boerman OC and Goldenberg DM. A novel method of 18F radiolabeling for PET. J Nucl Med 2009; 50: 991-998.

[34] Su AI, Cooke MP, Ching KA, Hakak Y, Walker JR, Wiltshire T, Orth AP, Vega RG, Sapinoso LM, Moqrich A, Patapoutian A, Hampton GM, Schultz PG and Hogenesch JB. Large-scale analysis of the human and mouse transcriptomes. Proc Natl Acad Sci U S A 2002; 99: 4465-4470.

[35] CFR 21 361.1. Available from: https://www.accessdata.fda.gov/scripts/cdrh/cfdocs/cfcfr/CFRSearch.cfm?FR=361.1.

[36] Hay DL, Walker CS and Poyner DR. Adrenomedullin and calcitonin gene-related peptide receptors in endocrine-related cancers: opportunities and challenges. Endocr Relat Cancer 2011; 18: C1-14.

Chapter 3: Al[^{18}F]F-complexation of DFH17, a NOTA-conjugated adrenomedullin analog, for PET imaging of pulmonary circulation

Luis Michel Alonso Martinez[1,2,3], François Harel[2,3,4], Quang T. Nguyen[3], Myriam Létourneau[5], Caroline D'Oliviera-Sousa[3], Bernard Meloche[3], Vincent Finnerty[3], Alain Fournier[5], Jocelyn Dupuis[3,6], Jean N. DaSilva[*,1,2,4]

[1] University of Montreal Hospital Research Centre, 900 rue Saint-Denis, Montréal (Québec) H2X 3H8, Canada

[2] Department of Biomedical Engineering, Faculty of Medicine, Université de Montréal, Pavillon Paul-G. Desmarais, 2960 chemin de la Tour, Montréal (Québec) H3T 1J4, Canada

[3] Research Center of the Montreal Heart Institute, 5000 Rue Bélanger, Montréal (Québec) H1T 1C8, Canada

[4] Department of Radiology, Radio-oncology and Nuclear Medicine, Université de Montréal, Pavillon Roger-Gaudry, 2900 boulevard Edouard Montpetit, Montréal (Québec) H3T 1J4, Canada

[5] Laboratoire d'études moléculaires et pharmacologiques des peptides, INRS-Institut Armand-Frappier, 531 boulevard des Prairies, Laval (Québec) H7V 1B7, Canada

[6] Department of Medicine, Université de Montréal, 2900 boulevard Edouard Montpetit, Montréal (Québec) H3T 1J4, Canada

Nucl Med Biol 2018; 67:36-42. doi:10.1016/j.nucmedbio.2018.10.003

3.1 Abstract

Adrenomedullin receptors are highly expressed in human alveolar capillaries and provide a molecular target for imaging the integrity of pulmonary microcirculation. In this work, we aimed to develop a NOTA-derivatized adrenomedullin analog (DFH17), radiolabeled with [^{18}F]AlF, for PET imaging of pulmonary microcirculation.

Highly concentrated [^{18}F](AlF)$^{2+}$ (15 µL) was produced from purified ^{18}F in NaCl 0.9%. Various complexation experiments were carried out at Al-to-NOTA molar ratios ranging from 1:1 to 1:40 to assess optimal radiolabeling conditions before using the peptide. DFH17 peptide (2 mM, pH 4) was radiolabeled with [^{18}F](AlF)$^{2+}$ for 15 min at 100 ºC in a total volume of 60 µL. As part of the radiolabeling process, parameters such as fluorine-18 activity (~37 and 1480 MBq), concentration of $AlCl_3$ (0.75, 2, 3, 6 or 10 mM) and the effects of hydrophilic organic solvent (aqueous vs ethanol 50%) were studied. The final formulation was tested for purity, identity and stability in saline. Initial *in vivo* evaluation of [^{18}F]AlF-DFH17 was performed in normal rats by PET/CT.

The scaled-up production of [^{18}F]AlF-DFH17 was performed in high radiochemical and chemical purities in an overall radiochemical yield of 22-38% (at end-of-synthesis) within 60 min. The final formulation was stable in saline at different radioactive concentrations for 8 h. PET evaluation in rats revealed high lung-to-background ratios and no defluorination in vivo up to 1 h post-injection. The novel radioconjugate [^{18}F]AlF-DFH17 appears to be a promising PET ligand for pulmonary microcirculation imaging.

Keywords

Concentrated [^{18}F]AlF; NOTA complex; adrenomedullin receptors

3.2 Introduction

Human adrenomedullin (AM) is a vasodilator peptide of 52 amino acids distributed in several tissues but mainly in the adrenal medulla, cardiac ventricles, kidneys and lungs [1]. The biological action of AM, for instance as a potent hypotensive agent, is mediated by the AM receptors constituted by two essential structural components: a seven-transmembrane protein, the calcitonin receptor-like receptor (CLR), and a single transmembrane domain named receptor-activity-modifying protein (RAMP) [2]. The AM1 receptors (CLR/RAMP2) are densely expressed in human alveolar capillaries [3] and provide a potential target for imaging of pulmonary circulation and pulmonary embolism. Pulmonary hypertension, defined as an increase in mean pulmonary artery pressure ≥25 mmHg, is associated with many clinical conditions and carries a poor functional and survival prognosis. Pathophysiologically, it is characterized by endothelial dysfunction of pulmonary microcirculation leading to vasoconstriction and myo-intimal proliferation with progressive loss of lung perfusion [4, 5]. Presently, there are no methods that can directly detect lung microcirculatory damage. ^{99m}Tc-labelled albumin macroaggregates ([^{99m}Tc]Tc-MAA) is an agent currently utilized for imaging pulmonary circulation with Single Photon Emission Computed Tomography (SPECT), but unfortunately and due to its physical size, this tracer is unable to detect functional defects at the microcirculation level in the lungs. Furthermore, it needs to be used with caution because it may further impede flow by blocking pulmonary vessels and shows potential risk of infections since it is a human hemoderivative [6].

PulmoBind is an AM receptor peptide ligand that was developed for molecular diagnosis of pulmonary vascular diseases. PulmoBind has been successfully radiolabeled with technetium-99m via a N_4-chelator (Gly-Gly-D-Ala-Gly) in high radiochemical yield and purity [7]. Clinical phase I and II trials demonstrated that [^{99m}Tc]Tc-PulmoBind administration is safe and provides superior quality SPECT images. It not only can diagnose large perfusion defects caused by pulmonary embolism, as does [^{99m}Tc]Tc-MAA, but also provides additional information with heterogeneous "drop-out" zones indicative of pulmonary vascular disease [8, 9]. The development of a structurally similar ^{18}F-labeled PulmoBind derivative could offer advantages over technetium-99m, such as superior sensitivity and higher spatial resolution of the images obtained with Positron Emission Tomography (PET) facilitating the quantification of AM receptors at the microcirculation level.

Aluminum [^{18}F]fluoride ([^{18}F]AlF) is an attractive radiolabeling approach introduced by McBride *et al.* [10] for fluorination by chelation of peptides and proteins. In the last years, a wide range of NOTA-peptides have been radiolabeled using the Al^{18}F-method [11-15]. Particularly, *N*-hydroxysuccinimide and maleimido-functionalized pentadentate NOTA derivatives has been previously shown to allow proper coordination chemistry with Al bound to flourine-18 [12, 15, 16]. In comparison with other radiofluorination reactions, this emerging strategy allows a one-step radiolabeling of peptides in aqueous solutions increasing the reaction yield, facilitating the radioconjugate purification, and considerably reducing total synthesis time [17].

DFH17 is a novel NOTA-peptide derived from a pegylated analog of the 22 to 52 peptide segment of AM (**Figure 1**). This peptide is an antagonist that shows a higher selectivity for the AM_1 (CLR/RAMP2) than for the AM_2 (CLR/RAMP3) receptor subtypes [7, 18]. Here, we describe the radiosynthesis of DFH17 labeled with fluorine-18 via the Al^{18}F-approach for PET imaging of

AM receptors in pulmonary microcirculation. To pursue our goal, a semi-automatic system was developed to produce highly concentrated $[^{18}F](AlF)^{2+}$. Furthermore, various complexation experiments with pentadentate NOTA were performed to assess the optimal radiolabeling conditions before using the more expensive peptide. Finally, PET imaging and biodistribution studies were conducted in normal rats to evaluate its suitability as a PET radioligand for AM receptors.

3.3. Material and methods

3.3.1. General

All reagents (Grade: trace metal basis) and solvents were purchased from Sigma-Aldrich (St-Louis, MO, USA) and J. T. Baker (Philipsburg, NJ, USA). Solutions were prepared with Chelex 100 (Bio-Rad, France) treated metal free water. NOTA (1,4,7-Triazacyclononane-1,4,7-triacetic acid) and maleimido-mono-amide-NOTA (1,4,7-Triazacyclononane-1,4-bis-acetic acid-7-maleimidoethylacetamide) were obtained from Macrocyclics, Inc (Dallas, TX, USA).

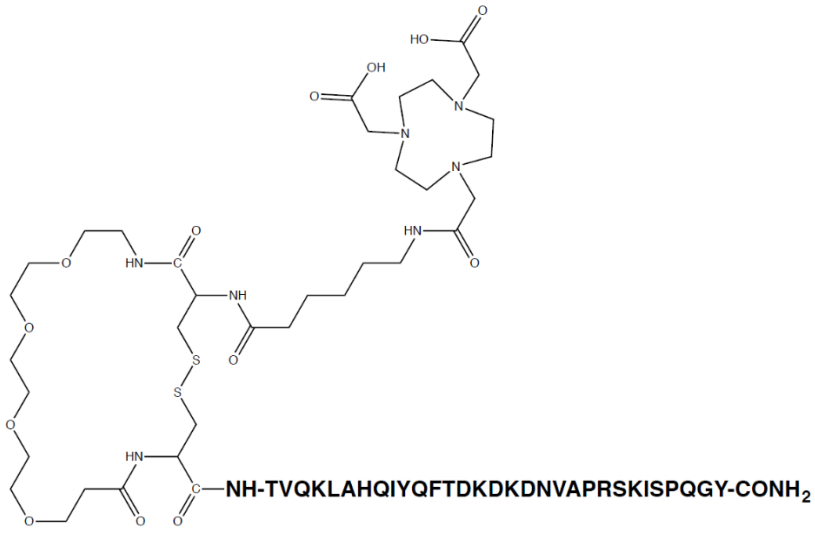

Figure 1. Chemical structure of DFH17, a NOTA-peptide derived from a pegylated analog of the 22 to 52 peptide segment of AM.

Analytical high performance liquid chromatography (HPLC) was carried out by two methods. *Method 1*: CSC-Kromasil C-18 reverse-phase column (4.6x250 mm 5 µm) following a linear gradient of acetonitrile (0-60%) in water containing 0.1% TFA at flow rate of 1 mL/min for 30 min. *Method 2*: Waters XBridge C-18 reverse-phase column (3x150 mm 3.5 µm) following a linear gradient of acetonitrile (20-40%) in water containing 0.1% TFA at flow rate of 0.8 mL/min for 40 min. Semi-preparative HPLC was performed on a Vydac C-18 reverse-phase column (14x250 mm 10 µm) following a linear gradient of acetonitrile (10-45%) in water containing 0.1% TFA at a flow rate of 3 mL/min. The eluate was analyzed for absorbance at 220 nm using a Waters 2998 photodiode array detector and for radioactivity using a radiometric flow scintillation analyzer coupled via a Waters e-SAT/IN device.

Instant thin layer chromatography-silica gel (ITLC-SG) papers (Merck, Germany) were developed in citric acid pH 1.6 (*Method 1*), and with a mixture of butanol:acetic acid:pyridine:water

(5:1:4:3) (*Method 2*). Radio-chromatograms were acquired with an AR-2000 radio-TLC imaging scanner (Eckert & Ziegler, Germany).

3.3.2 Preparation of NOTA-adrenomedullin derivative (DFH17)

The NOTA derivative DFH17 was synthesized following a similar approach used for PulmoBind [7]. Briefly, a Cys-dPEG$_4$-Cys segment was coupled onto the hAM(22-52) via standard Fmoc-based solid-phase peptide chemistry. Fmoc-aminohexanoic acid (Fmoc-Aca-OH, Chem-Impex International, IL, USA) was then incorporated to the hAM(22-52)-Cys-dPEG$_4$-Cys peptide N-terminal position, serving as spacer between the peptide and the chelator. Subsequently, the Fmoc moiety was removed from spacer with 20% piperidine/N,N-dimethylformamide (DMF). Prior to conjugation, NOTA was activated via N-hydroxysuccinimide (NHS) at room temperature for 20 min (NOTA 2 eq; NHS 3 eq; 1-ethyl-3-(3-dimethylaminopropyl)carbodiimide 6 eq according to peptide-resin). The conjugation was performed at room temperature for 20 h by the addition of NOTA-NHS ester to the peptide-resin suspended in 15% (v/v) triethylamine/DMF. Finally, the peptide was cleaved from the resin as previously described by Fu *et al.* [18] to yield crude linear DFH17. Cyclization of DFH17 through disulfide bond formation was achieved by air oxidation in the presence of EDTA (ethylenediaminetetraacetic acid). Crude cyclic DFH17 was purified by semi-preparative HPLC and the collected fractions were analyzed by analytical RP-HPLC (*Method 1*) and MALDI-TOF mass spectroscopy (MicroFlex LRF, Bruker Daltonics, Milton, Canada) in positive mode with α-cyano-4-hydroxycinnamic acid as the ionization matrix. Fractions corresponding to the desired compound were pooled and lyophilized.

3.3.3. Formation of binary Al^{18}F-complex

Concentrated [^{18}F](AlF)$^{2+}$ was obtained for peptide labeling in a total volume of approximately 15 µL as follow. The semi-automatic elution system placed in a Class A hot cell was designed with a 3-way manifold mixing solenoid valve (Cole-Parmer, IL, USA) that allowed connecting the ^{18}F-cyclotron line, a water rinse line, and a line for eluting fluorine-18 with saline to a MP-1 small anion exchanger cartridge (^{18}F-Trap & Release II, ORTG, TN, USA) (see **Figure S1**). Fluorine-18, produced via the nuclear reaction ^{18}O(p,n)^{18}F with our IBA Cyclone 18/9 cyclotron, was trapped onto the cartridge, rinsed with 3 mL water followed by a bolus of 375 µL 0.9% NaCl. Concentrated fluorine-18 was then eluted with additional fractions of 0.9% NaCl (10 µL) and dispensed semi-automatically via a Valco 12 port valve (VICI, EMT2CSD12UW, TX, USA) into small reaction vessels (1-mL V-vial, Wheaton) containing 5 µL of $AlCl_3$ (tested at various concentrations 0.1, 0.3, 0.5, 1, 2, 3, 4 or 20 mM) in sodium acetate buffer (0.1 M, pH 4). The solutions were incubated at RT for 10 min to form [^{18}F](AlF)$^{2+}$.

[^{18}F](AlF)$^{2+}$ production from fluorine-18 was estimated following cation trapping on a cationic exchange MCX cartridge (Waters, MA, USA). As control, fluorine-18 loaded on the same cartridge was completely washed with 30 mL of water. The [^{18}F](AlF)$^{2+}$ formation yield was determined by comparing the radioactivity eluted with water (free fluorine-18) and the total radioactivity trapped on the cation exchange resin.

3.3.4. Complexation assay with NOTA chelator

Al^{18}F-complexation with maleimido-functionalized NOTA was assayed in different $AlCl_3$-to-NOTA molar ratio as follow. Approximately 37 MBq (~12 µL) of ^{18}F was added to 2 mM $AlCl_3$ in sodium acetate buffer (0.1 M, pH 4), and then incubated at room temperature for 15 min.

[^{18}F](AlF)$^{2+}$ was added to stock solutions of NOTA (ranging from 10 - 400 mM) to provide the radioflourinated $AlCl_3$-to-NOTA molar ratios 1:1, 1:3, 1:5, 1:8, 1:10, 1:15, 1:30 or 1:40 (**Scheme 1**). The reaction mixtures were heated at 100 °C for 15 min. The [^{18}F]AlF-NOTA complexes were analyzed by ITLC-SG following the *Method 1* and the crude RCYs were calculated with the WinScan v3.14 software.

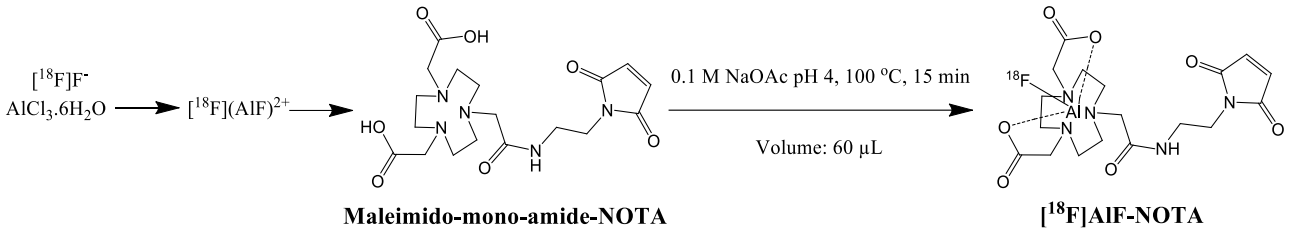

Scheme 1. Al^{18}F-complexation assays with pentadentate NOTA chelator.

3.3.5. Radiosynthesis of [^{18}F]AlF-DFH17

Activities of [^{18}F](AlF)$^{2+}$ (10 µL, 30-37 MBq) were used to radiolabel the NOTA-conjugate DFH17 (2 mM). Radiolabeling was performed at 100 °C for 15 min in 0.1 M sodium acetate pH 4 with a total reaction volume of 50-60 µL (**Scheme 2**). Ethanol (50% v/v) was used to improve the labeling efficiency. After heating the reaction mixture, the RCY was determined based on the proportion of radioactivity eluted from the HPLC column.

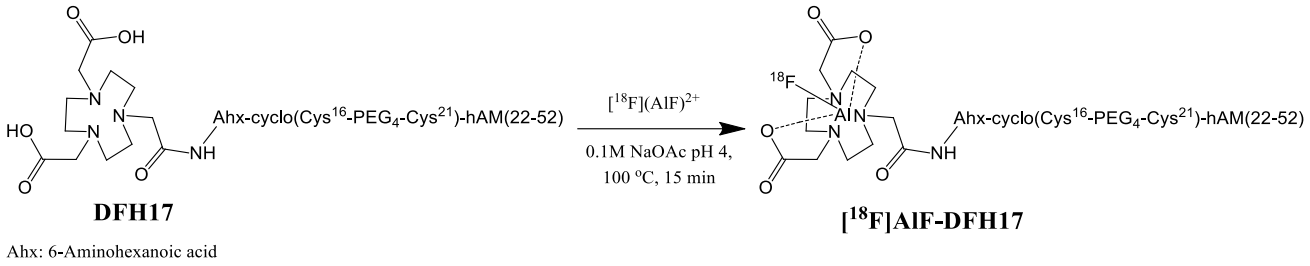

DFH17

Ahx: 6-Aminohexanoic acid

[^{18}F]AlF-DFH17

Scheme 2. Radiosynthesis of [^{18}F]AlF-DFH17.

3.3.5.1. Effect of fluorine-18 activity and Al^{3+} concentration (Scale-up)

The influence of Al^{3+} concentration with higher fluorine-18 activities was studied in the production of [^{18}F]AlF-DFH17. [^{18}F]F^- (10 µL, 1110-2405 MBq) was added to 5 µL $AlCl_3$ (0.75, 2, 3, 6 or 10 mM) to form [^{18}F](AlF)$^{2+}$ using our semi-automatic system. To a crimped vial containing [^{18}F](AlF)$^{2+}$, 15 µL of DFH17 (2 mM) and 30 µL of ethanol were added and the reaction was heated as described in the previous section. The crude mixture was then quenched with 1 mL of 0.1 M sodium acetate pH 4 and purified through a C-18 SepPak cartridge. After loading the sample, the cartridge was washed with 30 mL of water for injection to remove free [^{18}F](AlF)$^{2+}$ and then with 1 mL of 10 mM HCl in ethanol to elute the labeled peptide. The ethanol was evaporated under a gentle stream of N_2 and the dry residue was re-dissolved in saline. The final formulation was filtered (0.2 µm Acrodisc® Nylon, Pall Corp, NY, USA).

3.3.5.2. Analytical studies

The final formulation was assayed in various quality control tests as described in EU and US pharmacopoeias for other radiopharmaceuticals [19-21]. Briefly, the pH was determined by pH strips (BDH, Germany). The radiochemical purity was determined by RP-HPLC and by ITLC-

SG (*Method 2*). The radionuclide identification/radionuclidic purity was verified in an ionization chamber based activity meter (Capintec Radioisotope Calibrator CRC-55tPET and CRC-55t well counter, NJ, USA). Organic residual solvent (ethanol) was determined by Gas Chromatography (Agilent 7980B, CA, USA). Evaluation of microbiological integrity of the product and performance of the aseptic processing was assessed by filter integrity using the bubble point (≥60 psi) or pressure retaining tests (Calibrated manometer, Swagelok, OH, USA) (see Appendix A. Supplementary data, **Table S1** for specifications).

3.3.6. Stability tests of [^{18}F]AlF-DFH17 in saline with and without radioprotectant

The stability of radiolabeled peptide was evaluated in normal saline at room temperature (RT). The purified conjugate [^{18}F]AlF-DFH17 (~155 MBq/mL) was incubated in saline and the radiochemical purity was determined by ITLC-SG (*Method 2*) at 4 and 8 h. Similar experiments were repeated at higher radioactive concentration of [^{18}F]AlF-DFH17 (~664 MBq/mL) in the presence of ascorbic acid as radioprotectant (0.15 mg per 30 nmol of DFH17).

3.3.7. PET imaging and biodistribution

Animal experiments were carried out in compliance with the Institutional Animal Protection Committee of Montreal Heart Institute following the guidelines of the Canadian Council on Animal Care. CT images and Dynamic PET were acquired on a PET-CT clinical imaging system (Siemens Biograph mCT Flow 40, Germany). Sprague-Dawley rats (423-538 g, n=4) were anesthetized via the tail vein using between 0.4 and 0.55 mL of a ketamine/xylazine 1:1 solution (1 µL/g). Whole-body PET images of [^{18}F](AlF)$^{2+}$ and [^{18}F]AlF-DFH17 (~74 MBq, 0.3 mL) were acquired (6 x 10 minutes frames), 15 minutes after radiopharmaceutical injection (tail vein). Example images are presented as maximum intensity projection (MIP) in **Figure 7**. Animals were

sacrificed by 1 mL 10% KCl injection via caudal vein at above specified time points and organs of interest were collected and weighed.

On the acquisition workstation (Siemens PETsyngo VG60A, Germany), the PET emission data were corrected for detector normalization, dead time, non-uniform tissue attenuation, radioactive decay, photon scattering, and random coincidences. The tomographic datasets were reconstructed using the three-dimensional ordered-subsets expectation maximization (OSEM) iterative reconstruction algorithm including attenuation correction (AC), time of flight (TOF) and point spread function (PSF), using 8 iterations and 21 subsets. Regions of interest (ROIs) were drawn semi-automatically using ITK-snap 3.6.0 and analyzed using an "in-house" software programmed with MATLAB 2016b (Mathworks, Natick, MA, USA). Biodistribution into organs with significant uptake were expressed as percentage of the total radioactivity injected.

3.3.8. Statistical analysis

All data are presented as mean ± standard deviation. N values for each comparison are given in the figures. Statistical analysis was performed using STATGRAPHICS Plus version 5.1 (Warrenton, VA, USA). Results were compared using two-tailed t-test (parametric) and Mann-Whitney test (non-parametric); $p<0.05$ was considered significant.

3.4 Results

3.4.1. Preparation of NOTA-adrenomedullin derivative (DFH17)

The NOTA-adrenomedullin derivative DFH17 (9.5 mg) was obtained from peptide-resin (200 mg) in an overall yield of 9%. Purity of the final DFH17 product was determined to be of 94% with an observed molecular mass of 4426.88 (theoretical average molecular mass: 4426.04) (see Appendix A. Supplementary data, **Figure S1a** and **b**).

3.4.2. Formation of binary Al^{18}F-complex

The typical elution profile of fluorine-18 in MP-1 cartridge is shown in **Figure 2**. Concentrated [^{18}F]F$^-$ was obtained with our semi-automatic system (see Appendix A. Supplementary data, **Figure S2**) in 10 µL of 0.9% NaCl (corresponding to approximately 10% of total activity), enabling high activities of fluorine-18 in the reaction vial to form *in situ* the binary Al^{18}F-complex.

Formation yield of Al^{18}F-complex as a function of $AlCl_3$ concentration is depicted in **Figure 3**. High yields (~90%) of the Al^{18}F-complex were obtained with 0.3-20 mM $AlCl_3$. In contrast, lower concentrations of $AlCl_3$ (0.3 mM) only produced approximately 30% of Al^{18}F-complex. Therefore, 2-3 mM of $AlCl_3$ was used in radiolabeling experiments.

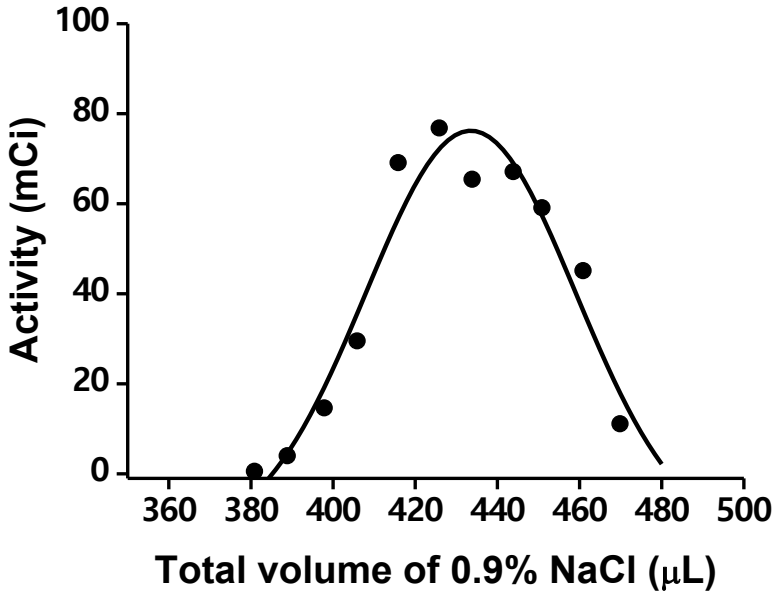

Figure 2. Typical elution profile of fluorine-18 from a MP-1 cartridge. After rinsing with 3 mL of water followed by a bolus of 375 µL of saline, concentrated fluorine-18 was eluted with additional fractions of 0.9% NaCl (10 µL).

3.4.3. Complexation assay with NOTA

Complexation yields higher than 80% were obtained with 1:1, 1:3 and 1:5 $[^{18}F](AlF)^{2+}$-to-NOTA ratios (**Figure 4** and Appendix A. Supplementary data **Figure S3c**, **d** and **e**). No statistical differences (p=0.09) were found between the $[^{18}F](AlF)^{2+}$-to-NOTA ratio of 1:1 to 1:3 and 1:1 to 1:5. While the 1:5 $[^{18}F](AlF)^{2+}$:NOTA molar ratio gave 81%, higher quantities of chelator are needed to reach the same complexation yield with 1 to 3 $[^{18}F](AlF)^{2+}$-to-NOTA ratio. Taking this into account, 1:1 and 1:3 $[^{18}F](AlF)^{2+}$:NOTA molar ratios were chosen to radiolabel the DFH17.

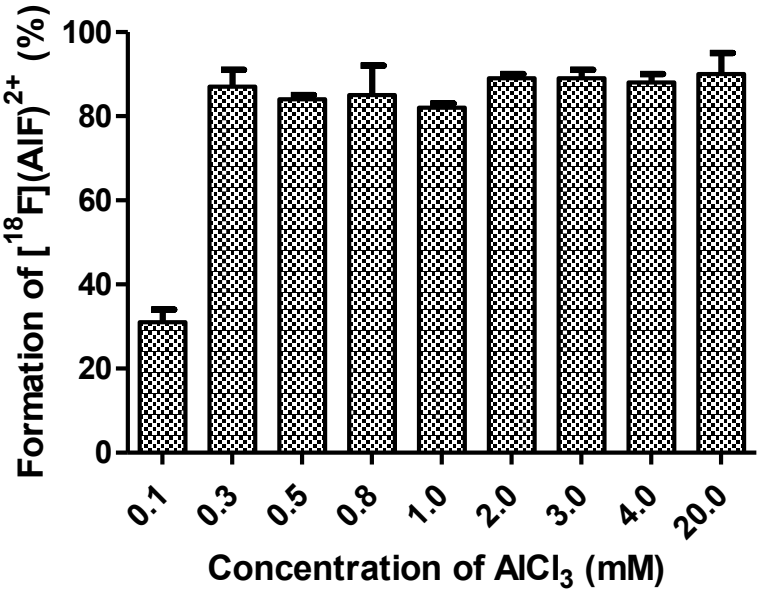

Figure 3. Formation of $[^{18}F](AlF)^{2+}$ at different concentrations of $AlCl_3$ (n=3 per concentration).

3.4.4. Radiolsynthesis of [^{18}F]AlF-DFH17

Radiolabeling experiments in aqueous conditions at low activities (~37 MBq) with $[^{18}F](AlF)^{2+}$-to-DFH17 molar ratio 1:3 is shown in Appendix A. Supplementary data, **Figure S4a**. The RCY of the crude labeling reaction as estimated by radio-HPLC was increased up to 92% by the addition of ethanol to the reaction mixture (see Appendix A. Supplementary data, **Figure S4b**) Taking this into account, 50% ethanol (v/v) was chosen in all subsequent radiofluorination experiments.

Radiosynthesis of [^{18}F]AlF-DFH17 at higher activities (1110-2405 MBq) resulted in lower yields compared to low-scale activities (See Appendix A. Supplementary data, **Figure S4c**). We hypothesized that higher activities of fluorine-18 require higher concentrated $AlCl_3$ solution levels

for optimal complexation. We then performed a series of radiolabeling experiments at different concentrations of $AlCl_3$ as shown in **Figure 5**. Contrary to our hypothesis, concentrations higher than 6 mM $AlCl_3$ reduced the RCY and optimal conditions were found at 2-3 mM $AlCl_3$. Therefore, we decided to use these $AlCl_3$ concentrations in all subsequent scaling-up radiosynthesis of [^{18}F]AlF-DFH17.

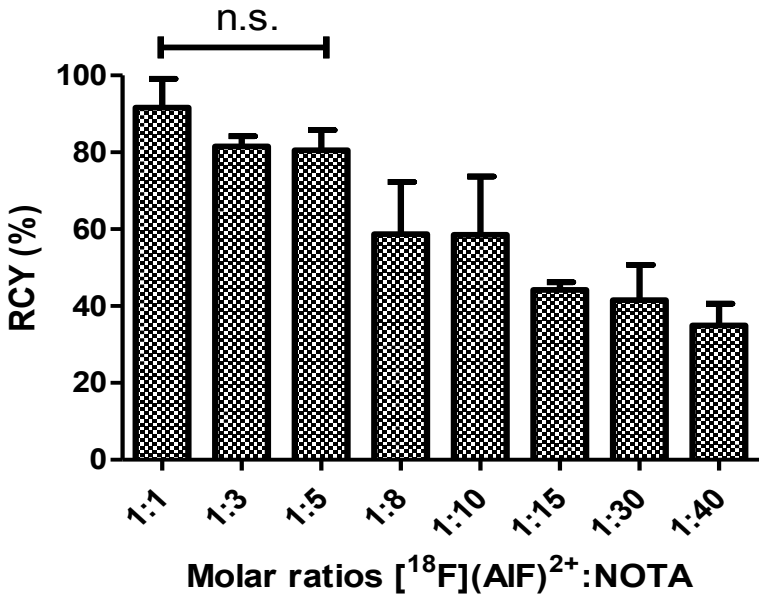

Figure 4. Complexation assay with pentadentate NOTA chelator (n=3 per molar ratio, n.s. = no significant difference, p=0.09).

The optimized radiosynthesis of [^{18}F]AlF-DFH17 resulted in RCYs of 22-38% (n=6, decay-corrected to fluroine-18 at start-of-synthesis) in a total preparation time of 63 min. The final formulation was tested for appearance, identity, purity, residual organic solvent and microbiological integrity. The product [^{18}F]AlF-DFH17 met the acceptance criteria for parenteral radiopharmaceuticals used for in vivo PET imaging studies (See Appendix A. Supplementary data, **Table S1** and **Figure S5**).

3.4.5. Stability tests of [^{18}F]AlF-DFH17 in saline with and without radioprotectant

As shown in **Figure 6**, the radioconjugate exhibited high *in vitro* stability in saline for 8 h at low radioactive concentration (~155MBq/mL) without ascorbic acid. The percentage of intact [^{18}F]AlF-DFH17 was between 95-99% (no statistical difference, p=0.38) in the formulation up to 664MBq/mL within 8 h from end-of-synthesis (EOS).

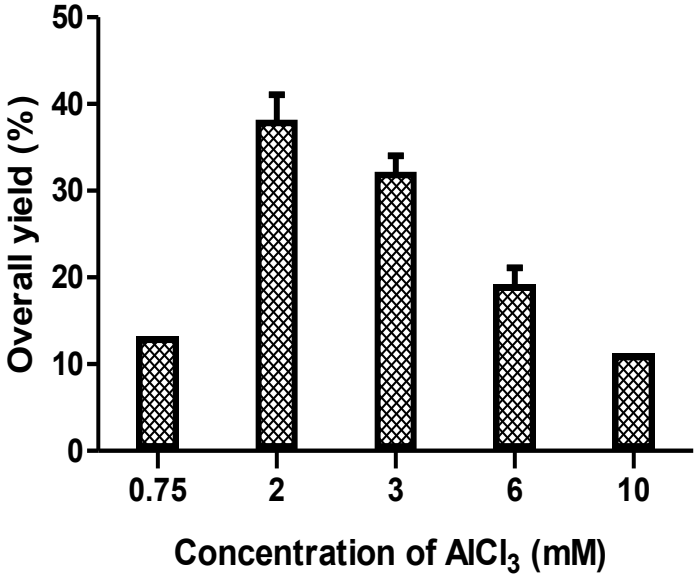

Figure 5. Radiolabeling of [^{18}F]AlF-DFH17 (Scale-up) at different concentrations of $AlCl_3$ with ethanol 50% (v/v) (n=3 per concentration).

3.4.6. PET imaging and biodistribution

PET/CT image of [^{18}F](AlF)$^{2+}$ and [^{18}F]AlF-DFH17 in normal Sprague-Dawley rats are presented in **Figure 7**. As expected, high uptake of [^{18}F](AlF)$^{2+}$ in the bones was found during all time points (**Figure 7a**). Compared to the control animal, high tracer accumulation was observed in the lungs 5 min post-injection (**Figure S6**), which persisted for 1 h (**Figure 7b,c**). Rapid

accumulation in kidneys was observed during the first 15 min which suggests clearance via urinary bladder (**Figure 7b,c**). Interestingly, the absence of radioactivity in the bones even at 1 h indicates in vivo stability of [^{18}F]AlF-DFH17, since no transmetalation was observed from the compound either as free [^{18}F]F^- or [^{18}F](AlF)$^{2+}$ (**Figure 7c** and Appendix A. Supplementary data, **Figure S6b**). Uptake in the non-target organs was considerably low.

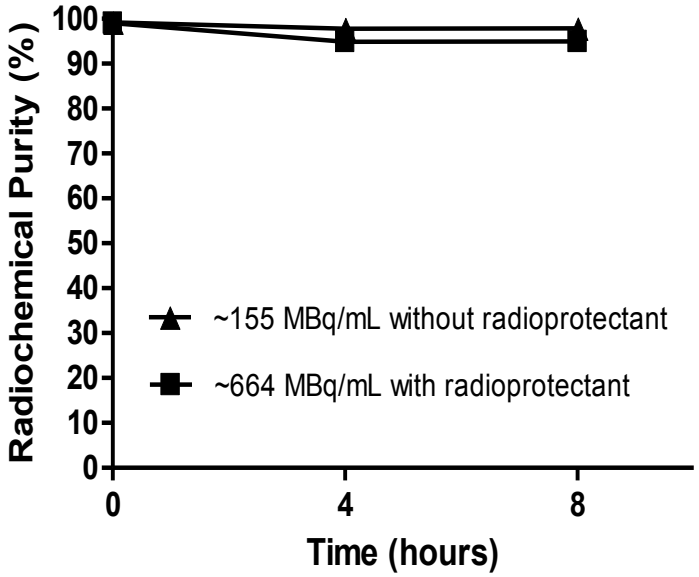

Figure 6. Stability of [^{18}F]AlF-DFH17 in saline at two different radioactive concentrations. Ascorbic acid as radioprotectant (n=3 per time point).

3.5. Discussion

Complexation of aluminum [^{18}F]fluoride is a versatile approach of peptide labeling that can be accomplished without a drying step needed for most ^{18}F-labeling methods. Nevertheless, an fluorine-18 purification step from [^{18}O]H_2O is usually required to achieve higher complexation yields. Commercial cartridges such as QMA SepPak or Chromafix PS-HCO_3 were previously used to purify flourine-18 in volumes ranging from 100 to 500 µL of 0.9% NaCl [22, 23]. In preliminary

experiments with [^{18}F]AlF, the total reaction volume was found to be a critical parameter for high radiochemical yields. For this reason, we developed an semi-automatic system to generate highly concentrated [^{18}F](AlF)$^{2+}$ from purified [^{18}F]F^{-} (in NaCl 0.9%). Our elution process was reproducible and successfully used in all experiments, thus considerably minimizing the radiation exposure to the hands. In addition, we proposed a simple method to estimate the formation of the Al^{18}F-binary complex by [^{18}F](AlF)$^{2+}$cation trapping in a MCX cartridge. Kersemans *et al.* [24] recently reported a similar method in where nearly 80% of [^{18}F](AlF)$^{2+}$ was trapped in a WCX cartridge when 50 nmol of Al^{3+} was used. Although both approaches gave comparable results, these methods have the limitation of not being able to differentiate between the binary AlF-cationic species [25] such as (AlF)$^{2+}$ and (AlF$_2$)$^{+}$ in case that (AlF$_2$)$^{+}$ was also formed in solution.

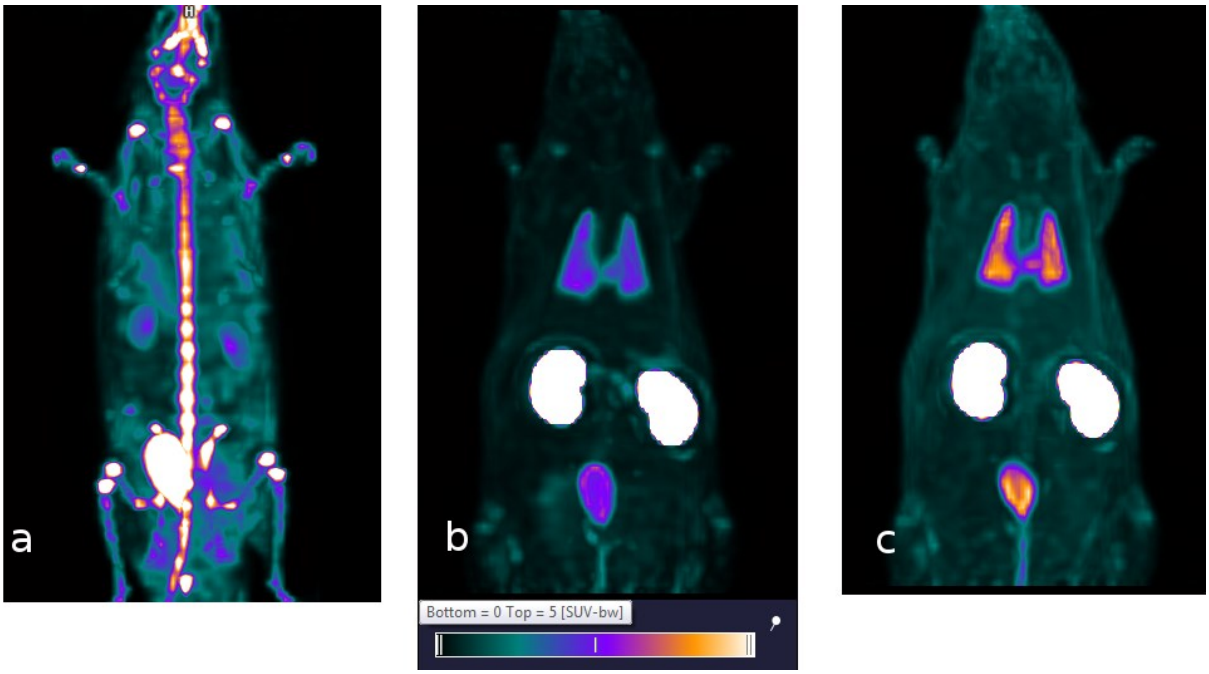

Figure 7. (a) Maximal intensity projections (MIP) images for PET/CT imaging of [^{18}F](AlF)$^{2+}$ after 1 h scan. **(b)** [^{18}F]AlF-DFH17 after 15 min and **(c)** 1 h scan.

Radiolabeling conditions were first optimized using a complexation assay with the inexpensive pentadentate NOTA chelator, before using the more expensive DFH17 peptide. $[^{18}F](AlF)^{2+}$-to-NOTA molar ratios 1:1, 1:3 and 1:5 gave comparable results while a high excess of chelator reduced the RCY down to 40%. Farkas *et al.* [26] studied the equilibria and dissociation kinetics of the Al(NOTA) complex. Their findings concluded that the formation kinetics of Al(III)-$NOTA^{3-}$-H^{+}-F^{-} four-component system are fairly complicated and further experiments should be performed to properly understand the formation kinetics of this complex. Attempts to explain the complexation kinetics with increasing $[^{18}F](AlF)^{2+}$-to-NOTA molar ratios was beyond the scope of this study, however a similar pattern has been previously reported by others using NOTA-conjugated molecules [12, 13, 23]. As result of the $Al^{18}F$-complexation assays with NOTA, the $(Al^{18}F)^{2+}$-to-DFH17 molar ratio 1:3 resulted in high RCYs that were further increased with the addition of ethanol. Previous studies have demonstrated that the addition of organic solvents to the reaction mixture improved RCYs for similar labeling processes [12, 22, 27, 28]. The effect of hydrophilic solvents breaking the hydrogen bonds between the water molecules was reported by Idrissi and Longelin [29]. Using Raman spectroscopy, they demonstrated that aqueous solutions containing isopropanol produce a small displacement towards lower frequencies of the peak associated with the hydrogen bonding of the water molecules. Their findings could suggest a breakup of the $Al^{18}F$-hydration shell in the presence of ethanol facilitating the interaction of the metal cations with donors in the chelate structure and therefore, giving rise to higher RCYs than in aqueous solutions (without addition of an alcohol).

Scaling-up the radiosynthesis of $[^{18}F]$AlF-DFH17 at higher activities resulted in lower yields compared to low-scale activities. Wan *et al.* [12] reported a similar behavior while using higher activities of fluorine-18 in labeling a NOTA-RGD derivative via $[^{18}F]$AlF. Their results gave 40% RCY with activities ranging from 740 to 2590 MBq, but dropped to 15% when more than 2812

MBq of [^{18}F]F^{-} was used. Lower labeling yields appear to be related to the type of Al^{18}F-binary complex that is formed in solution. Hem [[30]] reported the presence of the following AlF binary species: $(AlF)^{2+}$, $(AlF_2)^{+}$, AlF_3, $(AlF_4)^{-}$,$(AlF_5)^{2-}$ and $(AlF_6)^{3-}$ in aqueous solution. Using X-ray crystallography, only $(AlF)^{2+}$ was found to form a stable compound with a macrocyclic chelator [31]. Taking this into account, lower complexation yields could be the result of increased formation of $(AlF_2)^{+}$ and AlF_3 when high activities and/or low molar activities of fluorine-18 are used [32].

High radioactive concentration can lead to radiolytic decomposition by the formation of superoxide and hydroxyl radicals [33]. Well-known radical scavengers such as gentisic or ascorbic acid have been used previously in radioactive formulations to prevent their radiolytic decomposition following an electron transfer reaction from superoxide to electron-accepting groups in the ascorbate group [34, 35]. Thus, using the optimal value reported by McBride *et al.* [36], a quantity of 0.15 mg ascorbic acid per 30 nmol of peptide was added to the mixture, so the radiotracer stored at RT can be used for PET imaging within 8 h after EOS (at 95% radiochemical purity).

AM receptors, formed by the association of the CLR and RAMP2 or RAMP3, are predominantly the way of clearance of circulating AM [4]. Due to the high density of AM receptors in the cardiorespiratory system and that its metabolism occurs via receptor binding in the lungs, we proposed that AM receptors could represent a potential target for imaging disorders of pulmonary microcirculation. Higher resolution images were obtained with [^{18}F]AlF-DFH17 using PET compared to other AM derivatives such as [^{99m}Tc]Tc- linear AM, cyclic-DTPA AM and PulmoBind [6, 7] by SPECT. However, ~3% of the injected dose was found in the lungs at 30 min post-injection (see Appendix A. Supplementary data, **Figure S6b**). This result contrasts with the

retention of [^{99m}Tc]Tc-linear AM (~14 %ID)[37] and [^{99m}Tc]Tc-PulmoBind (~12 %ID)[7] in the lungs at the same post-injection time. Particularly, the differences with PulmoBind appeared intriguing because both radioconjugates are based on the human 22-52 AM fragment with minor structural differences in the type of chelator (acyclic N_4 vs macrocyclic NOTA). More work is required in order to determine the factors, such as molar activity and imaging modality, involved in this discrepancy. In spite of this, both radioconjugates exhibited similar biodistribution profiles with high lung retention for up to 1 h and elimination via the urinary system. Finally, our findings revealed that [^{18}F]AlF-DFH17 was able to image the lungs with high signal-to-noise ratio and with high in vivo stability. Based on this, [^{18}F]AlF-DFH17 could offer a new modality of PET imaging of the pulmonary microcirculation with greater resolution and sensitivity.

3.6. Conclusions

The novel radioconjugate [^{18}F]AlF-DFH17 was radiolabeled with concentrated [^{18}F]$(AlF)^{2+}$ produced by an "in-house" semi-automatic system. Complexation assays with NOTA chelator simulated the radiolabeling conditions and facilitated the radiolabeling optimization of DFH17. The production of [^{18}F]AlF-DFH17 was carried out in high radiochemical and chemical purities. PET/CT and biodistribution demonstrated high [^{18}F]AlF-DFH17 lung-to-background ratio and in vivo stability in rats. The AM-derived [^{18}F]AlF-DFH17 radioligand appears as a promising PET imaging tracer for further pre-clinical investigations.

3.7 Acknowledgments

This project was financially supported by Université de Montréal - MERCK SHARP & DOHME Inc. fund. The authors would like to thank Michael Klimas, executive director, imaging franchise lead, Merck USA, for kindly providing the pegylated analog of AM (fragment 22-52) freight substance. The authors gratefully acknowledge the staff of the Radiochemistry and Cyclotron platform at University of Montreal Hospital Centre (CRCHUM), as well as all members of the Research Centre and Department of Nuclear Medicine at Montreal Heart Institute.

3.8 References

[1] Sugo S, Minamino N, Kangawa K, Miyamoto K, Kitamura K, Sakata J, *et al*. Endothelial cells actively synthesize and secrete adrenomedullin. Biochem Biophys Res Commun 1994;201:1160-6.

[2] Conner AC, Simms J, Hay DL, Mahmoud K, Howitt SG, Wheatley M, *et al*. Heterodimers and family-B GPCRs: RAMPs, CGRP and adrenomedullin. Biochem Soc Trans 2004;32:843-6.

[3] Hagner S, Stahl U, Knoblauch B, McGregor GP, and Lang RE. Calcitonin receptor-like receptor: identification and distribution in human peripheral tissues. Cell Tissue Res 2002;310:41-50.

[4] Yanagawa B and Nagaya N. Adrenomedullin: molecular mechanisms and its role in cardiac disease. Amino Acids 2007;32:157-64.

[5] Dupuis J, Harel F, and Nguyen QT. Molecular imaging of the pulmonary circulation in health and disease. Clin Transl Imaging 2014;2:415-26.

[6] Harel F, Fu Y, Nguyen QT, Letourneau M, Perrault LP, Caron A, *et al*. Use of adrenomedullin derivatives for molecular imaging of pulmonary circulation. J Nucl Med 2008;49:1869-74.

[7] Letourneau M, Nguyen QT, Harel F, Fournier A, and Dupuis J. PulmoBind, an adrenomedullin-based molecular lung imaging tool. J Nucl Med 2013;54:1789-96.

[8] Levac X, Harel F, Finnerty V, Nguyen QT, Letourneau M, Marcil S, *et al*. Evaluation of pulmonary perfusion by SPECT imaging using an endothelial cell tracer in supine humans and dogs. EJNMMI Res 2016;6:43.

[9] Harel F, Langleben D, Provencher S, Fournier A, Finnerty V, Nguyen QT, *et al*. Molecular imaging of the human pulmonary vascular endothelium in pulmonary hypertension: a phase II safety and proof of principle trial. Eur J Nucl Med Mol Imaging 2017;44:1136-44.

[10] McBride WJ, Sharkey RM, Karacay H, D'Souza CA, Rossi EA, Laverman P, *et al*. A novel method of 18F radiolabeling for PET. J Nucl Med 2009;50:991-8.

[11] Laverman P, McBride WJ, Sharkey RM, Eek A, Joosten L, Oyen WJ, *et al*. A novel facile method of labeling octreotide with (18)F-fluorine. J Nucl Med 2010;51:454-61.

[12] Wan W, Guo N, Pan D, Yu C, Weng Y, Luo S, *et al*. First experience of 18F-alfatide in lung cancer patients using a new lyophilized kit for rapid radiofluorination. J Nucl Med 2013;54:691-8.

[13] Blasi F, Oliveira BL, Rietz TA, Rotile NJ, Day H, Looby RJ, *et al*. Effect of Chelate Type and Radioisotope on the Imaging Efficacy of 4 Fibrin-Specific PET Probes. J Nucl Med 2014;55:1157-63.

[14] Hausner SH, Bauer N, and Sutcliffe JL. In vitro and in vivo evaluation of the effects of aluminum [(1)(8)F]fluoride radiolabeling on an integrin alphavbeta(6)-specific peptide. Nucl Med Biol 2014;41:43-50.

[15] Liu Q, Pan D, Cheng C, Zhang D, Zhang A, Wang L, *et al*. Development of a Novel PET Tracer [18F]AlF-NOTA-C6 Targeting MMP2 for Tumor Imaging. PLoS One 2015;10:e0141668.

[16] Kumar K and Ghosh A. (18)F-AlF Labeled Peptide and Protein Conjugates as Positron Emission Tomography Imaging Pharmaceuticals. Bioconjug Chem 2018;29:953-75.

[17] McBride WJ, Sharkey RM, and Goldenberg DM. Radiofluorination using aluminum-fluoride (Al18F). EJNMMI Res 2013;3:36.

[18] Fu Y, Letourneau M, Nguyen QT, Chatenet D, Dupuis J, and Fournier A. Characterization of the adrenomedullin receptor acting as the target of a new radiopharmaceutical biomolecule for lung imaging. Eur J Pharmacol 2009;617:118-23.

[19] Convention USP. Fludeoxyglucose F 18 Injection. USP 29, NF 24: the United States Pharmacopeia, the National Formulary

United States Pharmacopeial Convention; 2005, p. 933.

[20] European pharmacopoeia. 7.8 Strasbourg: Council of Europe; 2013.

[21] Pharmacopoeia E. Gallium (68Ga) Edotreotide Injection. European Pharmacopoeia 2014: Supplement 8. 0: Council of Europe; 2013, p. 1062-4.

[22] Laverman P, D'Souza CA, Eek A, McBride WJ, Sharkey RM, Oyen WJ, *et al*. Optimized labeling of NOTA-conjugated octreotide with F-18. Tumour Biol 2012;33:427-34.

[23] Malik N, Zlatopolskiy B, Machulla H-J, Reske SN, and Solbach C. One pot radiofluorination of a new potential PSMA ligand [Al18F]NOTA-DUPA-Pep. Journal of Labelled Compounds and Radiopharmaceuticals 2012;55:320-5.

[24] Kersemans K, De Man K, Courtyn J, Van Royen T, Piron S, Moerman L, *et al*. Automated radiosynthesis of Al[(18)F]PSMA-11 for large scale routine use. Appl Radiat Isot 2018;135:19-27.

[25] Bruce Martin R. Ternary complexes of Al3+ and F− with a third ligand. Coordination Chemistry Reviews 1996;149:23-32.

[26] Farkas E, Fodor T, Kálmán FK, Tircsó G, and Tóth I. Equilibrium and dissociation kinetics of the [Al(NOTA)] complex (NOTA = 1,4,7-triazacyclononane-1,4,7-triacetate). Reaction Kinetics, Mechanisms and Catalysis 2015;116:19-33.

[27] Liu S, Liu H, Jiang H, Xu Y, Zhang H, and Cheng Z. One-step radiosynthesis of (1)(8)F-AlF-NOTA-RGD(2) for tumor angiogenesis PET imaging. Eur J Nucl Med Mol Imaging 2011;38:1732-41.

[28] Eppard E, Pèrez-Malo M, and Rösch F. Improved radiolabeling of DOTATOC with trivalent radiometals for clinical application by addition of ethanol. EJNMMI Radiopharmacy and Chemistry 2016;1:6.

[29] Idrissi A and Longelin S. The study of aqueous isopropanol solutions at various concentrations: low frequency Raman spectroscopy and molecular dynamics simulations. Journal of Molecular Structure 2003;651-653:271-5.

[30] Hem JD. Aluminum Species in Water. Trace Inorganics In Water: AMERICAN CHEMICAL SOCIETY; 1968, p. 98-114.

[31] Shetty D, Choi SY, Jeong JM, Lee JY, Hoigebazar L, Lee Y-S, *et al*. Stable aluminium fluoride chelates with triazacyclononane derivatives proved by X-ray crystallography and 18F-labeling study. Chemical Communications 2011;47:9732-4.

[32] Cleeren F, Lecina J, Billaud EM, Ahamed M, Verbruggen A, and Bormans GM. New Chelators for Low Temperature Al(18)F-Labeling of Biomolecules. Bioconjug Chem 2016;27:790-8.

[33] Hiroki A, Pimblott SM, and LaVerne JA. Hydrogen Peroxide Production in the Radiolysis of Water with High Radical Scavenger Concentrations. The Journal of Physical Chemistry A 2002;106:9352-8.

[34] Gregory NL. Mechanism of radioprotection by vitamin C. Br J Radiol 1978;51:473-5.

[35] Liu S and Edwards DS. Stabilization of (90)y-labeled DOTA-biomolecule conjugates using gentisic acid and ascorbic acid. Bioconjug Chem 2001;12:554-8.

[36] McBride WJ, D'Souza CA, Karacay H, Sharkey RM, and Goldenberg DM. New lyophilized kit for rapid radiofluorination of peptides. Bioconjug Chem 2012;23:538-47.

[37] Dupuis J, Harel F, Fu Y, Nguyen QT, Letourneau M, Prefontaine A, *et al*. Molecular imaging of monocrotaline-induced pulmonary vascular disease with radiolabeled linear adrenomedullin. J Nucl Med 2009;50:1110-5.

Appendix A. Supplementary data

Al^{18}F-complexation of DFH17, a NOTA-conjugated adrenomedullin analog, for PET imaging of pulmonary circulation

Luis Michel Alonso Martinez[1,2,3], François Harel[2,3,4], Quang T. Nguyen[3], Myriam Létourneau[5], Caroline D'Oliviera-Sousa[3], Bernard Meloche[3], Vincent Finnerty[c], Alain Fournier[5], Jocelyn Dupuis[3,6], Jean N. DaSilva[*,1,2,4]

Table of Contents

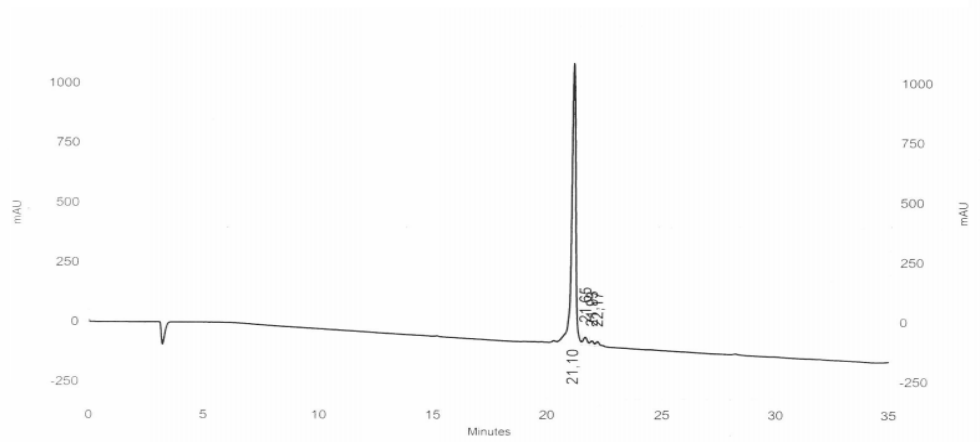

Results

Pk #	Retention Time	Area	Area Percent
1	21,10	14724215,00	94,24
2	21,65	430484,00	2,76
3	21,93	210738,00	1,35
4	22,17	258237,00	1,65
Totals		15623674,00	100,00

a

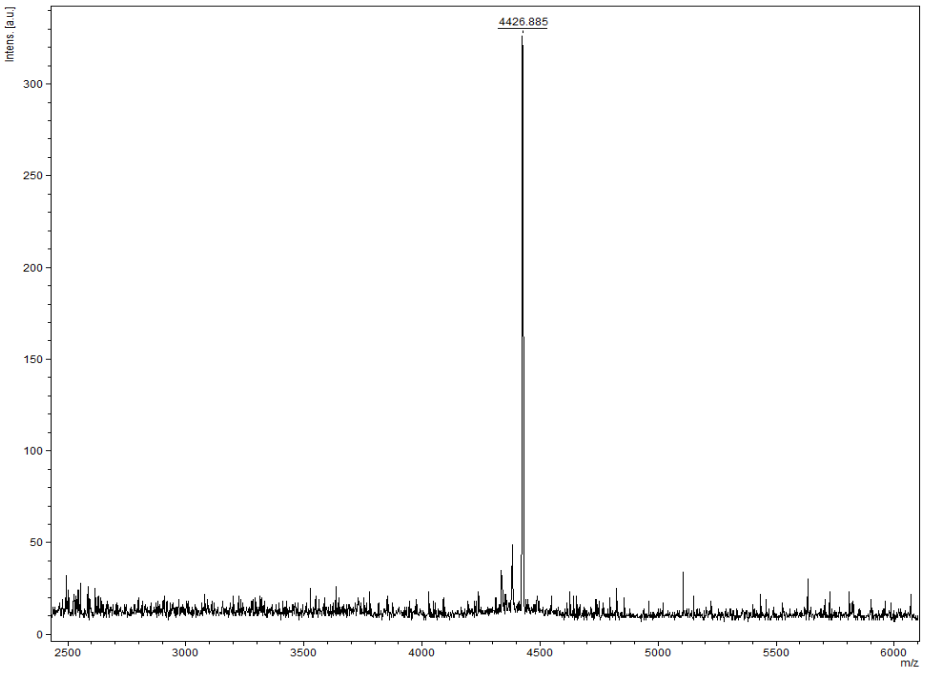

b

Figure S1. Analytical characterization of DFH17 (**a**) RP-HPLC and (**b**) MALDI-TOF.

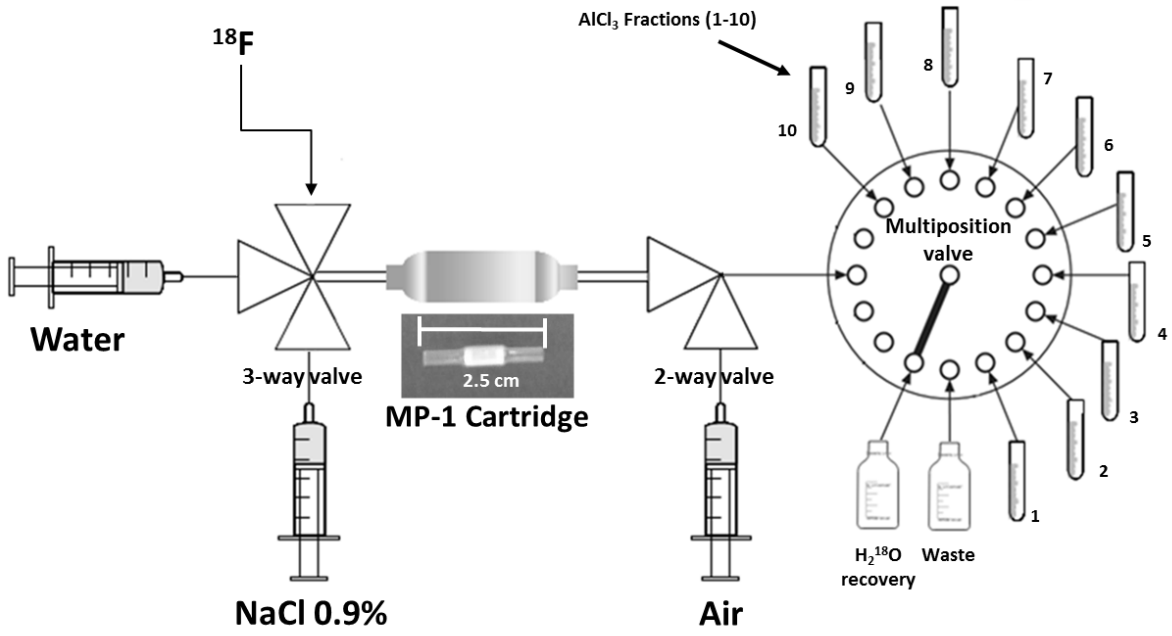

Figure S2. Semi-automatic system for ^{18}F-purification and production of concentrated [^{18}F]AlF. Fluorine-18 is trapped onto a MP-1 cartridge, rinsed with 3 mL water, washed and eluted with 375 µL and 10 µL of 0.9% NaCl respectively and then semi-automatically dispensed (Multiposition valve) into small reactions vials containing 5 µL of 2 mM $AlCl_3$ in sodium acetate buffer (0.1 M, pH 4). The solutions are incubated at RT for 10 min to form [^{18}F]$(AlF)^{2+}$.

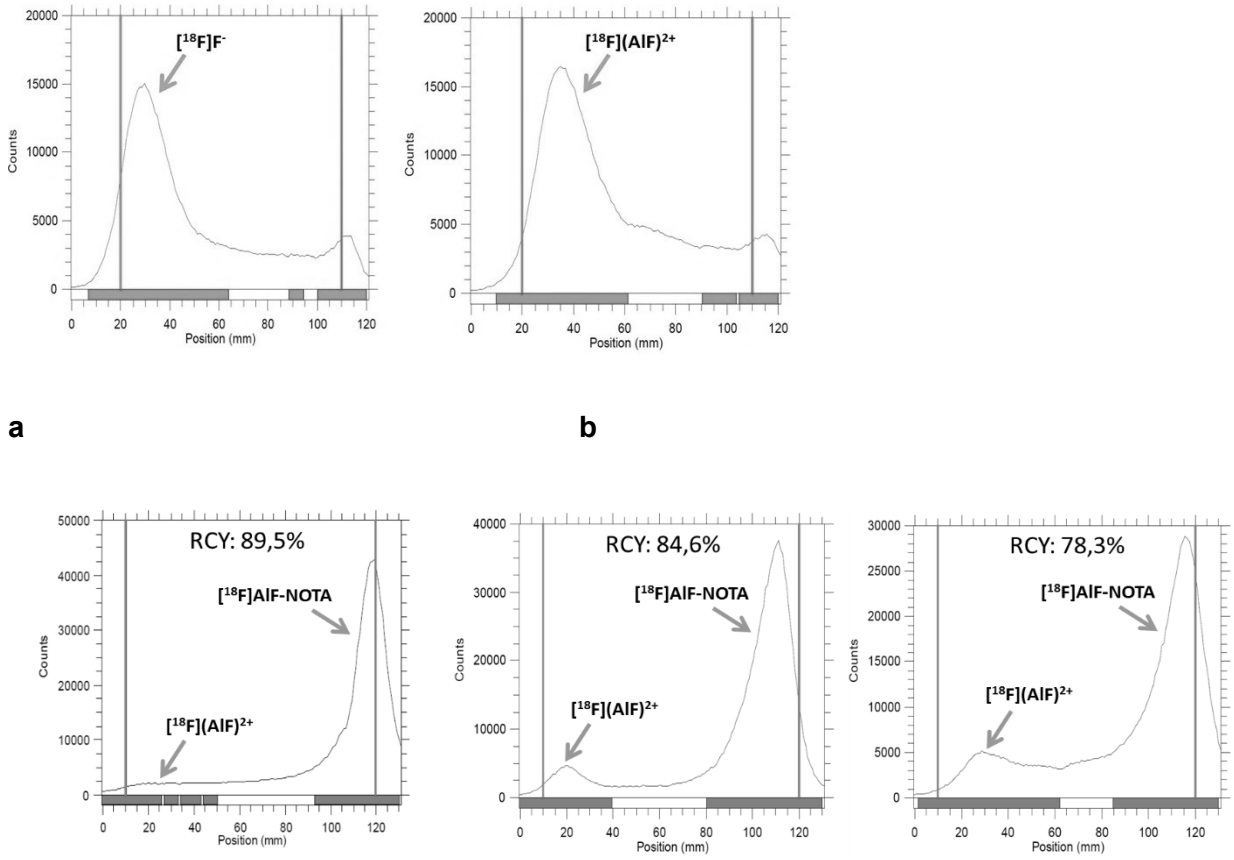

Figure S3. Radio ITLC-SG in citric acid pH 1.6 of **(a)** [^{18}F]F^- and **(b)** [^{18}F]AlF as control. Down panel, [^{18}F](AlF)$^{2+}$-to-NOTA molar ratios **(c)** 1:1, **(d)** 1:3 and **(e)** 1:5.

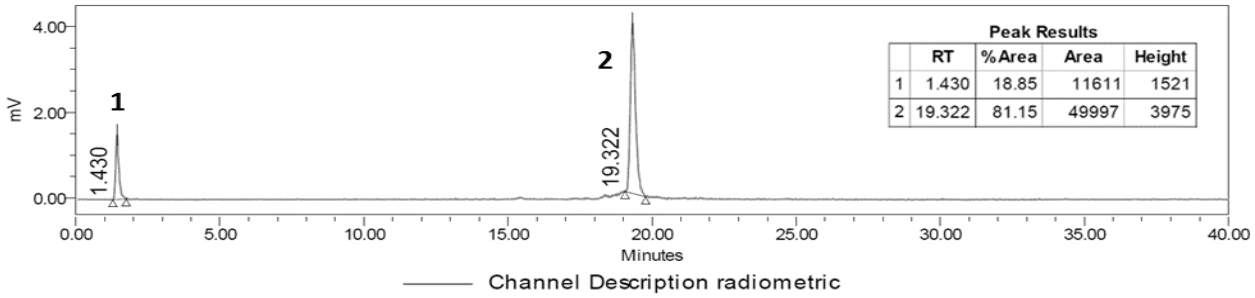

a

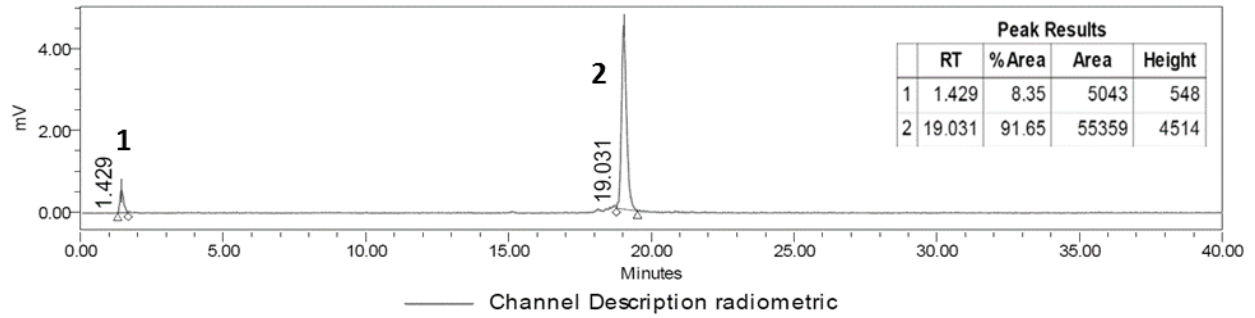

b

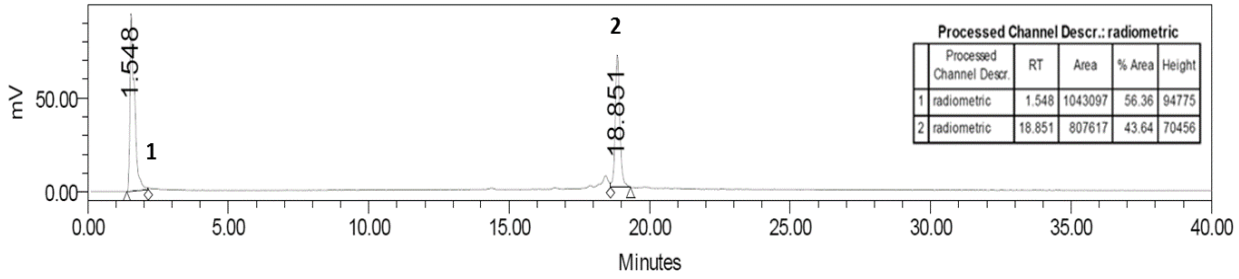

c

Figure S4. HPLC chromatograms of crude reaction mixture of [^{18}F]AlF-DFH17 molar ratio 1:3 (Al^{18}F)$^{2+}$:DFH17. (**a**) Radiosynthesis in aqueous solution (~37 MBq of [^{18}F](AlF)$^{2+}$). (**b**) Radiosynthesis with ethanol 50% (v/v) (~37 MBq of [^{18}F](AlF)$^{2+}$). (**c**) Radiosynthesis with ethanol 50% (v/v) (~1480 MBq of (Al^{18}F)$^{2+}$). *Note:* 1 represents the unbound activity [^{18}F](AlF)$^{2+}$ and 2 the radiolabeled peptide [^{18}F]AlF-DFH17.

Table S1 Results of quality control for the final formulation of [^{18}F]AlF-DFH17 (Representative batch)

Parameter	Acceptance criteria	Result	Decision
Appearance	Colourless, clear, and free from particulate matter	Verified	Pass
pH	4-8	5.3	Pass
Radiochemical purity (HPLC)	≥91%	99%	Pass
Radiochemical purity (ITLC-SG)	≥91%	98%	Pass
Radionuclide identification/Radionuclidic purity	Photo peak energy of 511 keV Half-life 105-115 min No gamma emission other than at 511 and 1022 keV	Confirmed 108.6 min Confirmed	Pass
Organic residual solvent: ethanol (GC)	≤10% (v/v)	0.24%	Pass
Sterility (Filter integrity)	≥60 psi	Pass	Pass

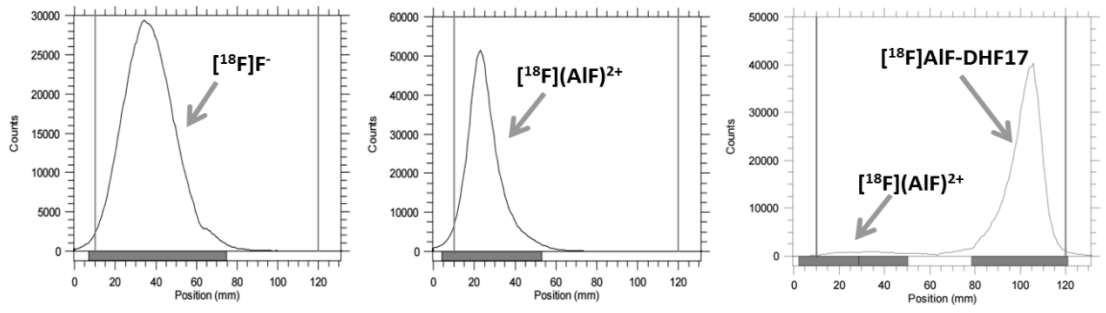

a b c

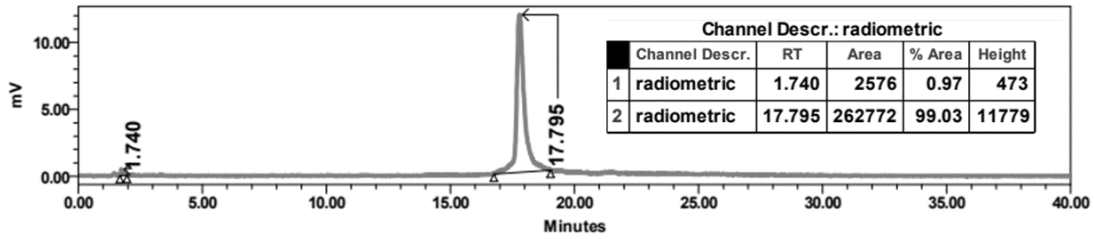

d

Figure S5 Radiochemical purity of [^{18}F]AlF-DFH17 determined by radio ITLC-SG **(a)** [^{18}F]F^- and **(b)** [^{18}F] $(AlF)^{2+}$ as control. **(c)** and **(d)** [^{18}F]AlF-DFH17 by ITLC-SG and RP-HPLC respectively.

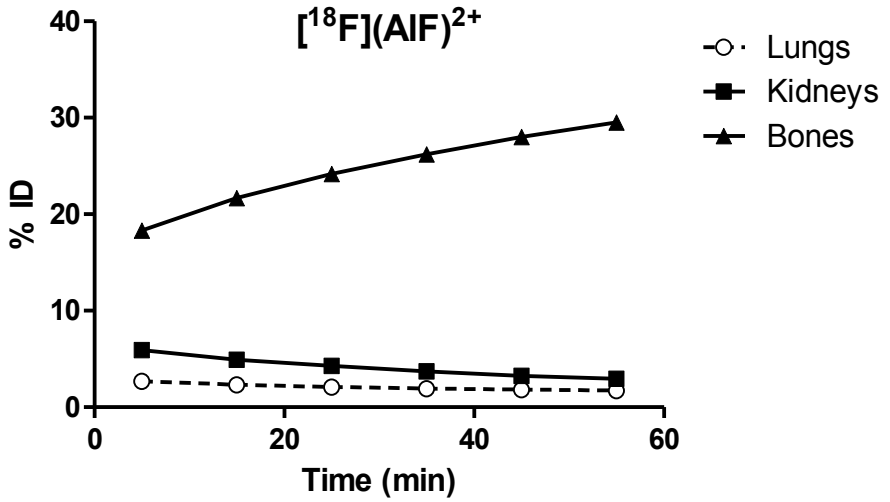

a

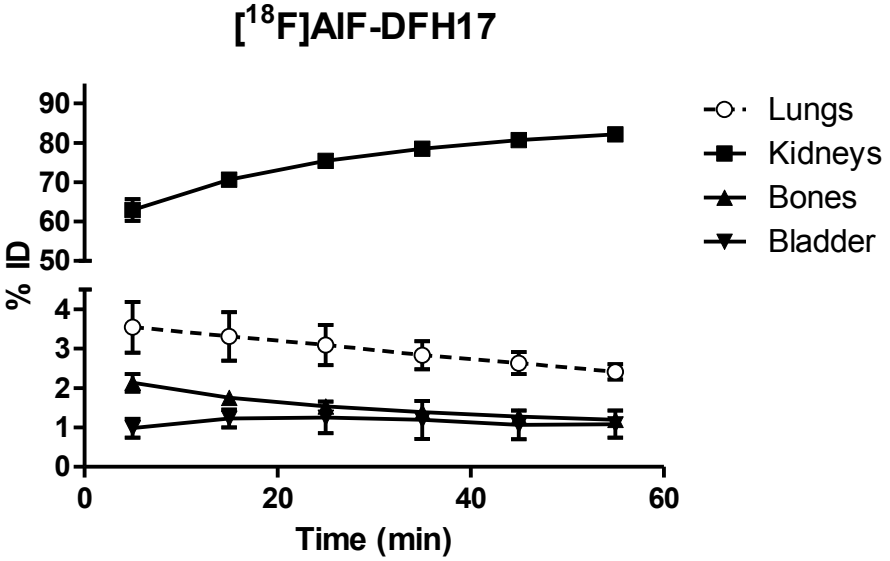

b

Figure S6. Biodistribution in organs of interest of (**a**) free $[^{18}F](AlF)^{2+}$ and (**b**) $[^{18}F]$AlF-DFH17.

Chapter 4: Development of a novel [^{18}F]fluorobenzyl derivative of the AT_1 Receptor antagonist Candesartan

Luis Michel Alonso Martinez[1,2,3], Jean N. DaSilva[*,1,2,4]

[1] University of Montreal Hospital Research Centre, 900 rue Saint-Denis, Montréal (Québec) H2X 3H8, Canada

[2] Department of Biomedical Engineering, Faculty of Medicine, Université de Montréal, Pavillon Paul-G. Desmarais, 2960 chemin de la Tour, Montréal (Québec) H3T 1J4, Canada

[3] Research Center of the Montreal Heart Institute, 5000 Rue Bélanger, Montréal (Québec) H1T 1C8, Canada

[4] Department of Radiology, Radio-oncology and Nuclear Medicine, Université de Montréal, Pavillon Roger-Gaudry, 2900 boulevard Edouard Montpetit, Montréal (Québec) H3T 1J4, Canada

Submitted to Journal of Labelled Compounds and Radiopharmaceuticals

4.1 Abstract

[^{18}F]Fluorobenzyl-Candesartan was developed from 4-[^{18}F]fluoroiodobenzene ([^{18}F]FIB) that was conjugated with alkyne-trityl-candesartan with the assistance of a $Pd(PPh3)_4$/CuI catalyst using the challenging Sonogashira cross-coupling reaction followed by acid deprotection. The 3-step two-reactor 2-HPLC purification process was automated resulting in >90% pure [^{18}F]fluorobenzyl-Candesartan ([^{18}F]**7)** in a RCY of 4.6±1.1% (n=4, decay corrected from EOB) and molar activities of 1406-5513 GBq/mmol. [^{18}F]FIB was reproducibly obtained by direct radiofluorination of the mono-iodinated triphenylsulfonium salt in a ~30% yield (n=8, decay-corrected). [^{18}F]**7** was stable (>97%) up to 4 h in solution and up to 1 h in rat plasma at 37 ^{o}C.

Keywords

[^{18}]FIB prosthetic group, Sonogashira cross-coupling reaction, Pd-catalyzed reaction, PET imaging, Automated synthesis

4.2 Introduction

The renin-angiotensin system (RAS) is part of the regulatory system of cardiovascular and renal functions [1]. Alterations of RAS is characterized by potent anti-atherosclerotic effects, which are mediated by their antihypertensive, anti-inflammatory, antiproliferative, and oxidative stress lowering properties [2]. Among other participants in RAS regulation, angiotensin (Ang) II plays a central role in the regulation of blood pressure. It acts mainly by stimulating the Ang II Type 1 receptors (AT_1Rs) which are expressed in the kidneys, adrenal glands, heart, brain, and vasculature [3]. Alterations of the expression levels of AT_1R has been linked to cardiac and renal diseases, such as cardiac and renal failures, hypertension and some type of cancers [4, 5]. Inhibitors of RAS such as the angiotensin converting enzyme inhibitors and AT_1R blockers, are well-stablished treatments for hypertensive target organ damage, and progressive renal and cardiac diseases [2]

Candesartan is an antagonist that binds selectively to AT_1Rs, giving a long-lasting blockage and suppression of Ang II response. It has high binding affinity (IC_{50} 0.6 nM) compared to the selective AT_1R antagonist Losartan (IC_{50} 20 nM) and Valsartan (IC_{50} 2.7 nM) [6]. Candesartan labeled with ^{125}I at the 22-position of the biphenyl moiety displayed binding to cardiac AT_1Rs with high heart-to-liver ratios, demonstrating its suitability to study AT_1R alterations in cardiovascular disorders [7]. Structure-activity relationship (SAR) studies demonstrated that large prosthetic molecules can be introduced at the 7-position of the benzimidazole ring of candesartan without changing its binding properties and pharmacological functions [8]. We have previously radiolabeled Candesartan with carbon-11 by [^{11}C]methylation of the carboxylic acid group, and this radioligand displayed potential for PET imaging of AT_1Rs [9]. However, a high proportion of the microPET signal in the rat kidney corresponded to non-specific binding from a ^{11}C-labeled hydrophobic metabolite.

We hypothesized that an F-18 aromatic-substituted derivative at the same 7-position would likely provide a more stable radioactive derivative of the high affinity Candesartan for PET imaging. Furthermore, the longer half-life of a F-18 analog of Candesartan would offer some key advantages such as allowing multiple injections per formulation and shipping to sites without cyclotron or radiochemistry capability; as well as superior PET imaging resolution due to low positron energy. Incorporation of ^{18}F-labeled prosthetic groups onto biological active compound has been accomplished via acylation, amidation, imidation, alkylation and photochemical conjugation [10]. Recently, our group developed the novel tracer [^{18}F]fluoropyridine-Candesartan labeled with the [^{18}F]FPyKYNE prosthetic via the copper-catalyzed azide-alkyne cycloaddition at the imidazole 7-position in 10% yield, high molar activity and radiochemical purity (≥97%) [11]. Biological studies revealed specific binding of [^{18}F]fluoropyridine-Candesartan in AT_1R-rich tissues such as the kidney cortex. Further studies to assess the full potential of [^{18}F]fluoropyridine-Candesartan are currently underway.

Several chemical approaches using the Pd mediated cross-coupling reaction were previously investigated in radiochemistry with some favorable outcomes using the Stille [12, 13], Suzuki [14], Sonogashira [15, 16] and Buchard *N*-arylation reactions [17]. Particularly, the Sonogashira cross-coupling reaction approach was successfully utilized to label alkyne-modified peptides with 4-[^{18}F]fluorohalobenzenes, such as 4-[^{18}F]bromofluorobenzene or 4-[^{18}F]fluoroiodobenzene, in high yields and *in vivo* stability [18]. Recently, 4-[^{18}F]fluoroiodobezene ([^{18}F]FIB) was produced from a commercially available precursor in high yields, relatively facile purification, fast conjugation and versatile applications [19]. We report here the radiosynthesis and automation of the novel derivative [^{18}F]fluorobenzyl-Candesartan via the Sonogashira cross-coupling reaction with [^{18}F]FIB (**Scheme 1**), and *in vitro* plasma stability study to assess enzymatic breakdown.

4.3 Material and methods

4.3.1. General

All chemicals, including FIB (**6**) and its triphenylsulfonium triflate precursor (**8**), are commercially available and used without further purification unless stated. Flash chromatography is carried out with silica gel (40-60 μm). ^{1}H- and^{13}C- NMR spectra are acquired with a Bruker 300 MHz spectrometer at ambient temperature. Spectral data are reported in parts per million (ppm) using residual solvent as a reference. High resolution and accurate mass measurements are acquired in positive mode by flow injection analysis into a Thermo Scientific Q-Exactive Plus Orbitrap Mass Spectrometer (San Jose, CA, USA) interfaced with a heated electrospray ion source. Sep-Pak C18 plus (360 mg, Waters) solid-phase extraction cartridges were pre-conditioned with 10 mL ethanol followed by 20 mL water. Analytical HPLC was performed on a Phenomenex Luna C18 (2) column (250×4.6 mm, 10μm) with a Waters HPLC composed of 1515 isocratic pump, 2487 dual λ absorbance detector and a Raytest Gabi Star radioactivity detector. Two analytical methods were utilized: Method 1 (2 mL/min, A: water and B: CH_3CN, linear gradient 50% B to 80% during 25 min); and Method 2 (2 mL/min, 55:45 acetonitrile/water 0.1% TFA). Radio-TLC chromatograms (solvent system, EtOAc/Hexanes/MeOH 80:20:5) were acquired with an AR-2000 radio-TLC imaging scanner (Eckert & Ziegler, Germany). Automated radiosyntheses were performed with the Synthra® RNPlus Research (Germany) synthesis module. Semi-preparative HPLC separations were carried out within the radiosynthesizer with a Phenomenex Luna C18 (2) HPLC column (250×10 mm, 10μm) at a flow rate of 8 mL/min (First purification [^{18}F]**6**: 55:45 acetonitrile/water 0.1% TFA and second purification [^{18}F]**7**: 45:55 acetonitrile/water 0.1% TFA) with UV (254 nm) and radiation detection.

4.3.2 Chemistry

Compounds (**2**),(**3**) and (**4**) were synthesized as reported previously [20]. (See supporting information S1)

*4.3.2.1 Tetrazole-protected alkyne Candesartan (7-((but-3-yn-1-yloxy)methyl)-2-ethoxy-1-((2'-(1-trityl-1H-tetrazol-5-yl)-[1,1'-biphenyl]-4-yl)methyl)-1H-benzo[d]imidazole) (**5**)*

But-3-yn-1-ol (12 mg, 0.18 mmol) was slowly added dropwise to NaH (9.5 mg, 0.39 mmol) and $Bu_4N^+I^-$ (13.2 mg, 0.04 mmol) in 1 mL anhydrous THF under nitrogen and stirred for 1h at 0 ^oC. Tetrazole-protected bromide Candesartan (**4**) (0.158g, 0.20 mmol) in 2 mL anhydrous THF was added dropwise at 0 ^oC and stirring continued overnight under N_2. The reaction was then quenched with cold saturated NaCl and then extracted with ethyl acetate (3 x 20 mL), dried over $MgSO_4$ and the filtrated was partially evaporated under reduced pression. The residue was purified by column chromatography using a solvent gradient EtOAc/Hexanes (15:85 to 30:70). The tetrazole-protected alkyne Candesartan (**5**) was obtained in 55% (yellowish solid, 84 mg). Purity of 98.2% (HPLC, 2mL/min, AcN/0.1M Ammonium formate 80:20). Melting Point: 94-98 ^oC. ESI-MS: Calculated for $C_{47}H_{40}N_6O_2$: 720.3213 Found (MH^+): 721.3288. ^1H NMR ($CDCl_3$): δ: 7.95-6.84 (m, 26H); 5.45 (s, 2H); 4.60 (q, *J*=6.96 Hz, 2H); 4.32 (s, 2H); 3.55-3.45 (m, 2H); 2.42 (td, *J*= 6.58, 2.63 Hz, 2H); 1.99 (m, 1H) 1.45 (t, *J*= 7.05 Hz, 3H). ^{13}C NMR (75 MHz, $CDCl_3$): δ 164.0, 157.6, 141.7, 141.3, 141.4, 140.3, 137.3, 132.5, 130.3, 130.2, 129.9, 129.8, 128.2, 127.5, 126.3, 124.9, 124.2, 121.2, 119.6, 118.4, 82.9, 81.6, 70.7, 69.4, 67.3, 66.4, 45.8, 19.8, 14.7.

*4.3.2.2 Fluorobenzyl-Candesartan (1-((2'-(1H-tetrazol-5-yl)-[1,1'-biphenyl]-4-yl)methyl)-2-ethoxy-7-(((4-(4-fluorophenyl)but-3-yn-1-yl)oxy)methyl)-1H-benzo[d]imidazole) (**7**)*

The tetrazole-protected alkyne Candesartan (**5**) (20 mg, 0.03 mmol) was added under argon to a solution containing $Pd(PPh_3)_4$ (0.70 mg, 0.6 µmol) and CuI (0.11 mg, 0.6 µmol) in 0.2 mL Et_3N at 0 ^oC. After stirring for 10 min under argon, FIB (**6**) (7.4 mg, 0.33 mmol) previously dissolved in Et_3N (0.5 mL) was added dropwise and stirred at 0 ^0C to room temperature for 20 h. After TLC testing (EtOAc/Hexanes 30:70, Rf = 0.4) for completion, the mixture was quenched with saturated aqueous solution of NH_4Cl, extracted with ether (2x10 mL) and washed with water (1x10 mL). A small aliquot was taken for MS. ESI-MS: Calculated for $C_{53}H_{43}FN_6O_2$: 814.3432 Found (MH^+): 815.3513. Subsequently, the product was hydrolyzed with 0.250 mL of TFA/AcN (1:1.5) at 60 ^oC for 7 min. The final mixture was purified by Semi-Prep HPLC and the collected fractions were lyophilized (FreeZone 12-84C, Labconco). The Fluorobenzyl-Candesartan (**7**) was obtained in 31% (white solid, 5 mg) and a chemical purity of 98.9% (analytical HPLC using Method 2). ESI-MS: Calculated for $C_{34}H_{29}FN_6O_2$: 572.2336 Found (MH^+): 573.2432. ^1H NMR ($CDCl_3$) δ 8.04 (d, *J*=6.6 Hz, 1H), 7.68-7.54 (m, 2H), 7.32-7.28 (m, 5H), 7.06 – 6.78 (m, 8H), 5.53 (s, 2H), 4.24 (s, 2H), 4.05 (s, 1H), 3.49 (t, *J*=6.5 Hz, 2H), 2.58 (t, *J*=6.4 Hz, 2H), 0.92 (t, *J*= 6.05 Hz, 3H). ^{13}C NMR (151 MHz, CD_3CN): δ 162.98, 161.34, 157.35, 154.95, 141.29, 139.64, 138.79, 138.53, 138.19, 138.07, 133.47, 131.22, 130.70, 130.67, 130.65, 130.63, 129.65, 127.97, 125.44, 124.22, 123.32, 121.50, 115.60, 109.56, 87.69, 79.83, 79.80, 69.94, 67.67, 67.23, 46.34, 45.58, 44.19, 20.25, 13.84, 8.03.

4.3.3 Radiochemistry

*4.3.3.1 Synthesis of 4-[^{18}F]fluoroiodobenzene ([^{18}F]FIB) ([^{18}F]**6**)*

[^{18}F]FIB ([^{18}F]**6**) was synthesized by ^{18}F-radiofluorination of 4-(iodophenyl)diphenyl-sulfonium triflate (**8**) as reported previously [21], [19]. Briefly, n.c.a. ^{18}F (740-5550 MBq) was produced via an IBA Cyclone 18/9 cyclotron by the nuclear reaction ^{18}O(p,n)^{18}F. The ^{18}F was trapped into an anion exchange resin (QMA light, Waters), eluted with 1.5 mL Kryptofix2.2.2/K_2CO_3 (86:14), and then dried azeotropically with 0.4 mL CH_3CN. When the solution was completely dried, 7 mg of the triphenylsulfonium triflate precursor (**8**) in CH_3CN (0.25 mL) was added to the reactor 1 of the automated Synthra synthesis module. As part of the reaction optimization, various parameters such as the reaction solvent (CH_3CN, DMSO and diglyme), phase-transfer catalyst (K222, $TBAHCO_3$ and no catalyst), amount of precursor (7, 10 and 15 mg), and temperature (85, 90 and 120 ^{o}C) were studied as presented in the **Table 1**. After reaction completion, the crude mixture was quenched with 20 mL water and purified either via a C18 Sep-Pak plus (Waters) or semi-Prep HPLC. [^{18}F]**6** was eluted with 1 mL (either THF or DMF) into either a vial for manual optimization of the Sonogashira cross-coupling reaction (see section 2.3.2) or into the second reactor of the Synthra module for the automated production of [^{18}F]**7** (see section 2.3.3). The radiochemical purity of [^{18}F]**6** was analysed by analytical HPLC (Method1).

*4.3.3.2 Optimization of the synthesis of [^{18}F]fluorobenzyl-Candesartan ([^{18}F]**7**)*

Optimization of the Sonogashira cross-coupling conditions were initially evaluated with two different catalyst ($Pd(PPh_3)_4$ or $Pd(OAc)_2$) for producing other radioligands [15, 16]. Such conditions (**Table 2**, entries 3 and 7) were utilised here for combining [^{18}F]FIB to the alkyne-Candesartan precursor. In general, in a conical vial (3 mL) under argon, the alkyne precursor (**5**), CuI, palladium catalyst and the base were mixed with 29.6-148 MBq of [^{18}F]FIB [^{18}F]**6** (purified by

Sep-Pak C18, entries 1-6 and 9 or semi-Prep HPLC (**Table 2**, entries 7,8 and 10,). The vial was sealed and the reaction heated. After cooling, the deprotection of the tetrazole was carried out by means of 250 µL 40% TFA in CH_3CN at 70 ^oC for 8 min to obtain [^{18}F]**7.** As part of the optimization process, the influence of various reaction parameter such as the amount of precursor (0.75 - 3 mg), temperature (60 - 110 ^oC) and the base (TEA or K_2CO_3) were studied as presented in **Table 2**. Aliquots were taken for radio-HPLC (Method 2) or radio TLC analysis.

*4.3.3.3 Automation of the synthesis of [^{18}F]fluoroenzyl-Candesartan ([^{18}F]**7**)*

Automated synthesis of [^{18}F]**7** was carried out using the best conditions obtained in the optimization process for the production of [^{18}F]**6** (**Table 1**, entry 9) and coupling to the alkyne Candesartan precursor (**5**) (**Table 2**, entry 10) using the automated dual reactor, two HPLC Synthra synthesis module (RNplus Research). After elution from the QMA into reactor 1 with a solution of 86% K2.2.2/K_2CO_3 (A1, 1.5 mL), F-18 was dried azeotropically under vacuum in presence of CH_3CN (A2, 0.4 mL). When completely dried, 10 mg of the precursor (**8**) in diglyme (A3, 0.25 mL) was added and heated at 90 ^oC for 15 min. The reaction was quenched with water (A4, 5 mL) and transferred to a C18 Sep-Pak plus. The cartridge was washed with extra water (A5, 15 mL) and the product was eluted with THF (A6, 1.5 mL) into the V-Vial 1 (containing 7 mL of water). The mixture was purified by semi-prep C18 HPLC (t_R=10.8 min) (See supporting information S3, **Figure S3-1**). The peak corresponding to [^{18}F]**6** was collected into the SP1 vessel (prefilled with 30 mL water), then transferred and trapped on a C18 Sep-Pak plus. [^{18}F]**6** was eluted with DMF (B3, 1 mL) into the reactor 2 containing 3 mg K_2CO_3, 1 mg CuI and 8 mg $Pd(PhP_3)_4$. After addition of the alkyne precursor (**5**) (3 mg in 0.2 mL DMF, B1) to reactor 2 the reaction was heated at 110 ^oC for 20 min. TFA (30%) in acetonitrile (B2, 0.25 mL) was added to the cooled reaction mixture for the tetrazol deprotection (60 ^oC, 7 min).

Following quenching with 3 mL HPLC solvent and filtration (0.45 µm Nylon, Whatman) into the V-vial 2, the filtered mixture was purified by Semi-Prep C18 HPLC (t_R=7.2 min) (See supporting information S3, **Figure S3-1**). The peak corresponding to [^{18}F]**7** was collected into the SP2 vessel (prefilled with 45 mL 0.1% TFA water). [^{18}F]**7** was trapped onto a C18 Sep-Pak plus, eluted with 2 mL ethanol (95%). In order to have a more concentrated formulation, the ethanol was evaporated at 40 ^{o}C under a gentle stream of nitrogen and 0.9% saline (containing 10 mg/mL sodium ascorbate, [22]) was added to reach a maximum of 10% ethanol in the final formulation.

4.3.3.4 Analytical studies

The final formulation was analysed by analytical HPLC (Method 2, t_R=7.8 min, **Figure 1**) to determine the radiochemical purity and molar activity. The chemical identity of product [^{18}F]**7** was confirmed by co-injection with the nonradioactive standard (**7**). [^{18}F]Fluorobenzyl-Candesartan ([^{18}F]**7**) was assayed for stability by monitoring the radiochemical purity 4 h after EOS.

4.3.3.5 In vitro plasma stability

In vitro tracer stability was evaluated in plasma samples from Sprague-Dawley rats. Plasma volumes of 0.5 mL were mixed with [^{18}F]**7** (~1.62 kBq) and then incubated at 37 ^{o}C for 20, 40- and 60-min. Urea at final concentration of 0.35 g/mL was added to plasma samples to disrupt plasma protein binding. Prior to the experiments, samples of plasma directly spiked with authentic tracer before incubation at time zero (no enzymatic degradation) was processed as a control.

A previously described column-switch HPLC [23] consisted in a capture column (20x2 mm, hand packed with Oasis HLB) and analytical column (Luna C18 10 µm 100 Å 250x4.60 mm,

Phenomenex) was utilised to study the presence of plasma degradation products. Briefly [adapted from 23], filtered samples injected in the system are trapped onto the capture column and hydrophilic subproducts and/or macromolecules are eluted at 1 mL/min with 1:99 acetonitrile/water. Once the UV signal returned to baseline, solvent is switched to 55:45 acetonitrile/0.1% TFA to back-flushed the retained compounds (hydrophobic degradation products + intact tracer) off the capture column and over the analytical column at 2 mL/min. Signals were analysed using PeakSimple 3.77 software, and subsequently corrected for noise and radioactive decay. Integration of peaks was used to determine the proportion of hydrophilic/hydrophobic plasma degradation products over intact [^{18}F]**7.**

4.4 Results and discussion

4.4.1 Chemistry

In order to prepare the hydroxy derivative of Candesartan (**2**), the carboxylic acid moiety was reduced by means of lithium aluminium hydride in high yields (**Scheme 1**). The alkyne tetrazole-protected Candesartan (**5**) was prepared from (**2)** with trityl chloride in the presence of TEA and dichloromethane. To produce the alkyne Candesartan precursor (**5**), two synthetic strategies were evaluated. The first one, was to form the alkoxide of the hydroxy derivative of Candesartan (**2**) by means of NaH and then proceed to the ether formation reaction with 4-chlorobut-1-yne. The second strategy was to use the Mitsunobu reaction between of hydroxy derivative of Candesartan (**2**) and 3-butyn-1-ol, but unfortunately both approaches didn't yield the desired compound (**5**). Interestingly, the reaction to produce (**5**) proceeded in high yields by inverting the conditions of first strategy, where the alkoxide of 3-butyn-1-ol reacted with the trityl bromine Candesartan (**4**) following a modified version of Williamson ether synthesis.

4.4.2 Radiochemistry

*4.4.2.1 Synthesis of [^{18}F]FIB ([^{18}F]**6**)*

After several attempts following the conditions reported in Way and Wuest, 2014, the highest RCY of [^{18}F]FIB was of 13.1±2.3% (**Table 1**, entry 1). Further experiments were designed to find optimal conditions (in our hands) and to increase the RCY. As presented in **Table 1**, the use of diglyme (entry 3) yielded ~19% compared to ~6% with anhydrous DMSO (entry 2). Therefore, diglyme was used in all subsequent conditions (entries 4-10). No difference was found with K222 or $TBAHCO_3$ (**Table 1**, entries 3 and 4), while using no catalyst produced [^{18}F]**6** in lower yields (**Table 1**, entry 5). Richarz *et al.* [24] published a minimalist method to produce [^{18}F]FIB in 66% radioconversion (RCC) without the need of catalyst and/or azeotropic drying. In their study, F-18 was trapped in a Chromafix cartridge, rinsed extensively with anhydrous methanol and then eluted into the reactor using the same sulfonium salt precursor as here. Using their approach, [^{18}F]FIB production was lower compared to the use of K222 or $TBAHCO_3$. Furthermore, approximately ~30% of the trapped F-18 was not completely eluted when 10 mg of sulfonium salt precursor was utilised. Therefore we selected the classical K222/K_2CO_3 approach for producing [^{18}F]FIB in high RCY.

After evaluating the amount of precursor (**Table 1**, entries 3, 6 and 7), the highest RCY for producing [^{18}F]**6** (at 93% radiochemical purity) was found with 10 mg of precursor. As previously reported [19], we also found a relationship between the temperature and the radiochemical purity of [^{18}F]**6** (**Table 1**, entries 8, 9 and 10). The formation of the by-product [^{18}F]fluorobenzene was practically prevented with reactions at 90 ^{o}C, indicating that at this temperature (See supporting information S2, **Figure S2-1**) the mechanism favored the electron-

poor iodinated system leading to the desired product [^{18}F]**6** [21]. Finally, the optimal condition (**Table 1**, entry 9) produced [^{18}F]**6** in a similar RCY (31.3±3.8, n=8) as previously reported by [21].

*4.4.2.2 Optimization of the synthesis of [^{18}F]**7***

Since the reaction proposal by Kenkichi Sonogashira in the 1970s [25], the Sonogashira cross-coupling reaction has not been extensively used in radiochemistry. The first report came in 2003 when Wuest and Kniess [15] reported the radiolabeling of an estradiol derivative with [^{18}F]FIB. Twelve years later, the same group extended [^{18}F]FIB application to the radiolabeling of alkyne-modified peptides - under mild conditions with $Pd(OAc)_2$ in high RCYs [18]. Their reported Sonogashira conditions were investigated here for radiolabeling the protected alkyne-Candesartan derivative (**5**) with [^{18}]FIB (**Table 2** , entries 3 and 7). As observed in entry 7, addition of $Pd(OAc)_2$ to the reaction mixture did not produce the final compound [^{18}F]**7** from [^{18}F]**6** either at 85 ^{o}C or 110 ^{o}C (**Table 2**, entry 7 and 6, respectively). Therefore, we decided to use the $Pd(PPh_3)_4$ catalyst in all subsequent experiments.

While performing optimization experiments with 3 mg of precursor and TEA as the base, random conversion yields where obtained varying from no reaction to 22% RCC. The analysis of HPLC chromatograms (**Table 2**, entry 3) revealed the formation of more radioactive impurities and the presence of the unprotected final product. To overcome these problems, we hypothesized that using less precursor would favorize the formation of [^{18}F]**7** over the [^{18}F]by-products (**Table 2**, entries 1 and 2). Contrary to our hypothesis, the formation yield was also reduced to 0.3% with 0.75 mg of precursor (**Table 2**, entry 1). Reducing the reaction temperature to 60 or 90 ^{o}C (**Table**

2, entries 5 or 4, respectively) was not beneficial with no reaction, demonstrating that 110 °C is required for completion of the cross-coupling reaction in higher RCCs.

The acid hydrolysis of the trityl-protected [^{18}F]fluorobenzyl-Candesartan was not reproducible due to the excess of TEA. It was reported that using concentrated acids (eg. TFA or HCl) led to the formation of the des-ethylated Candesartan analog for trityl deprotection [9]. To circumvent this problem, alternative bases such K_2CO_3 and Cs_2CO_3 were explored as previously reported as a modified version of the classic Sonogashira reaction [26]. Adapting this reaction condition to our context, 3 eq of K_2CO_3 in DMF produced [^{18}F]**7** in 5% yield with almost no trityl-protected (**5**) left (**Table 2**, entry 8). In addition, increasing the amount of precursor to 3 mg (**Table 2**, entry 9) increased the RCC up to 8%. Repeating the entry 9 with HPLC pure [^{18}F]**6** (**Table 2**, entry 10) led to the production of [^{18}F]**7** in in higher RCC (22%). Such observation was previously discussed by Wuest and Kniess [15]. Based in their findings, iodinated impurities produced during the thermal decomposition of product (**8**) [27, 28] are not separated from [^{18F}]FIB following C18 SepPak purification, causing competitive cross-coupling reactions reducing the RCC yields. Whereas such competition was not observed with [^{18}F]**6** after HPLC purification. The conditions described in entry 10 were thus selected for automatized radiosynthesis.

*4.4.3 Automation of the synthesis of [^{18}F]**7***

Automation of the radiosynthesis (See supporting information S3, **Figure S3-1**) was initially performed with 1 mg of precursor giving [^{18}F]**7** in an overall RCY of 0.19±0.03% (n=3, decay corrected from EOB). Increasing the amount of precursor to 3 mg of the protected alkyne-candesartan (**5**) gave radiochemically pure (99.8%) [^{18}F]7 in 4.6±1.1% (n=4, decay corrected from EOB) (**Figure 1a**). Its identity was confirmed by co-injection with the authentic (**7**) (**Figure 1b**).

Fawdry [22] reported that 10 mg/mL of sodium ascorbate in concentrated formulations of FDG (11 GBq/mL) led to a stability of 99% up to 14 h. After ethanol evaporation and reformulation in saline containing sodium ascorbate, the final formulation at 1.48 GBq/mL was stable for 4 h after EOS at room temperature (**Figure 1b**)**.** The molar activity of the final formulation was low (1406-5513 GBq/mmol) due to the formation of structurally-close impurities during the coupling and acid hydrolysis as detected by Semi-Prep HPLC (See supporting information S3, **Figure S3-2**). Attempts to further improve the isolated radiochemical yield and molar activities turned out to be challenging. However, new strategies for reducing the side-products formation by exploring new Pd catalyst, less aggressive acid hydrolysis of tetrazole group and new semi-prep HPLC system are currently under way.

4.4.4 In vitro plasma stability

Hydrolysis of compounds by plasmatic enzymes is among a wide variety of mechanisms utilized for clearing drugs from circulation. This process reduces the lifetime of pharmaceutical compounds in circulation, affecting the availability of the parent product to produce pharmacological effect [29]. [^{18}F]**7**was found to be stable in plasma with the presence of less than 3% of radioactive by-products after 60 min of incubation at 37 ^{o}C. Previous reports suggested that compounds containing functional groups such as esters, amides, lactones, lactams, carbamides, sulphonamides, and peptic mimetics are more susceptible to hydrolysis in plasma [30]. Taking our results into account, we have found the alkyne-benzene (sp-sp^2 carbon-carbon) planar arrangement of[^{18}F]**7** to be highly stable to enzymatic break-down, suggesting a stable metabolic profile of [^{18}F]fluorobenzyl-Candesartan.

4.5 Conclusions

A fully automated synthesis of the novel tracer [^{18}F]FB-Candesartan has been developed in a three-steps and two-HPLC purifications using [^{18}F]FIB as prosthetic group. The tracer was obtained in high radiochemical purity and remained stable up to 4 h in solution and up to 1 h in plasma at 37 ^{o}C. Nonetheless, the use of Sonogashira cross-coupling reaction to produce [^{18}F]fluorobenzyl-Candesartan in high yields and molar activities was found to be challenging.

4.6 Acknowledgements

The authors would like to thank the staff of Radiochemistry and Cyclotron Platform and Ms Fleur Gaudette of the Pharmacokinetics core facility for the high-resolution mass measurements. This work was supported by CIHR (MOP-126079) and the Réseau de Bio-Imagerie du Québec.

4.7 References

[1] Reid IA, Morris BJ, and Ganong WF. The renin-angiotensin system. Annu Rev Physiol 1978;40:377-410.

[2] Schmieder RE, Hilgers KF, Schlaich MP, and Schmidt BMW. Renin-angiotensin system and cardiovascular risk. The Lancet 2007;369:1208-19.

[3] De Mello WC. Renin Angiotensin System and the Heart: Wiley,2005.

[4] Du, Feng, Hu, Sun, Sun, Zhao, *et al*. Angiotensin II receptor type 1 blockers suppress the cell proliferation effects of angiotensin II in breast cancer cells by inhibiting AT1R signaling. Oncology Reports 2012;27:1893-903.

[5] Uemura H, Hasumi H, Ishiguro H, Teranishi J-i, Miyoshi Y, and Kubota Y. Renin-angiotensin system is an important factor in hormone refractory prostate cancer. The Prostate 2006;66:822-30.

[6] Burnier M and Brunner HR. Angiotensin II receptor antagonists. The Lancet 2000;355:637-45.

[7] Sanad MH, Sallam KM, Marzook FA, and Abd-Elhaliem SM. Radioiodination and biological evaluation of candesartan as a tracer for cardiovascular disorder detection. Journal of Labelled Compounds and Radiopharmaceuticals 2016;59:484-91.

[8] Kubo K, Kohara Y, Imamiya E, Sugiura Y, Inada Y, Furukawa Y, *et al*. Nonpeptide angiotensin II receptor antagonists. Synthesis and biological activity of benzimidazolecarboxylic acids. J Med Chem 1993;36:2182-95.

[9] Hadizad T, Kirkpatrick SA, Mason S, Burns K, Beanlands RS, and DaSilva JN. Novel O-[11C]methylated derivatives of candesartan as angiotensin II AT1 receptor imaging ligands: Radiosynthesis and ex vivo evaluation in rats. Bioorganic & Medicinal Chemistry 2009;17:7971-7.

[10] Wester H-J, Hamacher K, and Stöcklin G. A comparative study of N.C.A. Fluorine-18 labeling of proteins via acylation and photochemical conjugation. Nuclear Medicine and Biology 1996;23:365-72.

[11] Abreu Diaz AM, Drumeva GO, Petrenyov DR, Carrier J-F, and DaSilva JN. Synthesis of the Novel AT1 Receptor Tracer [18F]Fluoropyridine–Candesartan via Click Chemistry. ACS Omega 2020.

[12] Wüst FR and Kniess T. No-carrier added synthesis of 18F-labelled nucleosides using Stille cross-coupling reactions with 4-[18F]fluoroiodobenzene. Journal of Labelled Compounds and Radiopharmaceuticals 2004;47:457-68.

[13] Wüst FR, Höhne A, and Metz P. Synthesis of 18F-labelled cyclooxygenase-2 (COX-2) inhibitors via Stille reaction with 4-[18F]fluoroiodobenzene as radiotracers for positron emission tomography (PET). Organic & Biomolecular Chemistry 2005;3:503-7.

[14] Steiniger B and Wuest FR. Synthesis of 18F-labelled biphenyls via SUZUKI cross-coupling with 4-[18F]fluoroiodobenzene. Journal of Labelled Compounds and Radiopharmaceuticals 2006;49:817-27.

[15] Wüst FR and Kniess T. Synthesis of 4-[18F]fluoroiodobenzene and its application in sonogashira cross-coupling reactions. Journal of Labelled Compounds and Radiopharmaceuticals 2003;46:699-713.

[16] Way JD, Wang M, Hamann I, Wuest M, and Wuest F. Synthesis and evaluation of 2-amino-5-(4-[18F]fluorophenyl)pent-4-ynoic acid ([18F]FPhPA): A novel 18F-labeled amino acid for oncologic PET imaging. Nuclear Medicine and Biology 2014;41:660-9.

[17] Wüst FR and Kniess T. N-Arylation of indoles with 4-[18F]fluoroiodobenzene: synthesis of 18F-labelled σ2 receptor ligands for positron emission tomography (PET). Journal of Labelled Compounds and Radiopharmaceuticals 2005;48:31-43.

[18] Way JD, Bergman C, and Wuest F. Sonogashira cross-coupling reaction with 4-[18F]fluoroiodobenzene for rapid 18F-labelling of peptides. Chem Commun (Camb) 2015;51:3838-41.

[19] Way JD and Wuest F. Automated radiosynthesis of no-carrier-added 4-[18F]fluoroiodobenzene: a versatile building block in 18F radiochemistry. Journal of Labelled Compounds and Radiopharmaceuticals 2014;57:104-9.

[20] Garvey DS. NITRIC OXIDE ENHANCING ANGIOTENSIN II ANTAGONIST COMPOUNDS, COMPOSITIONS AND METHODS OF USE. USA; 2006.

[21] Mu L, Fischer CR, Holland JP, Becaud J, Schubiger PA, Schibli R, *et al*. 18F-Radiolabeling of Aromatic Compounds Using Triarylsulfonium Salts. European Journal of Organic Chemistry 2012;2012:889-92.

[22] Fawdry RM. Radiolysis of 2-[18F]fluoro-2-deoxy-D-glucose (FDG) and the role of reductant stabilisers. Appl Radiat Isot 2007;65:1193-201.

[23] Hilton J, Yokoi F, Dannals RF, Ravert HT, Szabo Z, and Wong DF. Column-switching HPLC for the analysis of plasma in PET imaging studies. Nuclear Medicine and Biology 2000;27:627-30.

[24] Richarz R, Krapf P, Zarrad F, Urusova EA, Neumaier B, and Zlatopolskiy BD. Neither azeotropic drying, nor base nor other additives: a minimalist approach to (18)F-labeling. Organic & biomolecular chemistry 2014;12:8094-9.

[25] Sonogashira K, Tohda Y, and Hagihara N. A convenient synthesis of acetylenes: catalytic substitutions of acetylenic hydrogen with bromoalkenes, iodoarenes and bromopyridines. Tetrahedron Letters 1975;16:4467-70.

[26] Jiang Q, Li H, Zhang X, Xu B, and Su W. Pd-Catalyzed Decarboxylative Sonogashira Reaction via Decarboxylative Bromination. Organic Letters 2018;20:2424-7.

[27] Knapczyk JW, Wiegand GH, and McEwen WE. Decomposition of triarylsulfonium alkoxides. Tetrahedron Letters 1965;6:2971-7.

[28] Dektar JL and Hacker NP. Photochemistry of triarylsulfonium salts. Journal of the American Chemical Society 1990;112:6004-15.

[29] Copeland RA. Evaluation of Enzyme Inhibitors in Drug Discovery: A Guide for Medicinal Chemists and Pharmacologists: Wiley,2013.

[30] Di L, Kerns EH, Hong Y, and Chen H. Development and application of high throughput plasma stability assay for drug discovery. International journal of pharmaceutics 2005;297:110-9.

Figures

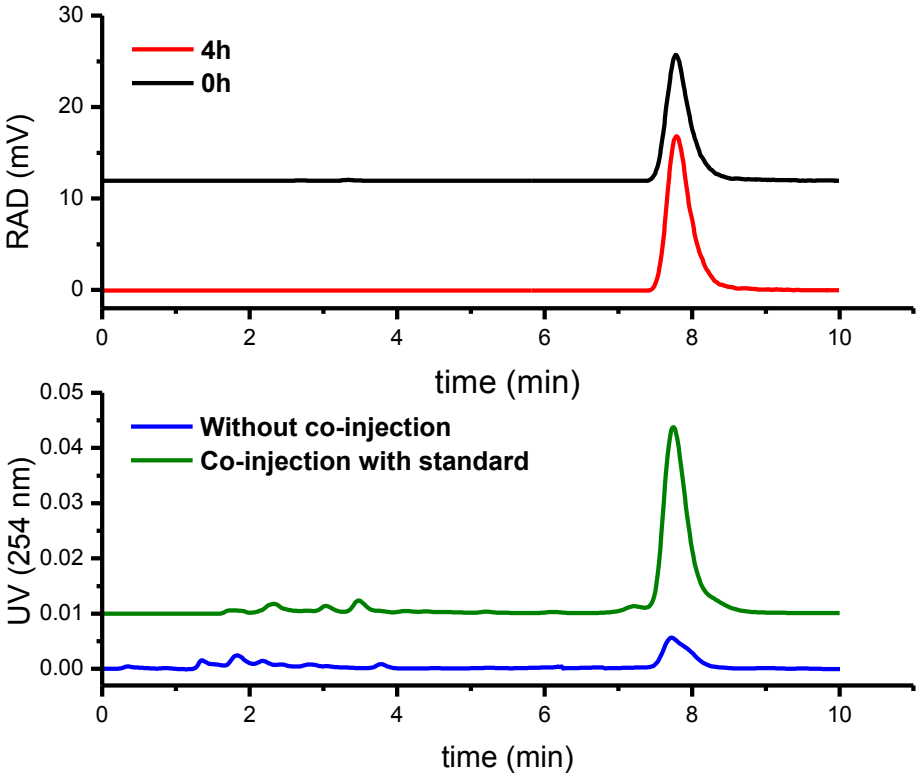

Figure 1. Representative analytical HPLC chromatograms of [^{18}F]**7**. Co-injection with authentic standard (**7**) in green (t_R=7.78 min) (**a**). Radioactive signal at QC time (time 0) in red and 4 h post-synthesis in black (t_R =7.80 min) (**b**).

Schemes

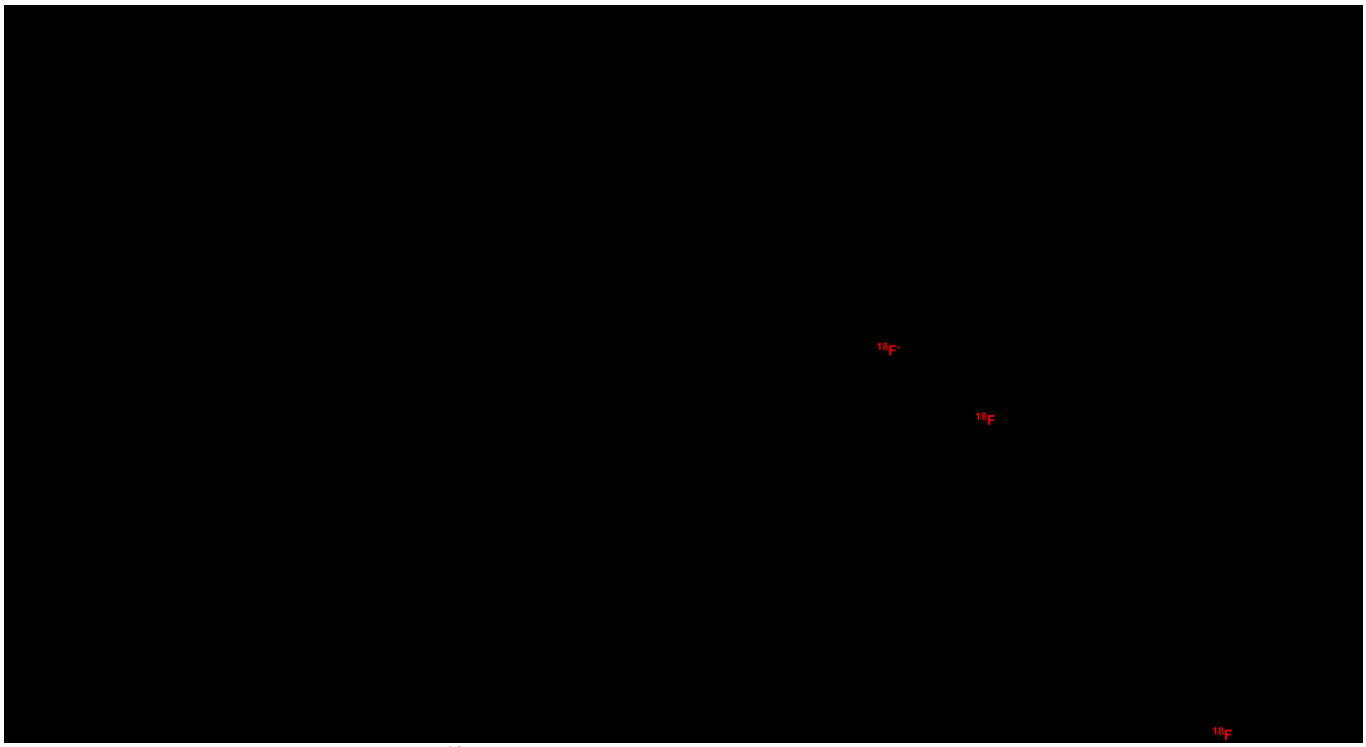

Scheme 1. Synthetic route of [^{18}F]**7**.

Tables

Table 1. Optimization of [^{18}F]**6** reaction conditions

Entry	Phase-transfer catalyst	Precursor (mg)	Solvent	Time (min)	Temperature (ºC)	RCY [b] %
1	K_{222}	7	CH_3CN	15	85	13.1±2.3
2	K_{222}	7	DMSO	15	85	6.2±1.4
3	K_{222}	7	Diglyme	15	85	19.3±2.8
4	$TBAHCO_3$	7	Diglyme	15	85	23.0±1.5
5	None[a]	7	Diglyme	15	85	9.1±1.8
6	K_{222}	10	Diglyme	15	85	31.3±3.8
7	K_{222}	15	Diglyme	15	85	14.4±1.5
8[c]	K_{222}	10	Diglyme	15	85	26.4
9[c]	K_{222}	10	Diglyme	15	90	29.8
10[c]	K_{222}	10	Diglyme	15	120	<20

[a] following Richarz *et al.* [24]
[b] isolated radiochemical yield from start-of-synthesis (n=3)
[c] radiochemical conversion of [^{18}F]FIB compared to [^{18}F]Fluorobenzene (by-product) for conditions described in entry 8, 9 and 10 are 93.1%, 99.8% and 78.3%, respectively (n=1).

Table 2. Optimization of Sonogashira cross-coupling on the synthesis of [^{18}F]**7**

Entry	Product 5 mg/µmol	CuI mg/µmol	Catalyst mg/µmol	Base	Solvent	Volume mL	Temp °C	Time min	RCC[a] %
1[d]	0.75/1	3/16	$Pd(PPh_3)_4$ 3/3	TEA	THF/TEA (1:1)	2	110	20	0.3[b]
2[d]	1.5/2	3/16	$Pd(PPh_3)_4$ 3/3	TEA	THF/TEA (1:1)	2	110	20	4.4[b]
3[d]	3/4	3/16	$Pd(PPh_3)_4$ 3/3	TEA	THF/TEA (1:1)	2	110	20	0-15[b]
4[d]	3/4	3/16	$Pd(PPh_3)_4$ 3/3	TEA	THF/TEA (1:1)	2	90	20	0[c]
5[d]	3/4	3/16	$Pd(PPh_3)_4$ 3/3	TEA	THF/TEA (1:1)	2	60	20	0[c]
6[d]	1.5/2	3/16	$Pd(OAc)_2$ 3/13	TEA	THF/TEA (40:1)	2	110	20	0[b]
7[e]	1/1	1/5	$Pd(OAc)_2$ 3/13	TEA	THF/TEA (40:1)	2	85	30	0[b]
8[e]	1.5/2	1/5	$Pd(PPh_3)_4$ 8/7	K_2CO_3	DMF	1	110	20	5.1[b]
9[d]	3/4	1/5	$Pd(PPh_3)_4$ 8/7	K_2CO_3	DMF	1	110	20	7.8[b]
10[e]	3/4	1/5	$Pd(PPh_3)_4$ 8/7	K_2CO_3	DMF	1	110	20	22[b]

[a] RCC was determined with n=1 run, except for entry 3 (n=6); [b]determined by analytical HPLC; [c]determined by radio-TLC. [d] [^{18}F]**6** purified by Sep-Pak C18, entries 1-6 and 9; [e] [^{18}F]**6** purified by semi-Prep HPLC, entries 7,8 and 10

Supporting information

Development of a novel [^{18}F]fluorobenzyl derivative of the AT_1 Receptor antagonist Candesartan

Luis Michel Alonso Martinez[1,2,3], Jean N. DaSilva[*,1,2,4]

Table of content

*S1. Structural information of compound (**2**), (**3**) and (**4**)*

*Hydroxy Candesartan derivative ((1-((2'-(1H-tetrazol-5-yl)-[1,1'-biphenyl]-4-yl)methyl)-2-ethoxy-1H-benzo[d]imidazol-7-yl)methanol) (**2**)*

The hydroxy Candesartan derivative (**2**) was produced in 90% (white solid, 432 mg). Melting Point: 133-135 ºC. ESI-MS: Calculated for $C_{24}H_{22}N_6O_2$: 426.1804 Found (MH^+): 427.1874. ^{1}H NMR (DMSO-d6): δ 7.66-7.44 (m, 4H), 7.40 (dd, *J*=7.7, 1.3 Hz, 1H), 7.10-7.02 (m, 3H), 7.00 (dd, *J*=7.5, 1.3 Hz, 1H), 6.93 (d, *J*=8.2 Hz, 2H), 5.50 (s, 2H), 4.56 (q, *J*=7.0 Hz, 2H), 4.45 (s, 2H), 1.41 (t, *J*=7.1 Hz, 3H).

*Tetrazole-protected hydroxy Candesartan derivative ((2-ethoxy-1-((2'-(1-trityl-1H-tetrazol-5-yl)-[1,1'-biphenyl]-4-yl)methyl)-1H-benzo[d]imidazol-7-yl)methanol) (**3**)*

The tetrazole-protected hydroxy Candesartan (**3**) was obtained in 60% (white solid, 403 mg). Melting Point: 183-185 ºC. ESI-MS: Calculated for $C_{43}H_{36}N_6O_2$: 668.2900 Found (MH^+): 669.2973. ^{1}H NMR ($CDCl_3$): δ 7.95-7.89 (m, 1H), 7.63 (d, *J*=7.5 Hz, 1H), 7.54-7.42 (m, 2H), 7.40-7.30 (m, 5H), 7.27-7.21 (m, 6H), 7.16 (t, *J*=7.7 Hz, 1H), 7.09 (d, *J*=8.2 Hz, 2H), 6.98-6.91 (m, 7H), 6.85 (d, *J*=8.2 Hz, 2H), 5.48 (s, 2H), 4.65 (q, *J*=7.0 Hz, 2H), 4.44 (s, 2H), 1.41 (t, *J*=7.1 Hz, 3H).

*Tetrazole-protected bromide Candesartan derivative (7-(bromomethyl)-2-ethoxy-1-((2'-(1-trityl-1H-tetrazol-5-yl)-[1,1'-biphenyl]-4-yl)methyl)-1H-benzo[d]imidazole) (**4**)*

The tetrazole-protected bromide Candesartan (**4**) was obtained in 50% (slightly yellow solid, 203 mg). Melting Point: 75-78 ^{o}C. ESI-MS: Calculated for $C_{43}H_{35}BrN_6O$: 730.2056 Found (MH^+): 731.2135. 1H NMR ($CDCl_3$): δ 7.99–7.95 (m, 1H), 7.63 (dd, *J*=7.9, 0.9 Hz, 1H), 7.55-7.42 (m, 2H), 7.40-7.31 (m, 5H), 7.30-7.21 (m, 7H), 7.15 (t, *J*=7.8 Hz, 3H), 6.99-6.86 (m, 10H), 5.54 (s, 2H), 4.69 (q, *J*=7.1 Hz, 2H), 4.28 (s, 2H), 1.45 (t, *J*=7.1 Hz, 3H).

S2. Effect of temperature in the production of [^{18}F]**6**

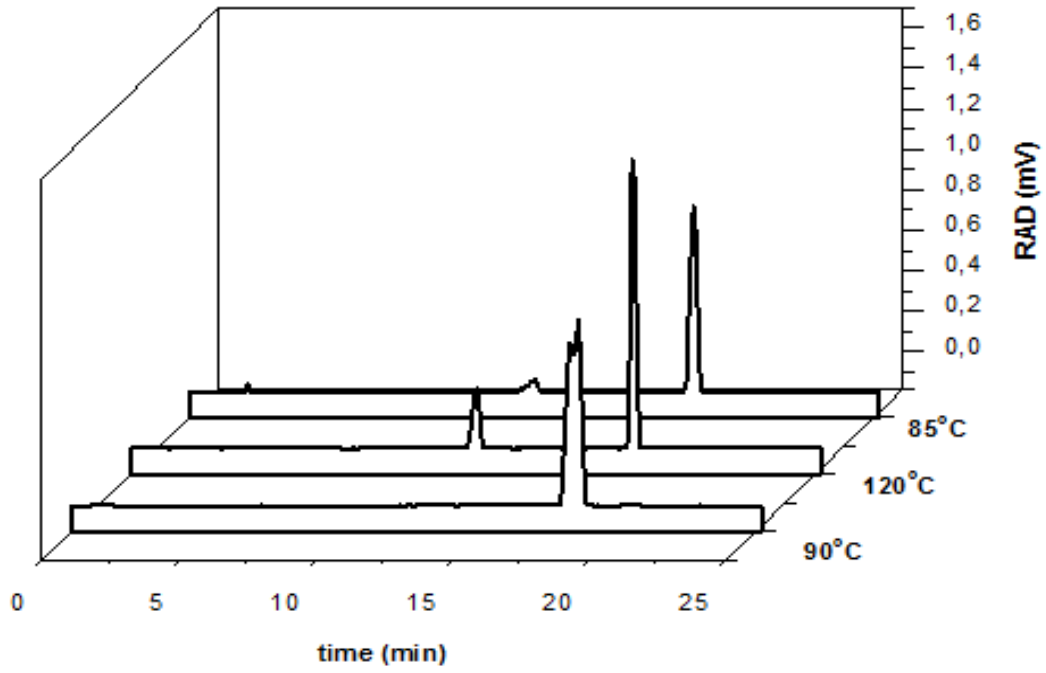

Figure S2-1. Representative analytical HPLC chromatograms of [^{18}F]**6** at different temperatures. (t_R [^{18}F]**6**= 18.4 min and by-product [^{18}F]fluorobenzene, t_R=12.6 min)

*S3 Reaction impurities of [^{18}F]**7** detected by Semi-Prep HPLC*

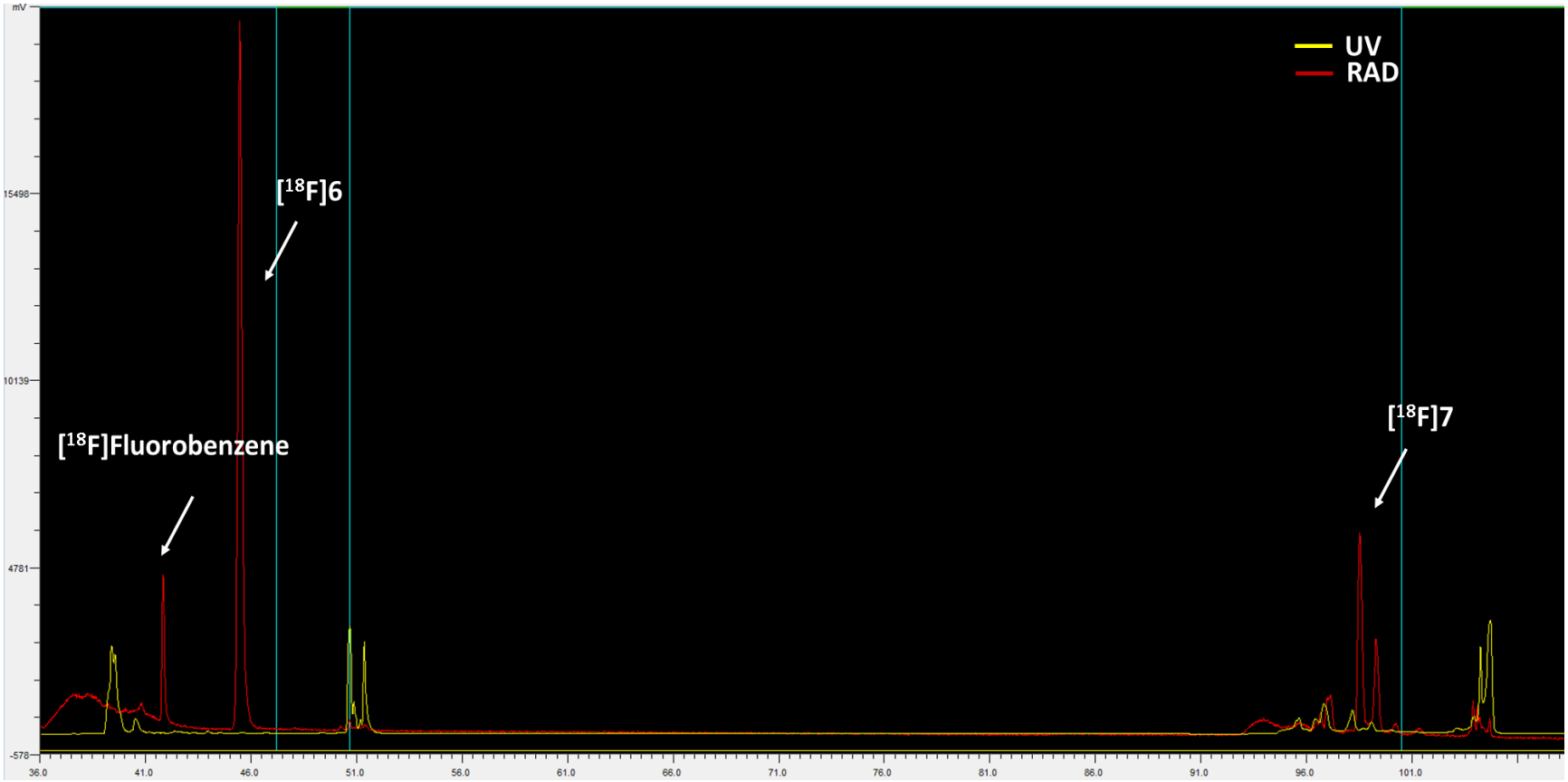

Figure S3-1. Representative semi-Prep HPLC radiochromatogram of purification of products [^{18}F]**6** and [^{18}F]**7** .

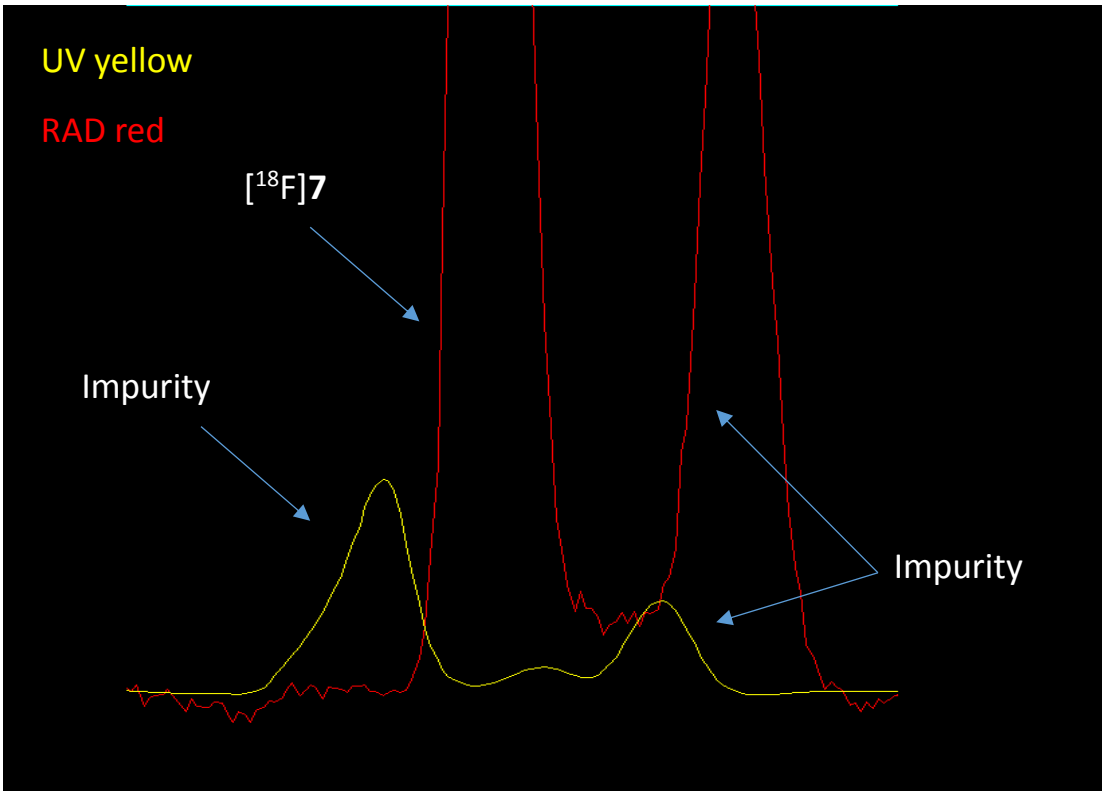

Figure S3-2. Zoomed HPLC chromatogram of [^{18}F]**7** with UV (254 nm) and radiation detection.

Chapter 5: General Discussion, Conclusions and Perspectives

5.1 General discussion

Two new radiotracers radiolabeled with F-18 via Al^{18}F-chelation chemistry (AM project) and via conjugation of a prosthetic group through Pd-mediated cross-coupling (AT_1R project) were developed for PET imaging. Several experiments in the optimization process, analytical characterization and animal studies were presented along the previous chapters of this doctoral thesis. Highlights and new aspects involved in the production of each radiotracer are discussed in the next two subsections.

5.1.1 [^{18}F]AlF-DFH17 for PET imaging of AM receptors

Based on the success demonstrated by [^{99m}Tc]Tc-PulmoBind for SPECT imaging of AM receptors (Chapter 2), the new analog DFH17 was designed as a potential PET tracer for imaging of pulmonary microcirculation. Considering previous SAR studies of PulmoBind, DFH17 was built on the same antagonistic 22-52 peptide segment of human AM replacing the tetrapeptide -RFGT- by a core of Cys^{16}-$(PEG)_4$-Cys^{21} and adding a NOTA chelator for radiometal coordination chemistry. Modifying the chelator type between PulmoBind and DFH17 did not imply drastic differences in pharmacological profile since changes were introduced distant of their pharmacophoric portion. Due to the favorable nuclear properties of F-18 for PET imaging, the peptide was radiolabeled using an attractive approach of fluorination by chelation with the Al-complexation chemistry. This fluorination approach for the peptide was selected due to similarities of aluminum-NOTA coordination chemistry with other transitions radiometals such as ^{68}Ga, ^{64}Cu or ^{44}Sc. Optimal amounts of aluminum to form the Al^{18}F binary complex were found and its production in high concentration was automated for peptide labeling (Chapter 3).

Using inexpensive complexation assays with NOTA, optimal conditions were first found facilitating the radiolabeling optimization of DFH17. Combining the Al-to-DFH17 1:3 with 50% ethanol (v/v) as co-solvent, allowed to produce [^{18}F]AlF-DFH17 in high radiochemical and chemical purities. With a stable final formulation that met the requirements of parenteral radiopharmaceuticals, animal studies were performed to evaluate the in vivo potential of this novel tracer. PET/CT and biodistribution demonstrated high [^{18}F]AlF-DFH17 lung-to-background ratio and *in vivo* stability in rats, dog and primate. Contrasted inter-species uptake in the lungs associated with variations of RAMP2 were detected by PET imaging and theoretical validated by bioinformatic comparison of RAMP2 and CLR primary sequences (Chapter 2) (**Annex II, figure S1**).

Gamma rays emitted by the intact radiotracer and its radiolabeled metabolite(s) cannot be differentiated either by SPECT and/or PET camera. Radiometabolite analysis in plasma is an essential pre-requisite to determine arterial input function for quantitative PET measurements. Therefore, it is important to quantify the chemical form of radiolabeled compounds in biological samples to correct the arterial input function due to plasma radiometabolites [1]. Aiming futures PET studies of AM receptor quantification and tracer kinetic modelling, a radiometabolite study was performed in a dog plasma. Using a column switch HPLC [2] (**Annex II, figure S2**) the presence of labeled metabolites were quantified in plasma samples at 6,12, 30, and 60 min post [^{18}F]AlF-DFH17 injection. Compared to authentic [^{18}F]AlF-DFH17 as control, no labeled metabolites were detected in plasma at all time points demonstrating that there is an important first-pass pulmonary retention in the lung for [^{18}F]AlF-DFH17 (**Annex II, figure S3**). This finding corroborates that lungs are the primary binding site of [^{18}F]AlF-DFH17, mediated via the AM receptors. Furthermore, dosimetry calculations carried out in a primate, resulted in extrapolation of effective dose values to humans higher than FDG but similar to other ^{18}F-labeled tracers. The

urinary bladder was found to be a critical organ (66.5 μSv/MBq) without exceeding the effective dose for renal radiopharmaceuticals routinely used in clinics, such as ^{99m}Tc-DTPA (94 μSv/MBq)[3] (Chapter 2). Altogether, these results support the potential of [^{18}F]AlF-DFH17 as a PET tracer of human AM receptors.

5.1.2 [^{18}F]FB-Candesartan for PET imaging of AT_1 receptors

To our knowledge, Candesartan has never been radiolabeled before with fluor-18 thus we aimed to develop the novel analog [^{18}F]FB-Candesartan with potentially better metabolic profile and biodistribution for future PET studies of AT_1Rs. Initially, the alkyne-Candesartan tritylated precursor and fluorobenzyl-Candesartan (standard) were synthesized and characterized by NMR and HRMS. High stability of tetrazole-protected alkyne-Candesartan versus unprotected, was found in the protected precursor in contrast to unprotected analog, which HPLC chromatograms displayed increasing signs of degradation over a short time. Thus, due to the enhanced long-term stability of alkyne-Candesartan tritylated precursor, the protection of tetrazole moiety was necessary. Such stability allowed storage (at 4-8 ^{o}C) of the protected precursor for radiochemistry runs.

Using the challenging Sonogashira cross-coupling reaction, the alkyne Candesartan precursor was radiofluorinated with the [^{18}F]FIB prosthetic group. After studying the influence of reaction parameters such as solvent, amount of precursor, type of catalyst and temperature; the [^{18}F]FIB prosthetic group was synthesized reproducibly in high yield and purity (Chapter 4). Subsequently, a total of ten different reaction conditions were evaluated with [^{18}F]FIB and the protected alkyne-Candesartan precursor using the Sonogashira cross-coupling reaction. In our

hands, such approach produced [^{18}F]FB-Candesartan in low conversion yields. After studying several Pd-cross-coupling conditions, the radioconversion yield was slightly increased by means of a $Pd(PPh_3)_4$/CuI catalyst and K_2CO_3 as base in DMF. The 3-step process was fully automated on a two-reactor 2-HPLCs synthesis module using the best reaction conditions for [^{18}F]FIB fluorination and coupling to the tetrazol-protected alkyne-Candesartan followed by an acid hydrolysis to yield [^{18}F]FB-Candesartan (Chapter 4).

While calculating the recoveries of each step of the automated process, trapped [^{18}F]FB-Candesartan was detected in the reformulation Sep Pak C18 plus (360 mg) used to remove the semi-Prep HPLC solvent. Aiming to avoid the dilution of the final [^{18}F]FB-Candesartan, two C18 cartridges (Sep Pak C18 1 cc Vac 50 mg and Sep Pak light 130 mg) with less amount of sorbent were investigated. Surprisingly, the sorbent mass of these two cartridges was found insufficient since most of [^{18}F]FB-Candesartan (in 8 mL of CH_3CN/Water 0.1% TFA 55:45, diluted in 45 mL of Water 0.1% TFA) was not trapped, going directly to waste. After obtaining the elution profile of [^{18}F]FB-Candesartan Sep Pak C18 plus (**Annex II, figure S4**), the reformulation process was redesigned with 2 mL ethanol elution followed by evaporation and redissolution in saline containing sodium ascorbate. Other efforts to increase overall radiochemical yield turned out to be fruitless. The MA of the final [^{18}F]FB-Candesartan formulation was low due to the formation of structurally-close impurities during the [^{18}F]FIB coupling and acid hydrolysis detected during the semi-Prep HPLC purification in the module.

The exact mechanism of copper catalyzed Sonogashira reaction is unknown but it is believed to take place through two independent catalytic cycles as depicted in **Figure 1**. Taking into account this mechanistic approach, the rate-determining step would generate a compound

like $R_1Pd(-C{\equiv}CR_2)L_2$ whose *trans/cis* isomerization followed by a reductive elimination could lead to the formation of several structurally close by-products [4]. Several strategies to achieve sufficient separation of [^{18}F]FB-Candesartan from its impurities by varying HPLC conditions were evaluated, and others using different column packing are planned in the future. We were able to succeed in the separation of some impurities, but some others moved together with the peak of interest (**Annex II, figure S5**) thus impeding the production of [^{18}F]FB-Candesartan in high MAs.

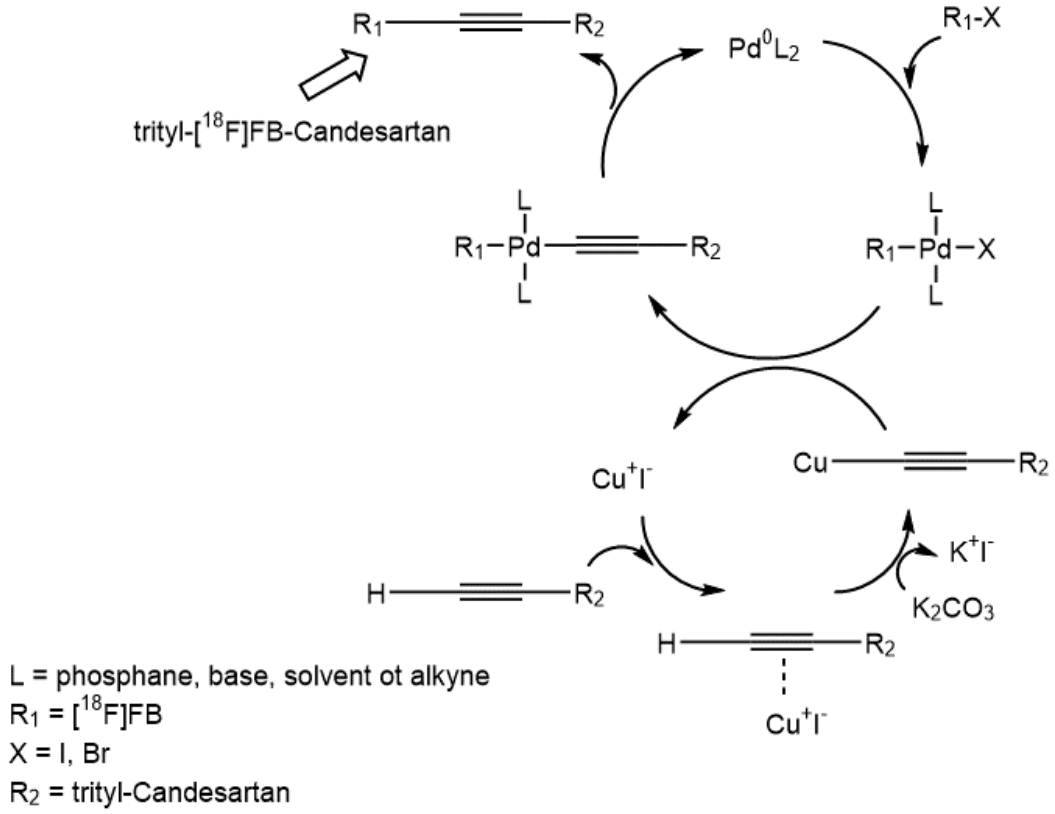

Figure 1. General mechanism of Sonogashira cross-coupling reaction adapted to the [^{18}F]FB-Candesartan synthesis.

The novel [^{18}F]FB-Candesartan was reproducibly produced in high radiochemical purity and stability. It is well-known that high radioactive concentration accelerates the decomposition rate of radiopharmaceuticals by the formation of superoxide and hydroxyl radicals [5]. Thus, reductant stabilizers like sodium ascorbate, slow down the radiolytic decomposition by stopping the electron transfer reaction of superoxide radicals and improving the shelf life of radiopharmaceuticals [6]. Fawdry reported that 10 mg/mL of sodium ascorbate in concentrated formulations of FDG led to high tracer stability for 14 h [7]. Using this amount, no signs of radiolytic decomposition was observed after 4 h post-synthesis, indicating stability of the final [^{18}F]FB-Candesartan formulation.

5.2 Conclusions

In this research project, the two radiotracers [^{18}F]AlF-DFH17 and [^{18}F]FB-Candesartan were developed as new potential PET imaging agents of AM and AT_1 receptors, respectively. [^{18}F]AlF-DFH17 was produced in moderate yields and high chemical and radiochemical purities by complexation of Al^{18}F-to-DFH17 1:3 with 50% ethanol in 0.1M sodium acetate pH 4 at 100 ^{o}C for 15 min. PET studies revealed high tissue contrast in the lungs, absence of labeled metabolites in plasma and favorable dosimetry. Therefore, the new AM derivative [^{18}F]AlF-DFH17 is a promising agent for future applications in molecular PET imaging of pulmonary vascular diseases.

For the first time, the production of[^{18}F]FB-Candesartan based on the Sonograshira cross-coupling reaction with [^{18}F]FIB as prosthetic group was automated in a three-steps two-HPLC purifications process. The tracer was obtained in high radiochemical purity and remained stable up to 4 h post-synthesis in the tracer formulation and up to 1 h in rat plasma at 37 ^{o}C. However,

using this palladium mediated radiofluorination approach to produce [^{18}F]FB-Candesartan in high yields and MAs was turned out to be challenging for routine use in radiochemistry labs, limiting its potential as PET tracer of AT_1 receptors.

5.3 Perspective

5.3.1 [^{18}F]AlF-DFH17 PET imaging

PAH is a pathology characterized by endothelium dysfunctions at lung vascular levels leading to a myo-intimal proliferation causing the progressive obstruction of pulmonary arterioles [8]. Cardiac ultrasound is widely utilized as a diagnostic technique of PAH, but it is imprecise for estimating the systolic pressure of pulmonary arteries [9]. Thus, there is a real need for a more precise non-invasive diagnostic method for early detection and dynamic monitoring of the integrity of pulmonary microcirculation.

To our knowledge, the novel AM derivative DFH17 is unique and has never been radiolabeled before with fluor-18. Considering the experiences with ^{99m}Tc-PulmoBind (presented along Chapter 2) and the results obtained in this research project (Chapters 2 and 3), this novel tracer appears promising for PET imaging of pulmonary microcirculation. However, the advancement of [^{18}F]AlF-DFH17 for clinical applications requires the development of a kinetic model for the accurate quantification of AM receptors in healthy and diseased animals first. [^{18}F]AlF-DFH17 PET studies in PAH murine models such as monocrotaline [10] and Sugen-hypoxia [11], causing angioproliferative lung damage with obstruction of small pulmonary arteries, will not only allow imaging of large perfusion deficits but also early detection of microvascular damage. Micro PET quantifications will then be correlated with molecular and histology analyses

of pulmonary tissues to determine the expression of AM receptors. In addition, the effect of pulmonary micro-embolization (as obliteration model of pulmonary arterioles) in the accumulation and spatial distribution of [^{18}F]AlF-DFH17 will be study by dynamic PET acquisitions. After successive embolization of 100 µm microspheres in a dog, we will demonstrate that blocked arterioles cause an increase in vascular resistance and pulmonary pressure corresponding to four million microspheres. Thus, the micro-embolization study will be aimed at finding a correspondence between the embolization of microspheres, their hemodynamic pattern and PET imaging with [^{18}F]AlF-DFH17 of AM receptors.

There is currently no cure for PAH, and the development of effective medication is limited by the lack of non-invasive tests that can screen the disease at an early stage and monitor its progression. In a near future, the successful development of [^{18}F]AlF-DFH17 will establish a new non-invasive imaging modality of pulmonary microcirculation with greater resolution and sensitivity via PET. The structural similarities of DFH17 to PulmoBind (soon in Clinical trial Phase III) will facilitate the approval of Health Canada as an effective PET biomarker for diagnostic of pulmonary hypertension and pulmonary embolism via AM receptors. This approach would present an excellent opportunity to advance understanding of the pathophysiology of AM receptors and its involvement in PAH as well as better guide the therapy and monitor disease progression.

5.3.2 [^{18}F]FB-Candesartan PET imaging

Cardiovascular disease is the most common cause of death among chronic kidney disease, and patients are likely to experience cardiovascular problems such as angina, heart attack, stroke or HF [12]. RAS-dependent antihypertensive treatments, such as ARB Losartan and Candesartan, are known to promote regression of such diseases. Therefore, the use of a new PET imaging probe based on the high affinity ARB Candesartan is expected to provide a

new detection methodology with greater resolution and sensitivity. [^{18}F]FB-Candesartan is the first ARB-based derivative radiolabeled with [^{18}F]FIB following the Sonogashira cross-coupling reaction. Thus, such analog with similar characteristics compared to clinically used Candesartan will facilitate translational work (animal to human) and approval from Health Canada. Renal and cardiac AT_1R expression has been found to be altered in disease states but its regulatory mechanism is still partially understood [13]. Using [^{18}F]FB-Candesartan would present a unique opportunity to advance understanding at a molecular level of the pathophysiology of various diseases, including HF, hypertension, cardiac and renal failures, and some types of cancers. In addition to cardiovascular diseases, this research could be expanded to diabetes mellitus to assess associated AT_1R alterations [14] and further investigate the relationship between RAS blockade and glycemic effect via PET imaging.

Nonetheless, due to the low MA of [^{18}F]FB-Candesartan caused by the presence of unlabeled impurities that could not be separated, its potential to image organs that express low levels of AT_1Rs (such as the heart) will be limited. However, such imaging would be possible in tissues that abundantly express AT1Rs such as the kidney. As reported by Ismail *et al.* [15] a reduction of renal AT_1Rs in hypertensive animal models was detected by PET using [^{18}F]FPyKYNE- Losartan with molar activities as low as 4 000 GBg/mmol. Therefore, starting with higher levels of F-18 activity (e.g. 10 Ci instead of 2 Ci as in here), the actual MA of [^{18}F]FB-Candesartan (~5 500 GBq/mmol) could be enhanced 5x to 27 500 GBq/mmol, allowing PET quantifications of renal AT_1Rs and multiple injections per formulation. Several strategies to reduce the formation of by-products could be investigated, such as exploring new Pd catalyst and less aggressive acid hydrolysis of the tetrazole group. Pd catalyst such as bis(triphenylphosphine)palladium chloride is one of the mostly utilized catalyst for the Sonogashira reaction. Consequently, we thus hypothesize that using $Pd(PPh_3)_2Cl_2$ could lead to the formation of less or even different side-products during the geometrical rearrangement and

reductive elimination step of Sonogashira mechanism, rendering the HPLC separation possibly less challenging. In addition, a combination of factors, such as TFA concentration, hydrolysis time and temperature which maximize the yield of the tetrazole deprotection with less formation of hydrolysis side-products, could also be investigated. We are also planning to explore new alternatives to C18 reverse phase resins, such as Kinetex biphenyl, whose core-shell unique stationary phase has shown enhanced resolution power. By combining this HPLC column with the appropriate solvent system and pH, we expect to improve the separation of [^{18}F]FB-Candesartan from it by-product impurities. By doing so, we believe that the low MA obstacle will be overcome allowing the production of [^{18}F]FB-Candesartan at higher MA at EOS.

The successful development of [^{18}F]FB-Candesartan in high MAs will permit the full investigation of its pharmacological binding profile and metabolism in small animals. If [^{18}F]FB-Candesartan exhibits selective binding with no labeled metabolites in the tissue of interest, that would complicate signal quantification, then this tracer will provide a novel molecular imaging probe for measuring AT_1Rs that has never been investigated by PET imaging in animals or humans. This imaging approach will equally provide non-invasive insights into drug responses at AT_1R level that may help to optimize dose, guide therapy, monitor disease progression; and reduce adverse effects in patients with heart, renal failures and hypertension.

5.4 References

[1] Pawelke B. Metabolite analysis in positron emission tomography studies: examples from food sciences. Amino Acids 2005;29:377-88.

[2] Hilton J, Yokoi F, Dannals RF, Ravert HT, Szabo Z, and Wong DF. Column-switching HPLC for the analysis of plasma in PET imaging studies. Nuclear Medicine and Biology 2000;27:627-30.

[3] Stabin M, Taylor A, Eshima D, and Wooter W. Radiation dosimetry for technetium-99m-MAG3, technetium-99m-DTPA, and iodine-131-OIH based on human biodistribution studies. Journal of nuclear medicine : official publication, Society of Nuclear Medicine 1992;33:33-40.

[4] Chinchilla R and Nájera C. The Sonogashira Reaction: A Booming Methodology in Synthetic Organic Chemistry. Chemical Reviews 2007;107:874-922.

[5] Hiroki A, Pimblott SM, and LaVerne JA. Hydrogen Peroxide Production in the Radiolysis of Water with High Radical Scavenger Concentrations. The Journal of Physical Chemistry A 2002;106:9352-8.

[6] Gregory NL. Mechanism of radioprotection by vitamin C. Br J Radiol 1978;51:473-5.

[7] Fawdry RM. Radiolysis of 2-[18F]fluoro-2-deoxy-D-glucose (FDG) and the role of reductant stabilisers. Appl Radiat Isot 2007;65:1193-201.

[8] Morrell NW, Adnot S, Archer SL, Dupuis J, Lloyd Jones P, MacLean MR, *et al.*. Cellular and Molecular Basis of Pulmonary Arterial Hypertension. Journal of the American College of Cardiology 2009;54:S20-S31.

[9] Dupuis J, Harel F, and Nguyen QT. Molecular imaging of the pulmonary circulation in health and disease. Clin Transl Imaging 2014;2:415-26.

[10] Dupuis J, Harel F, Fu Y, Nguyen QT, Letourneau M, Prefontaine A, *et al.*. Molecular imaging of monocrotaline-induced pulmonary vascular disease with radiolabeled linear adrenomedullin. J Nucl Med 2009;50:1110-5.

[11] Letourneau M, Nguyen QT, Harel F, Fournier A, and Dupuis J. PulmoBind, an adrenomedullin-based molecular lung imaging tool. J Nucl Med 2013;54:1789-96.

[12] Go AS, Chertow GM, Fan D, McCulloch CE, and Hsu CY. Chronic kidney disease and the risks of death, cardiovascular events, and hospitalization. The New England journal of medicine 2004;351:1296-305.

[13] Uemura H, Hasumi H, Ishiguro H, Teranishi J-i, Miyoshi Y, and Kubota Y. Renin-angiotensin system is an important factor in hormone refractory prostate cancer. The Prostate 2006;66:822-30.

[14] Harrison-Bernard LM, Imig JD, and Carmines PK. Renal AT1 receptor protein expression during the early stage of diabetes mellitus. Int J Exp Diabetes Res 2002;3:97-108.

[15] Ismail B, deKemp RA, Hadizad T, Mackasey K, Beanlands RS, and DaSilva JN. Decreased renal AT1 receptor binding in rats after subtotal nephrectomy: PET study with [(18)F]FPyKYNE-losartan. EJNMMI research 2016;6:55-.

\

Annex I: Spectral data for Chapter 4

*Hydroxy Candesartan derivative ((1-((2'-(1H-tetrazol-5-yl)-[1,1'-biphenyl]-4-yl)methyl)-2-ethoxy-1H-benzo[d]imidazol-7-yl)methanol) (**2**)*

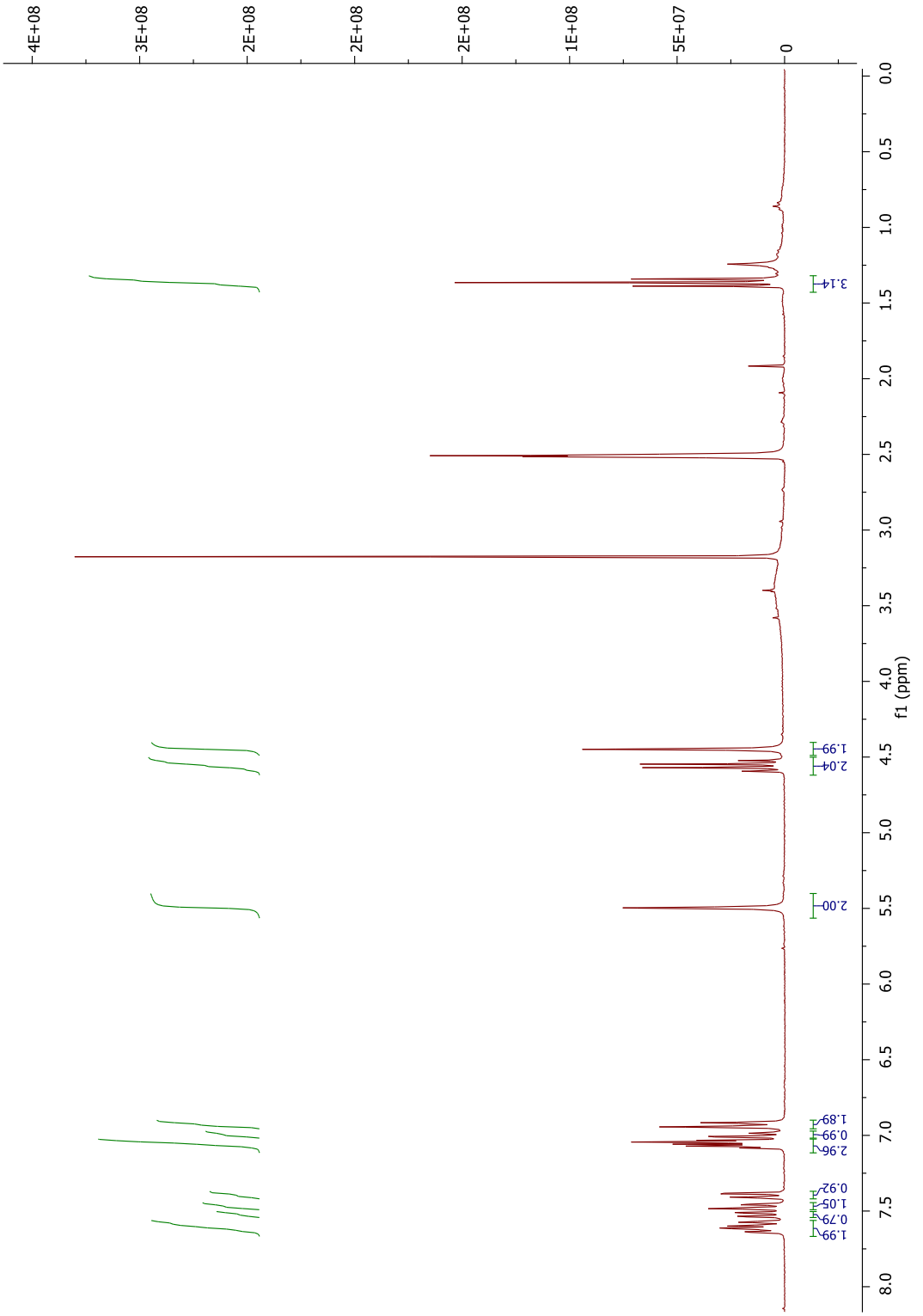

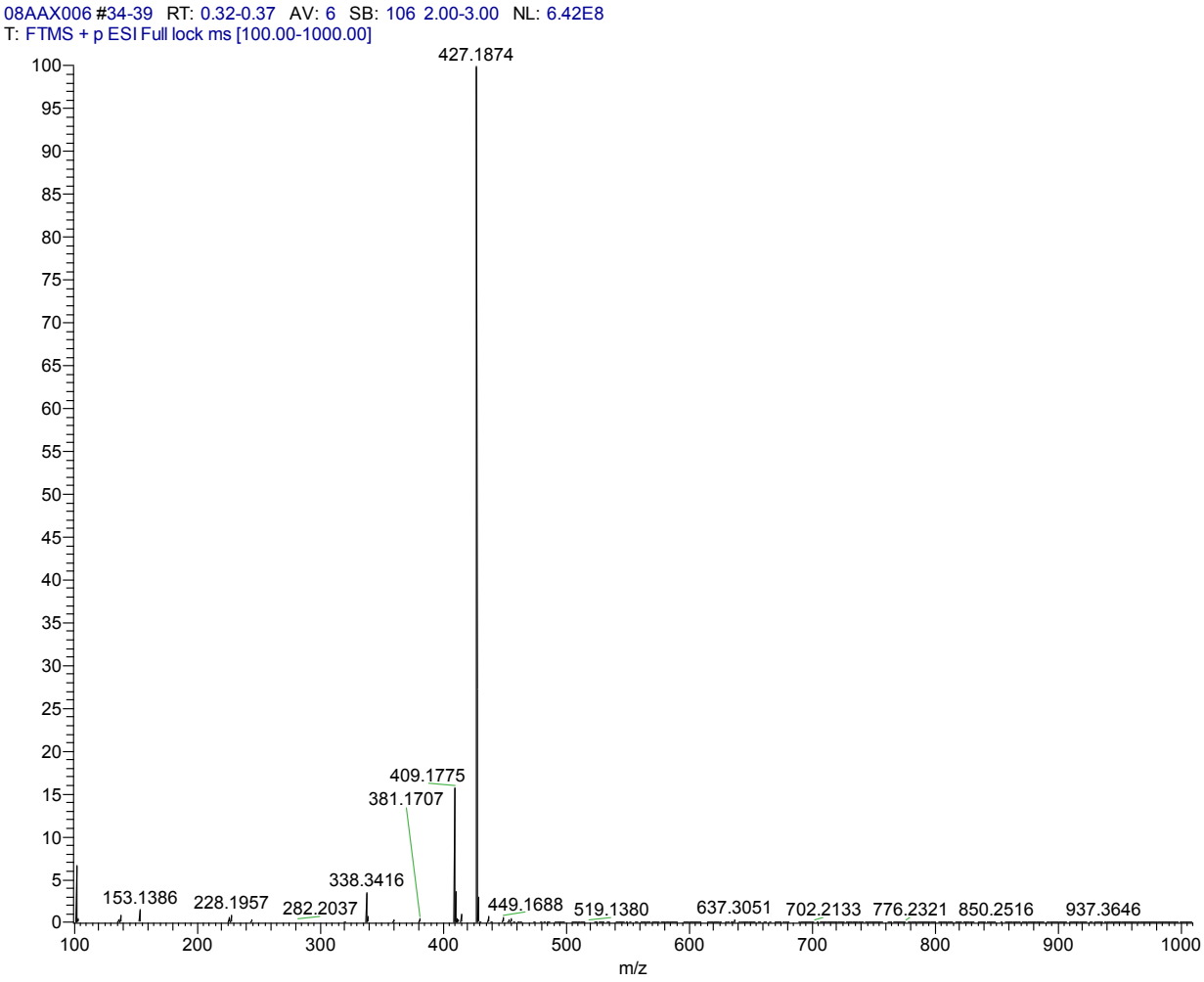
08AAX006 #34-39 RT: 0.32-0.37 AV: 6 SB: 106 2.00-3.00 NL: 6.42E8
T: FTMS + p ESI Full lock ms [100.00-1000.00]
427.1874
409.1775
381.1707
153.1386
228.1957
282.2037
338.3416
449.1688
519.1380
637.3051
702.2133
776.2321
850.2516
937.3646
m/z

*Tetrazole-protected hydroxy Candesartan derivative ((2-ethoxy-1-((2'-(1-trityl-1H-tetrazol-5-yl)-[1,1'-biphenyl]-4-yl)methyl)-1H-benzo[d]imidazol-7-yl)methanol) (**3**)*

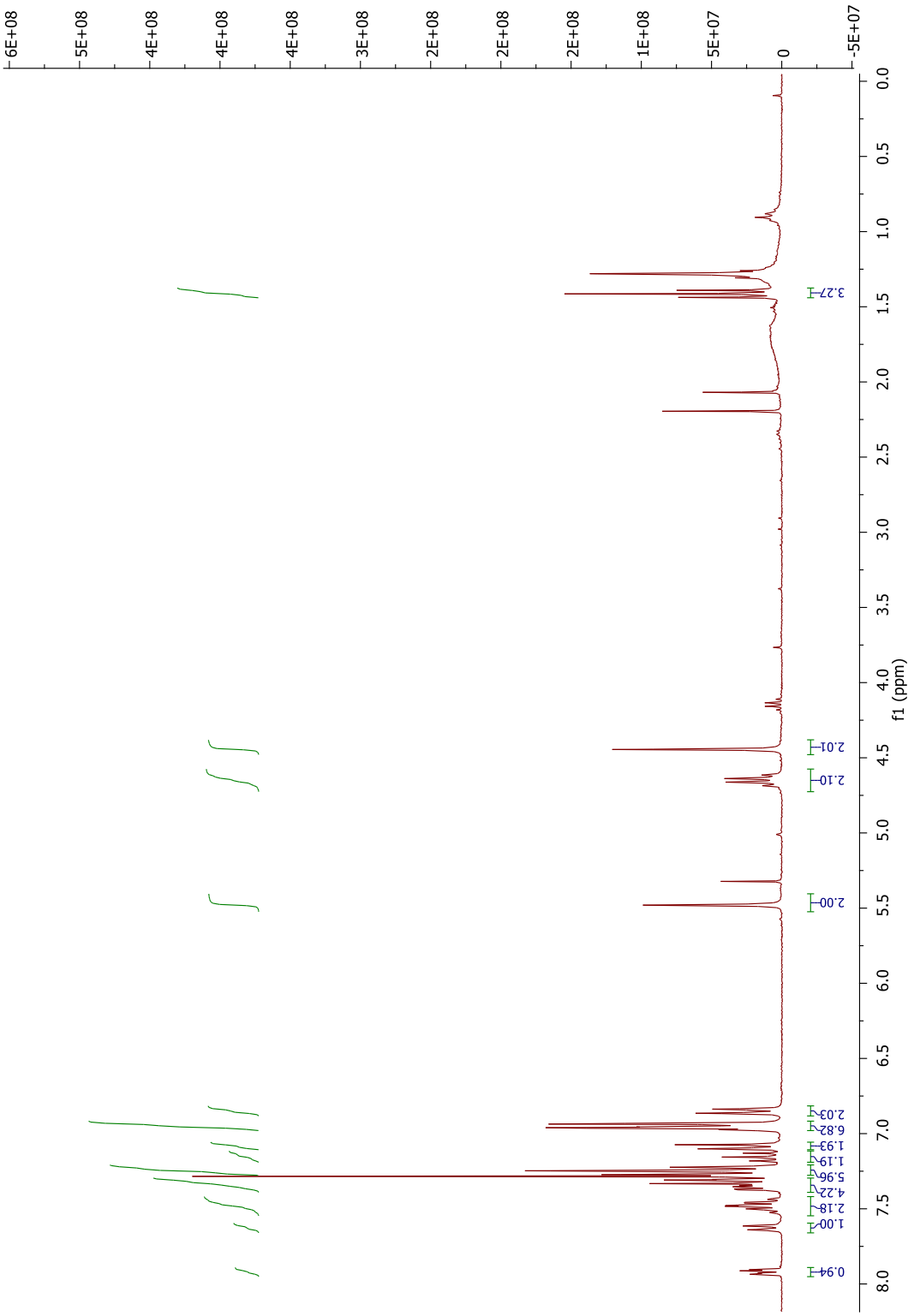

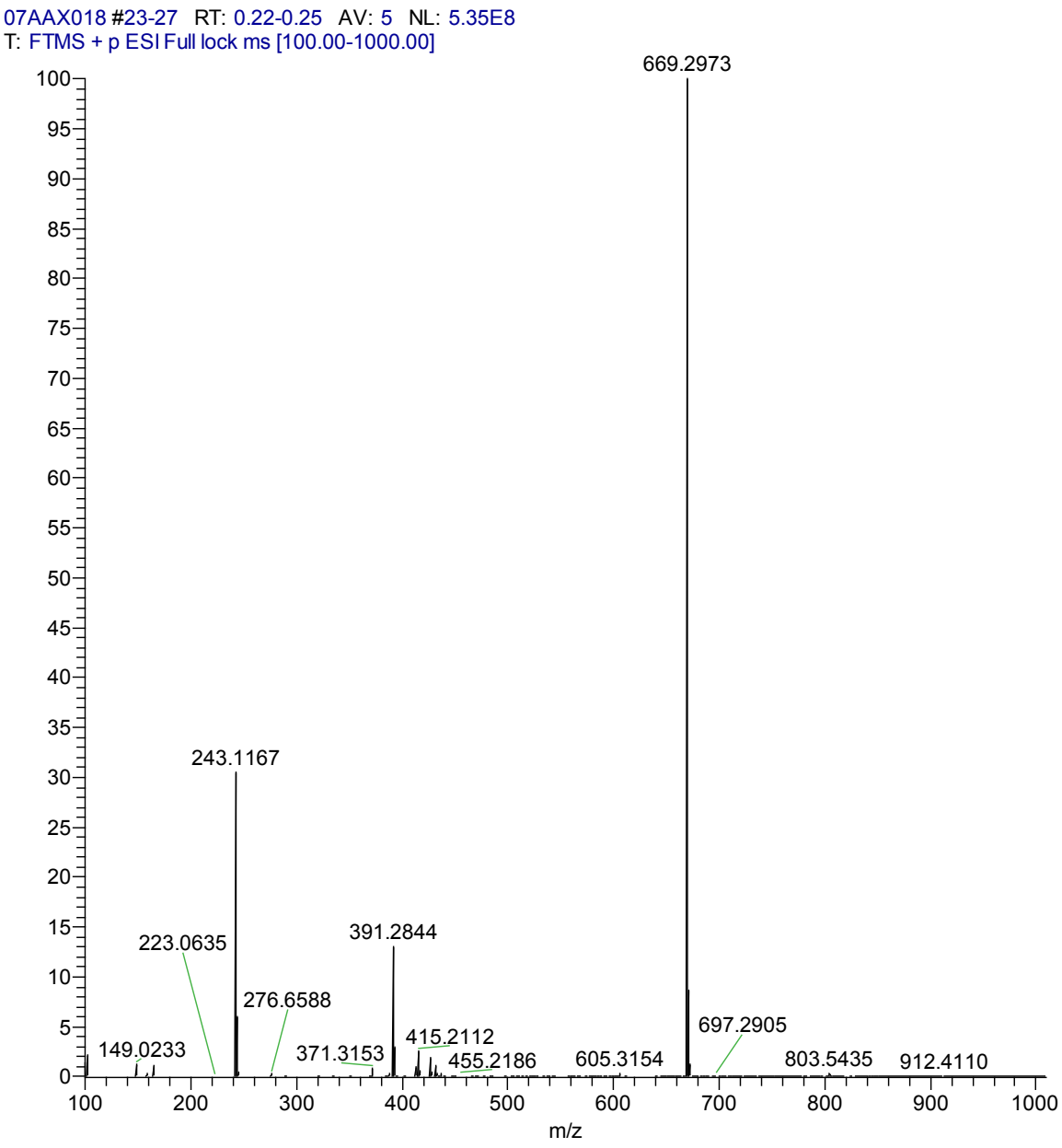
07AAX018 #23-27 RT: 0.22-0.25 AV: 5 NL: 5.35E8
T: FTMS + p ESI Full lock ms [100.00-1000.00]
669.2973
243.1167
223.0635
391.2844
276.6588
415.2112
455.2186
149.0233
371.3153
605.3154
697.2905
803.5435
912.4110
m/z

*Tetrazole-protected bromide Candesartan derivative (7-(bromomethyl)-2-ethoxy-1-((2'-(1-trityl-1H-tetrazol-5-yl)-[1,1'-biphenyl]-4-yl)methyl)-1H-benzo[d]imidazole) (**4**)*

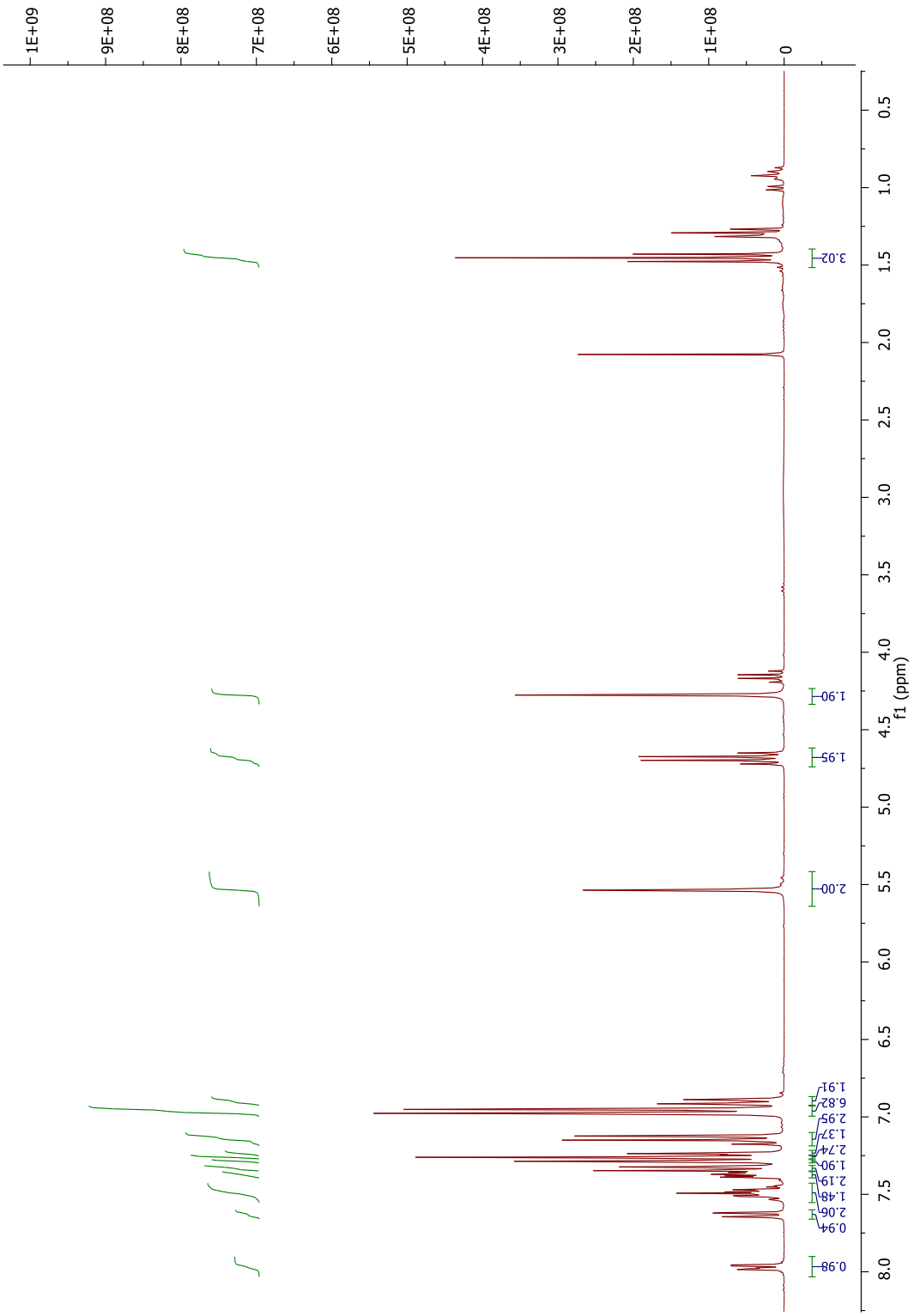

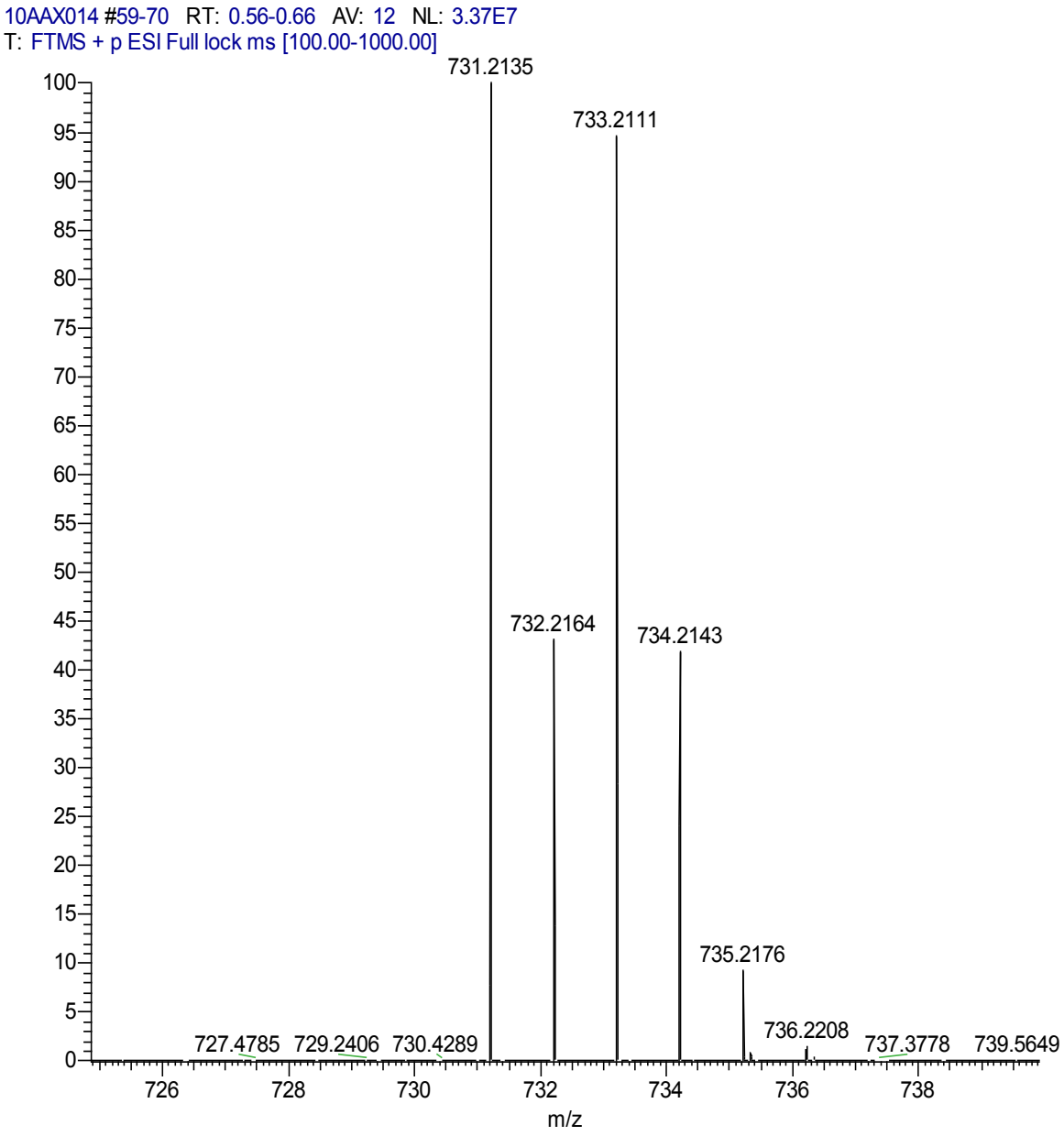
10AAX014 #59-70 RT: 0.56-0.66 AV: 12 NL: 3.37E7
T: FTMS + p ESI Full lock ms [100.00-1000.00]
731.2135
733.2111
732.2164
734.2143
735.2176
736.2208
727.4785
729.2406
730.4289
737.3778
739.5649
m/z

*Tetrazole-protected alkyne Candesartan (7-((but-3-yn-1-yloxy)methyl)-2-ethoxy-1-((2'-(1-trityl-1H-tetrazol-5-yl)-[1,1'-biphenyl]-4-yl)methyl)-1H-benzo[d]imidazole) (**5**)*

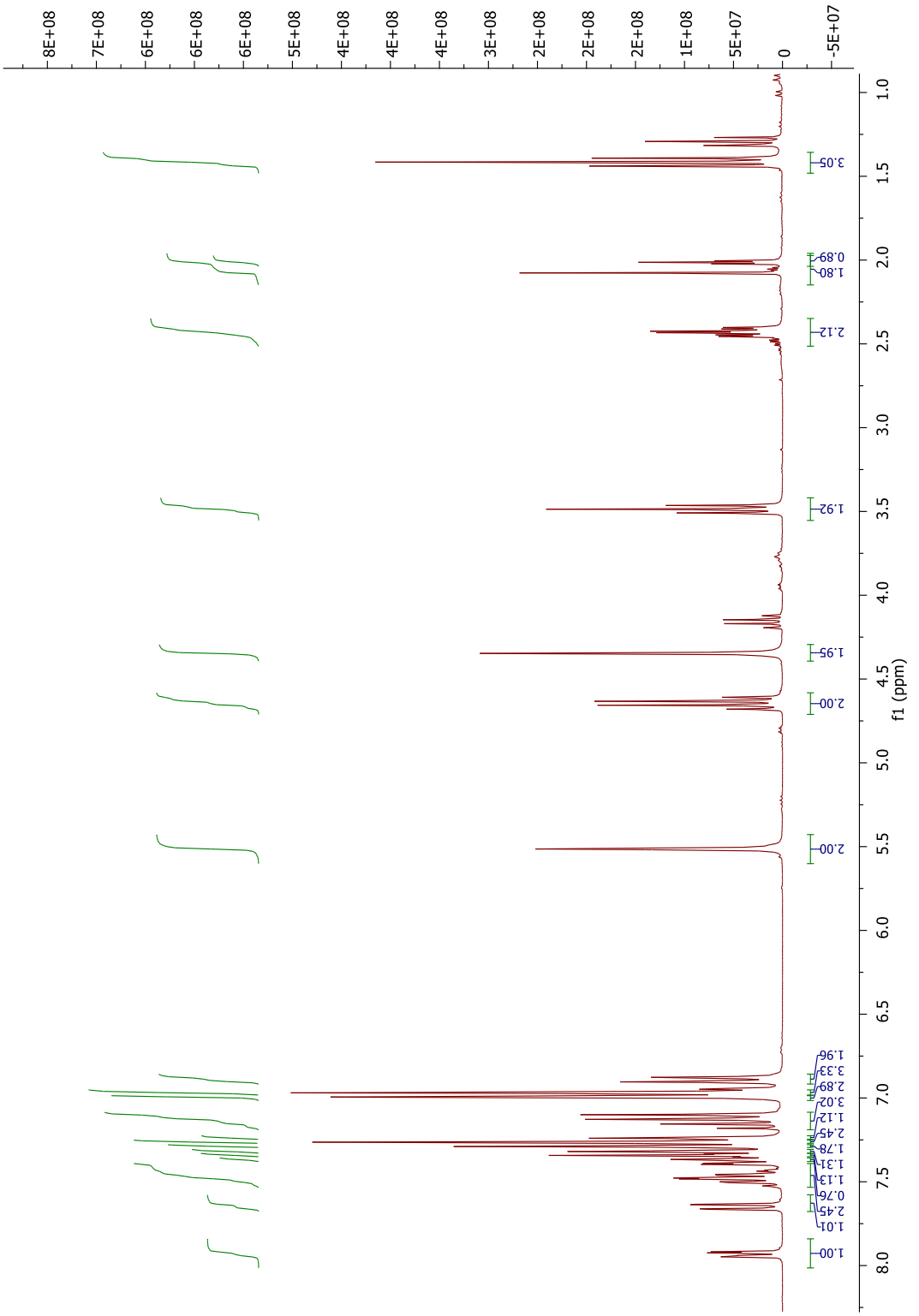

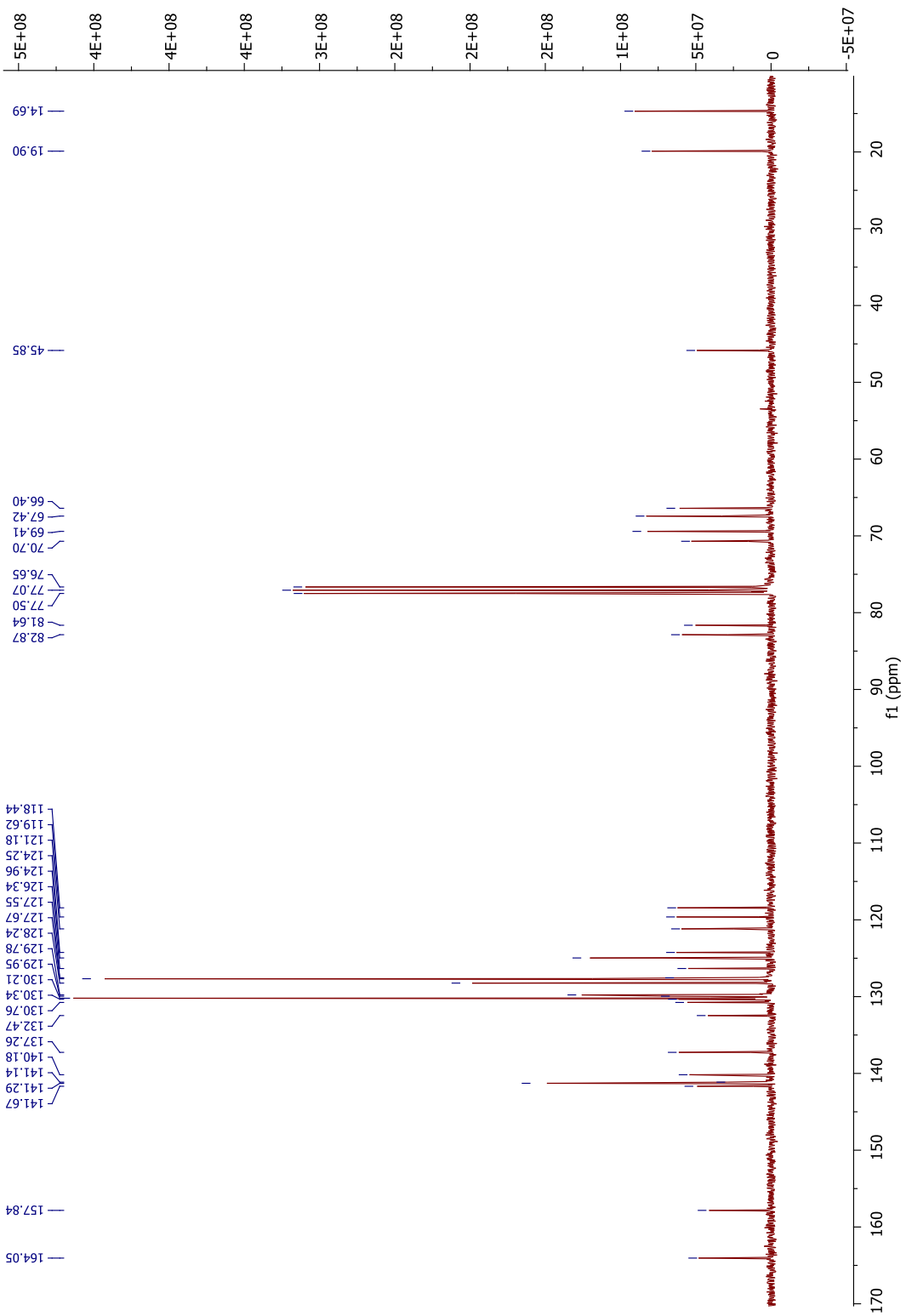
5E+08
4E+08
4E+08
4E+08
3E+08
2E+08
2E+08
2E+08
1E+08
5E+07
0
-5E+07
14.69
19.90
45.85
66.40
67.42
69.41
70.70
76.65
77.07
77.50
81.64
82.87
118.44
119.62
121.18
124.25
124.96
126.34
127.55
127.67
128.24
129.78
129.95
130.21
130.34
130.76
132.47
137.26
140.18
141.14
141.29
141.67
157.84
164.05
20
30
40
50
60
70
80
90
100
110
120
130
140
150
160
170
f1 (ppm)

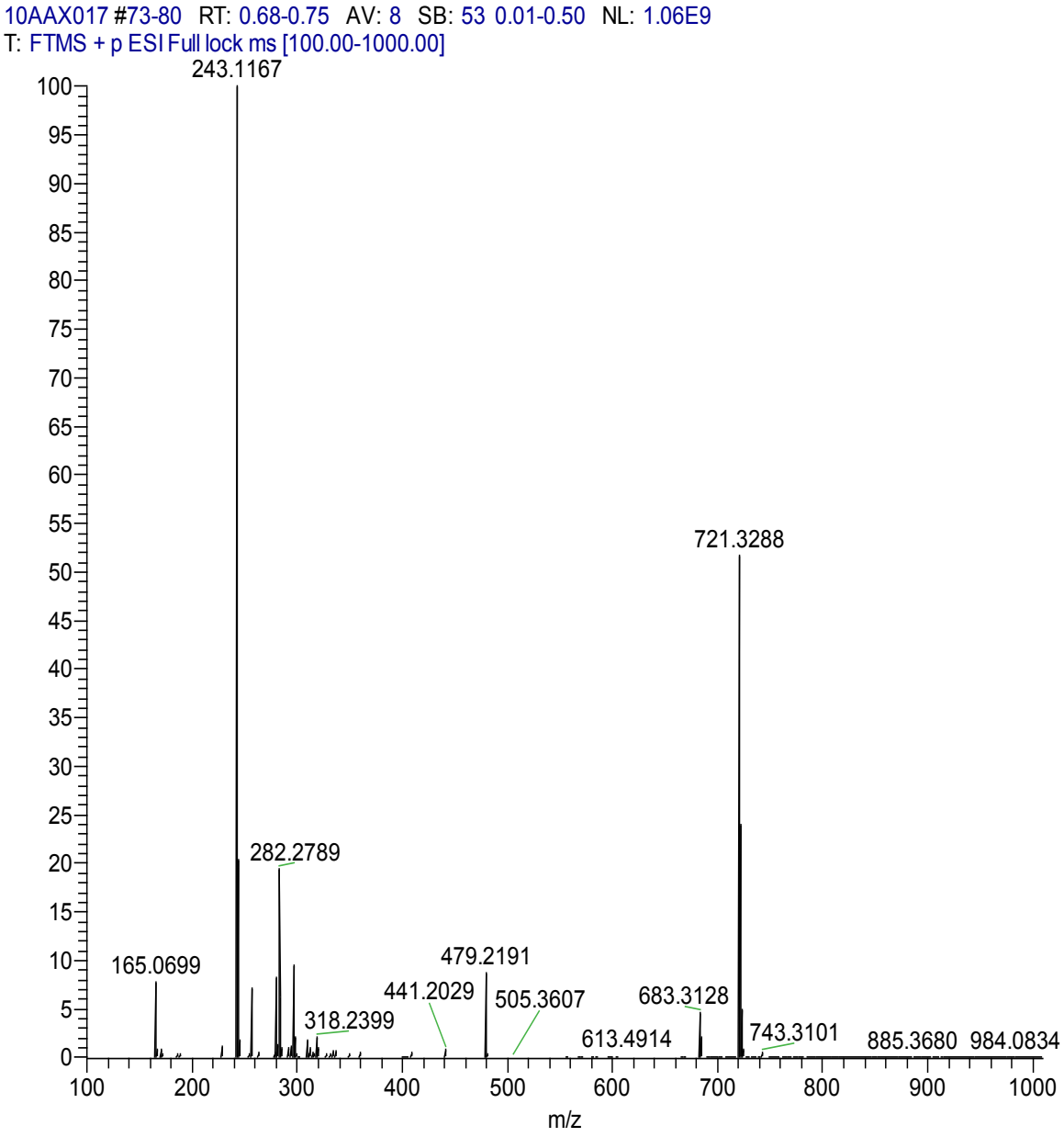
10AAX017 #73-80 RT: 0.68-0.75 AV: 8 SB: 53 0.01-0.50 NL: 1.06E9
T: FTMS + p ESI Full lock ms [100.00-1000.00]
243.1167
721.3288
282.2789
165.0699
479.2191
441.2029
505.3607
683.3128
318.2399
613.4914
743.3101
885.3680
984.0834
m/z

*Fluorobenzyl-Candesartan (1-((2'-(1H-tetrazol-5-yl)-[1,1'-biphenyl]-4-yl)methyl)-2-ethoxy-7-(((4-(4-fluorophenyl)but-3-yn-1-yl)oxy)methyl)-1H-benzo[d]imidazole) (**7**)*

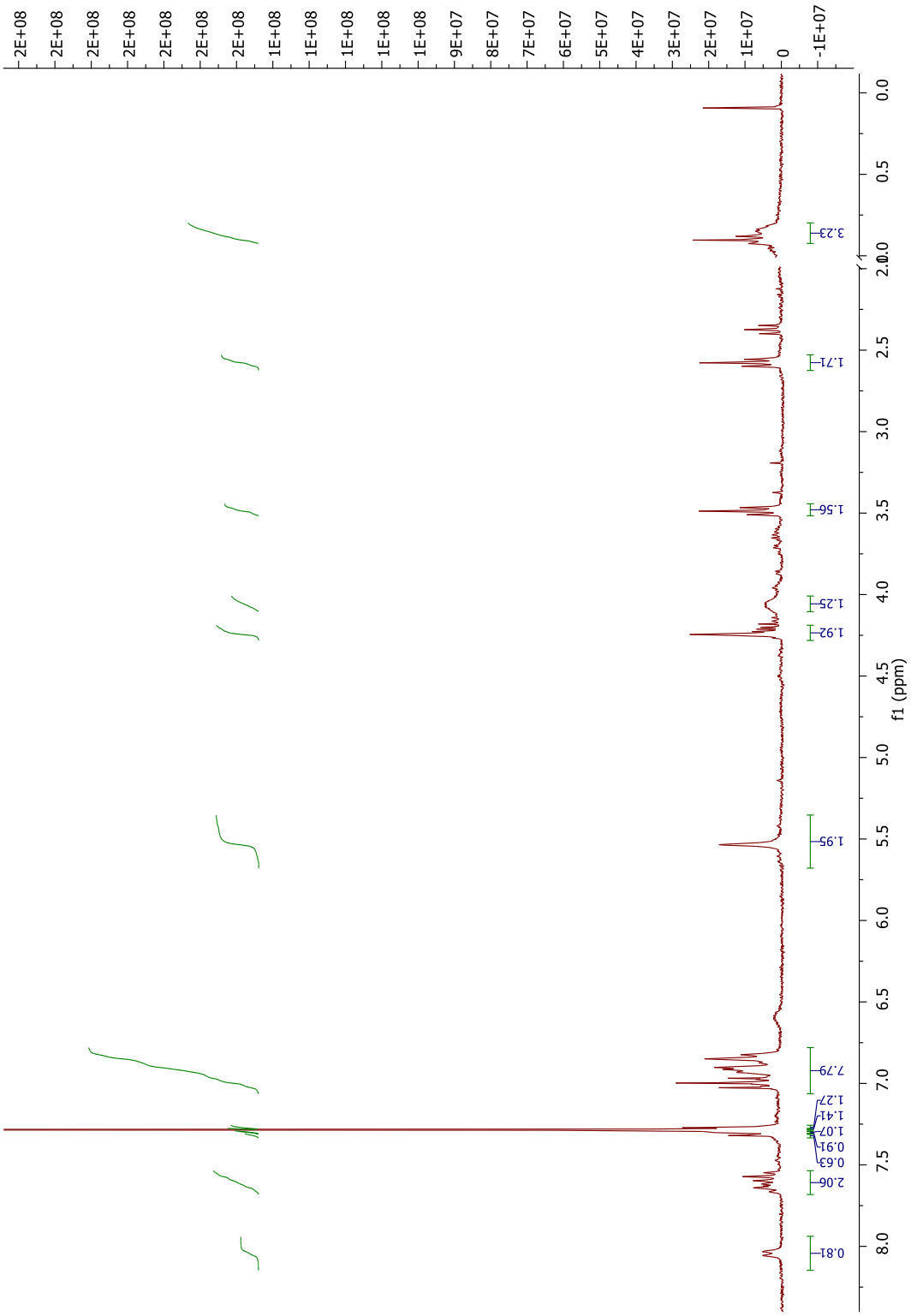

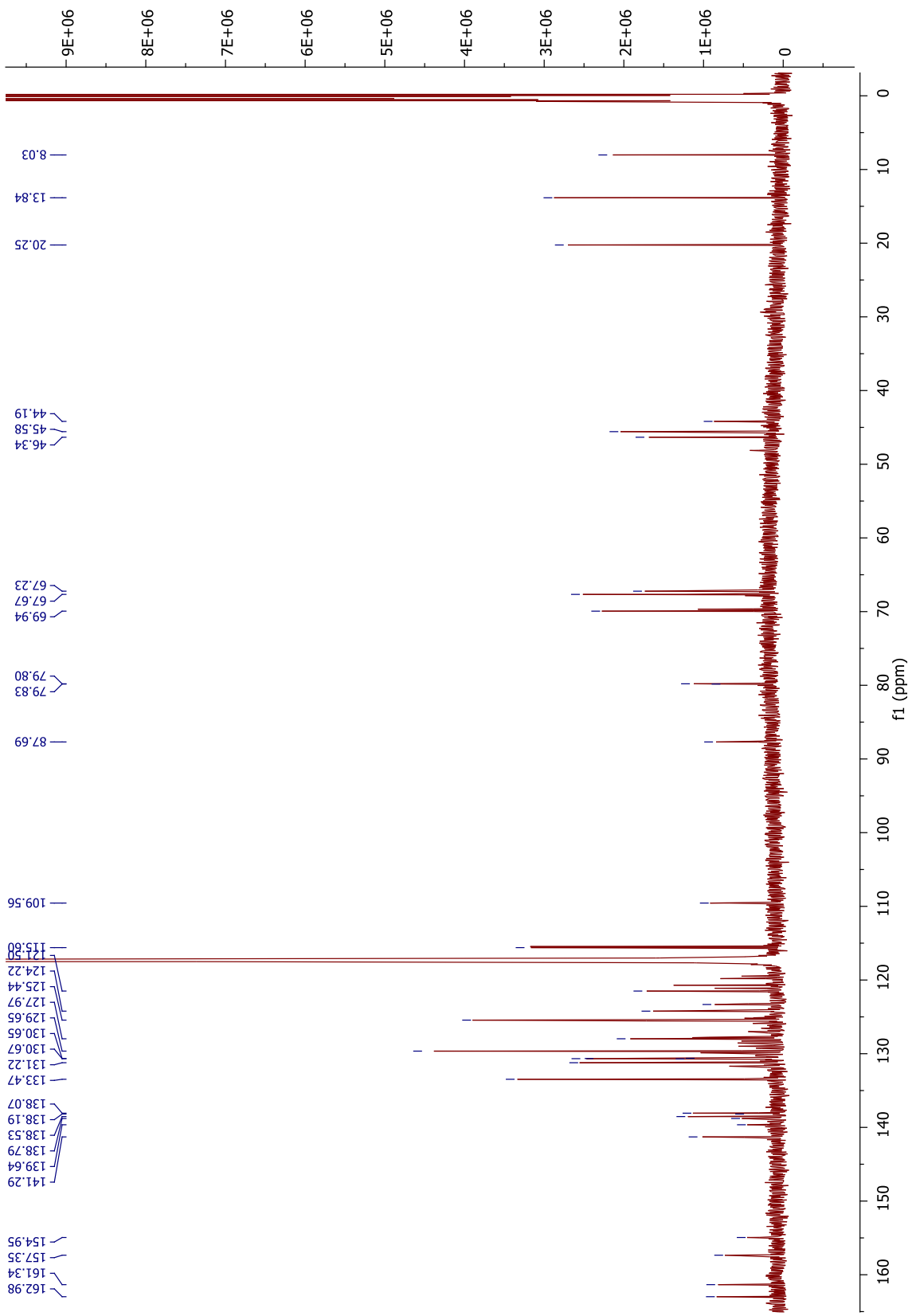
8.03
13.84
20.25
44.19
45.58
46.34
67.23
67.67
69.94
79.80
79.83
87.69
109.56
115.60
121.80
124.22
125.44
127.97
129.65
130.65
130.67
131.22
133.47
138.07
138.19
138.53
138.79
139.64
141.29
154.95
157.35
161.34
162.98
f1 (ppm)

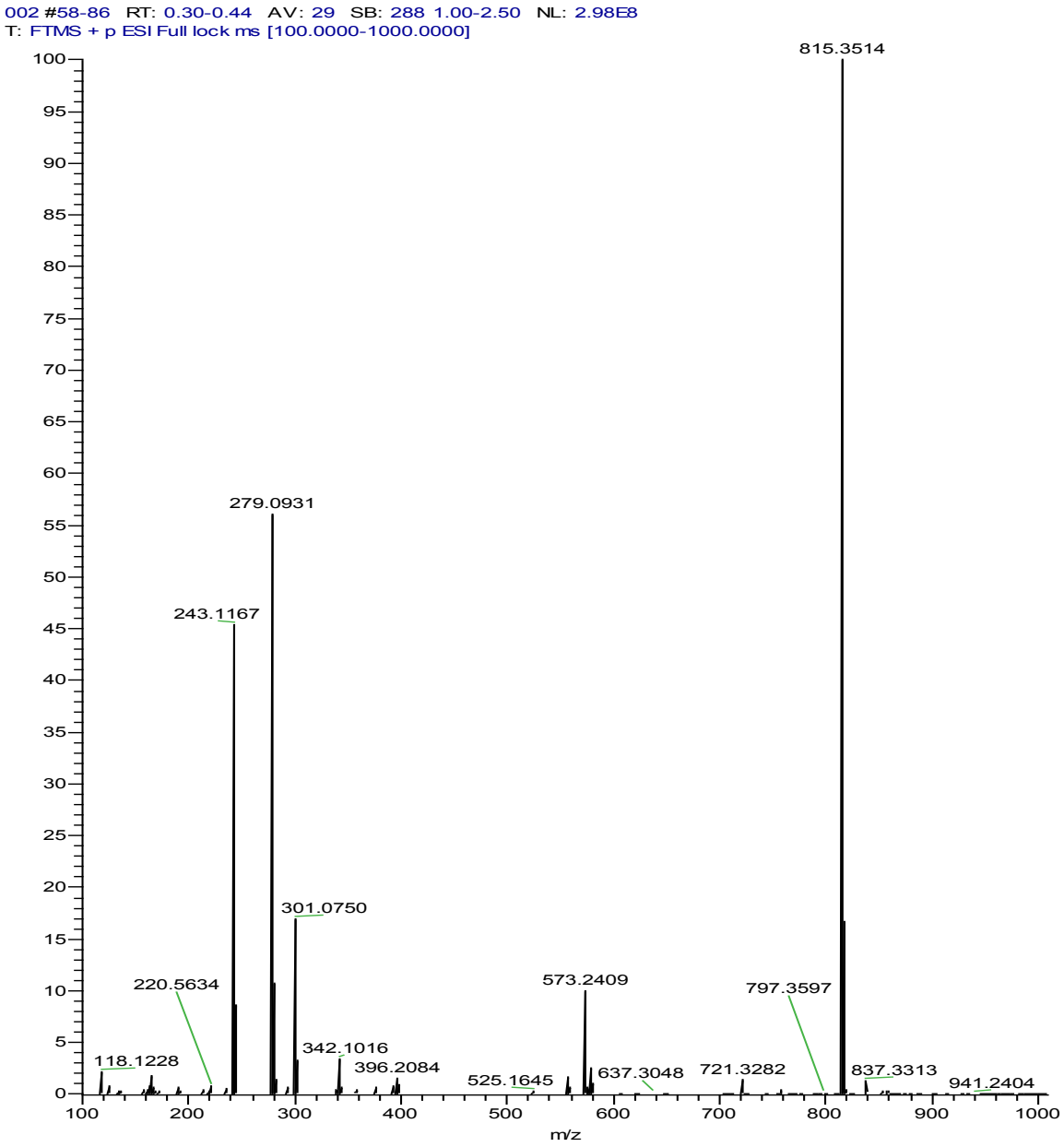
002 #58-86 RT: 0.30-0.44 AV: 29 SB: 288 1.00-2.50 NL: 2.98E8
T: FTMS + p ESI Full lock ms [100.0000-1000.0000]
815.3514
279.0931
243.1167
301.0750
220.5634
573.2409
797.3597
342.1016
396.2084
118.1228
525.1645
637.3048
721.3282
837.3313
941.2404
m/z

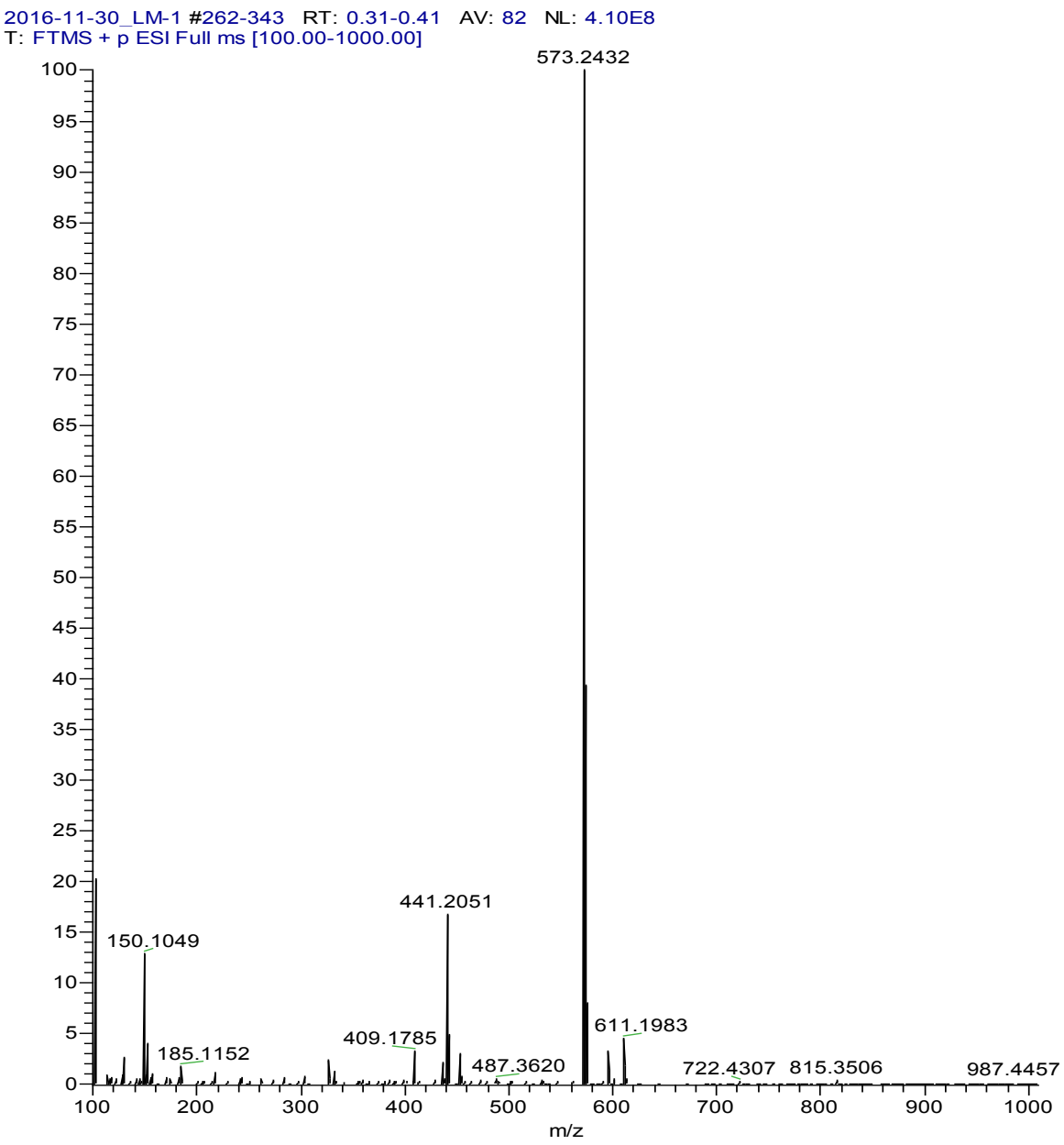
2016-11-30_LM-1 #262-343 RT: 0.31-0.41 AV: 82 NL: 4.10E8
T: FTMS + p ESI Full ms [100.00-1000.00]
573.2432
441.2051
150.1049
611.1983
409.1785
185.1152
487.3620
722.4307
815.3506
987.4457
m/z

Annex II: Supporting information for Chapter 5

Figure S1. Multiple-sequence alignment of AM receptor sub-components CLR (left) and RAMP2 (right) of rat, dog, primate and human. The study was performed with the multiple sequence alignment tool: Clustal omega available at EMBL-EBI website. CLR sub-component of AM receptor it is conserved among species since the percent of identity is high (~90%). In contrast, RAMP2 varies considerably from rat to human (68% vs 100%), showing high differences in the identity of their primary sequence. This variation of RAMP2 is the responsible of contrasted inter-species [^{18}F]AlF-DFH17 uptake observed by PET imaging.

Determination of dog plasma radiometabolites

Methodology

Blood samples were centrifuged and 1 mL supernatant (plasma) was transferred to a vial containing 0.5 g urea (to disrupt tracer bound to plasma proteins and allow for analyses of free labeled molecules). The sample is incubated at 37 ^{o}C to dissolve urea and then filtered through a 22 µm glass filter. After plasma injection in (V1) (**Figure S2**), the sample is transferred from the injection loop with 1:99 CH_3CN / H_2O 0.1 % TFA to the capture column C1 while the valve V2 is directly connected to the detector.

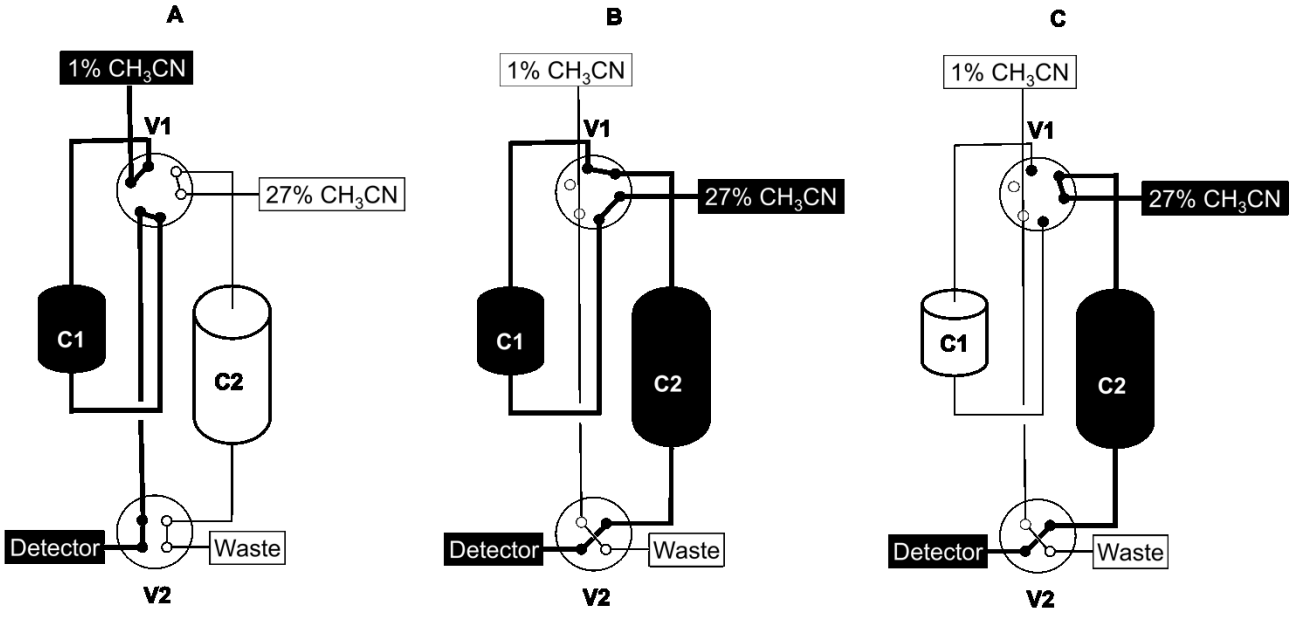

Figure S2. Colum switch HPLC for radiometabolite analysis. C1 Capture column (Oasis HLB) and C2 Analytical column (Phenomenex Luna C18). Flow rates: C1, 1 mL/min and C2, 2 mL/min.

In this first 4 min, the detection corresponds to hydrophilic metabolites that are too polar to bind the sorbent in C1. Once the UV detection displays no more elution of macromolecules, V1 is **switched** to allow the analytical solvent (27 % CH_3CN / H_2O 0.1 % TFA) to back-flush C1 onto C2 and V2 is connected to the detector. During the first 5 min, V1 is returned to the initial position to wash C1 with 1:99 CH_3CN / H_2O 0.1 % TFA in preparation for the next plasma sample analysis. After 5 min, the intact tracer and its hydrophobic metabolites (if present) are separated in C2. Finally, C2 is rinsed with 100% CH_3CN to verify that all radioactive products had been eluted, before re-equilibration with the HPLC solvent (27 % CH_3CN / H_2O 0.1 % TFA).

Data processing and results

HPLC software (PeakSimple 2.83) is used to integrate the peaks (that are decay-corrected).in the chromatograms. The %AUC of all peaks is compared to the intact peak of non-metabolized tracer (similar t_R of control) at all time points. (6, 12, 30, and 60 min). As depicted in **Figure S3** upper panel, control experiments were aimed to find separation conditions of authentic [^{18}F]AlF-DFH17 (left) and with plasma containing 0.5 g of urea (right). It was found that 5% of tracer was nonspecifically bound to plasma proteins (eluting with them at the beginning). Approximately 3% of [^{18}F]AlF-DFH17 was found bound to dog plasma proteins (**Figure S3** down panel, -5 min). Compared to this authentic control (-5 min), neither hydrophilic nor hydrophobic [^{18}F]AlF-DFH17 metabolites were detected in all time point studied (**Figure S3** down panel, 6, 12, 30, and 60 post-injection)

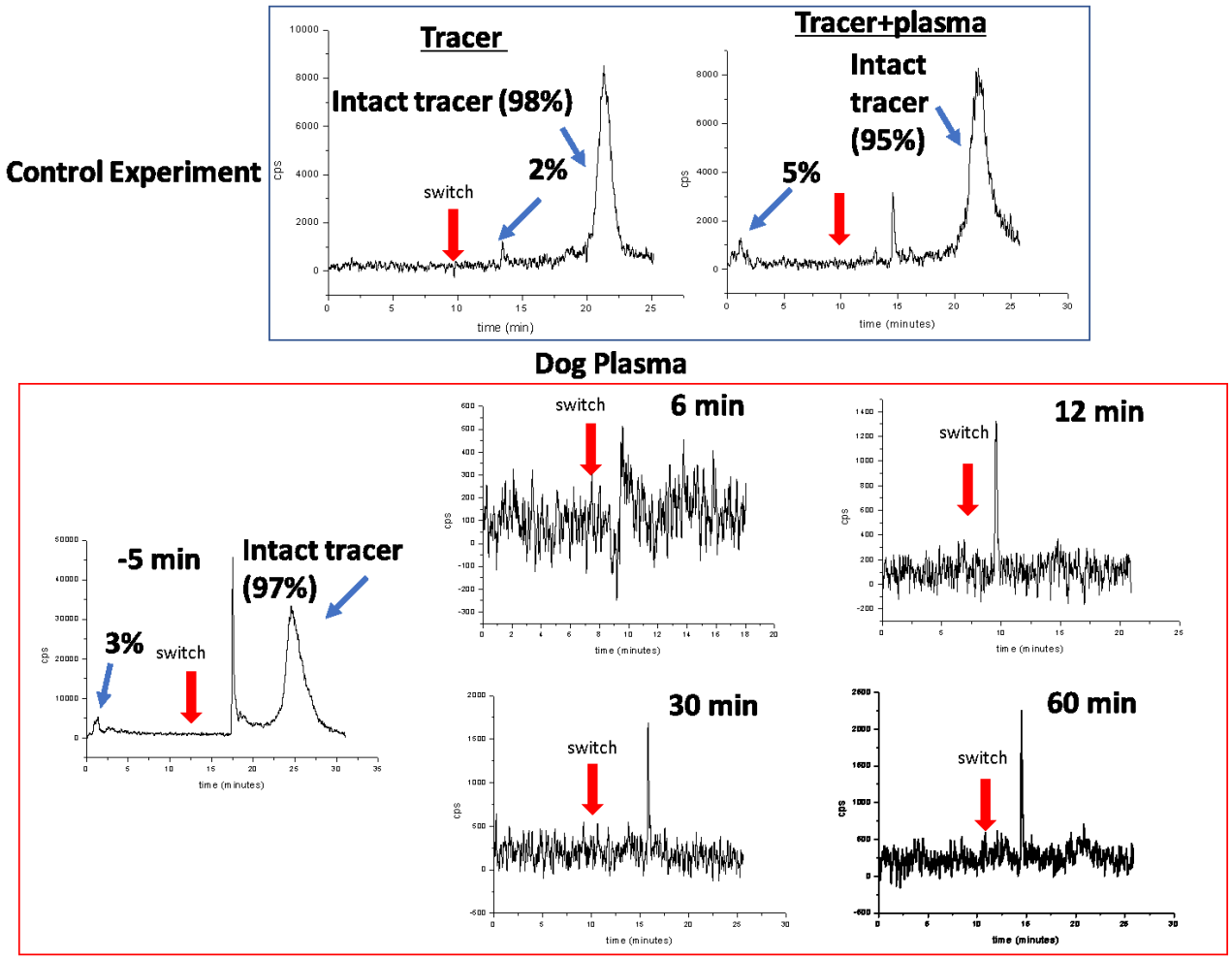

Figure S3. Representative analytical HPLC chromatograms displaying radiometabolites in dog plasma at 6, 12, 30, and 60 min post-injection. No [^{18}F]AlF-DFH17 metabolites or parent compound were detected in dog plasma at all time points.

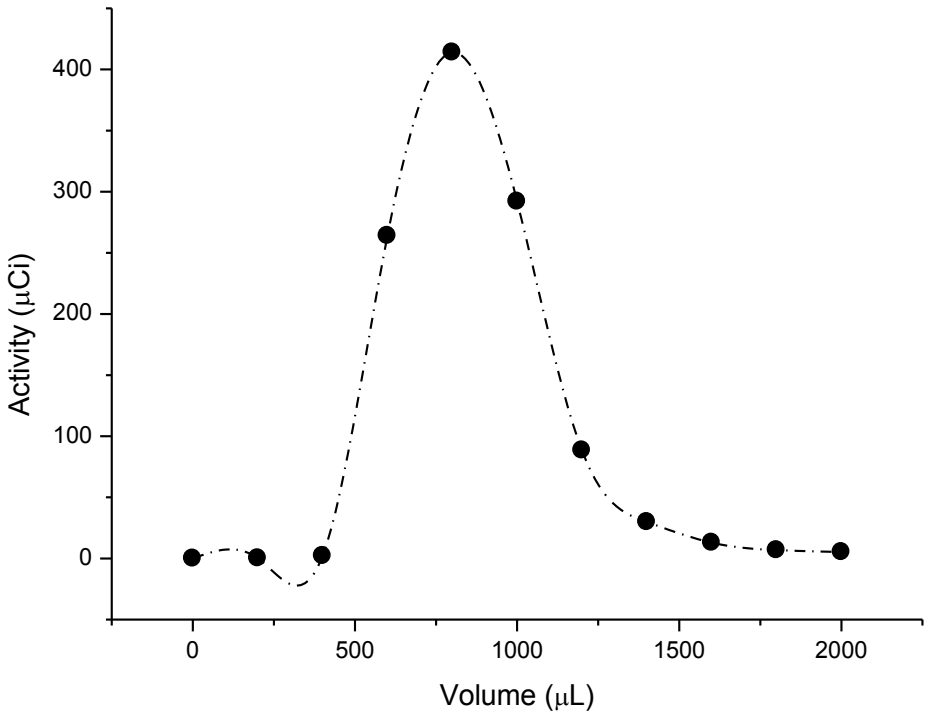

Figure S4. Elution profile of [^{18}F]FB-Candesartan in a C18 Sep-Pak Plus (360 mg) with ethanol as mobile phase. Two mL ethanol was used to eluted of [^{18}F]FB-Candesartan with a subsequent solvent evaporation step at 45 ^{o}C under nitrogen in order to obtain a concentrated formulation of the tracer.

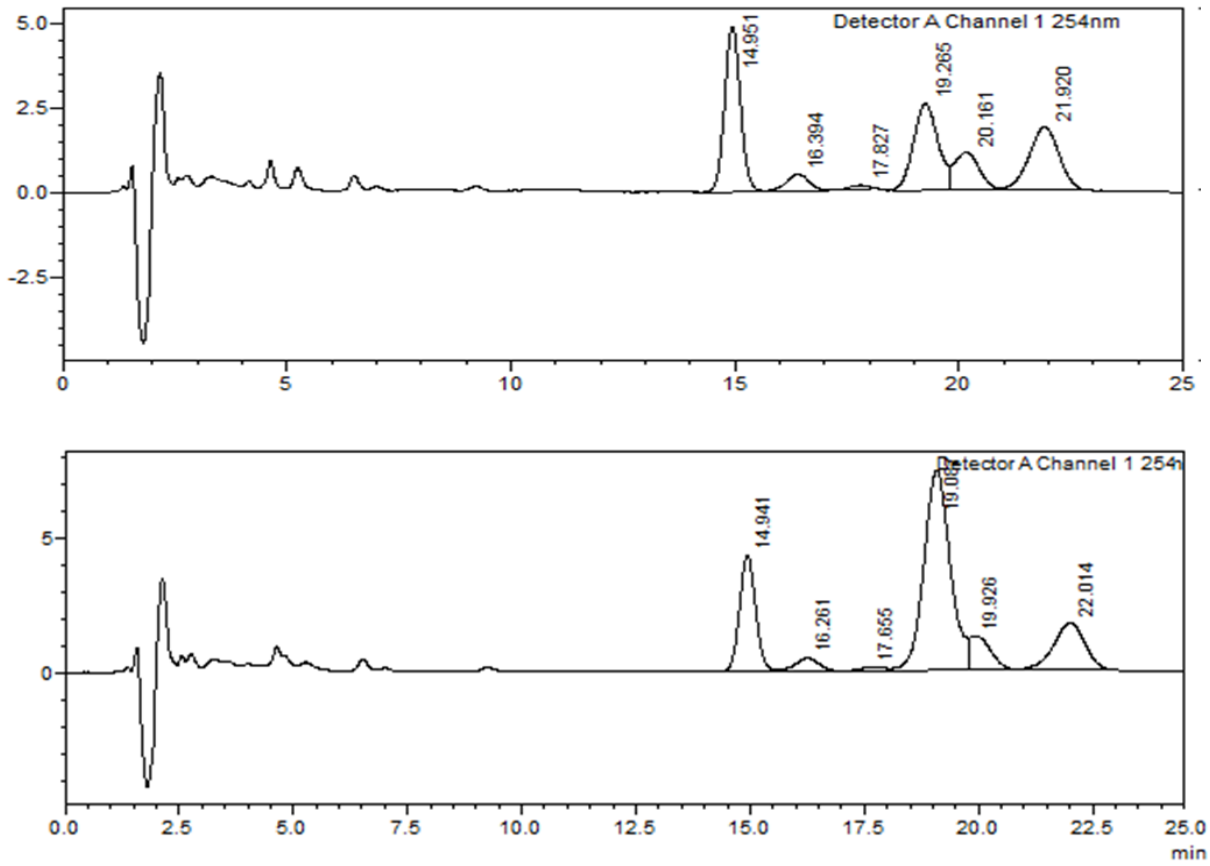

Figure S5. Analytical HPLC chromatograms of chemical impurities of [^{18}F]FB-Candesartan (Top) and best HPLC separation condition (Bottom) with co-injected authentic compound FB-Candesartan (t_R=19.09 min). Phenomenex Luna C18 (2) column (250×4.6 mm, 10µm) (2 mL/min, Water 0.1% TFA/CH_3CN 0.1% TFA 55:45). Impurity at t_R=14.9 min was successfully separated from FB-Candesartan (t_R=19.09 min). However other structurally-close by-product impurities (t_R=17.5 min and t_R=20 min) were eluted along with FB-Candesartan (t_R=19.09 min) which is still detrimental for its final MA.